

Copyright

by

Nathan Taylor Hahn

2012

The Dissertation Committee for Nathan Taylor Hahn Certifies that this is the approved version of the following dissertation:

Synthesis and Characterization of Semiconductor Thin Films for Photoelectrochemical Energy Conversion

Committee:

C. Buddie Mullins, Supervisor

Allen J. Bard

Gyeong S. Hwang

Keith J. Stevenson

Keith P. Johnston

**Synthesis and Characterization of Semiconductor Thin Films for
Photoelectrochemical Energy Conversion**

by

Nathan Taylor Hahn, B.S. Chem. E.

Dissertation

Presented to the Faculty of the Graduate School of

The University of Texas at Austin

in Partial Fulfillment

of the Requirements

for the Degree of

Doctor of Philosophy

The University of Texas at Austin

August 2012

Dedication

To my family and friends

Acknowledgements

I thank my advisor, Buddie, and the rest of the Mullins research group for all their advice and practical help over the years. I also express my gratitude to Dr. Bard and Dr. Korgel and members of their research groups (especially Dr. Heechang Ye and Dr. Vince Holmberg) for the generous lending of their equipment and expertise to our research efforts. I also thank several UT facility scientists and technical specialists, especially Dr. Hugo Celio, Butch Cunningham, Jim Smitherman, and Michael Ronalter, whose valuable help with experimentation and equipment fabrication over the years made this work possible.

Synthesis and Characterization of Semiconductor Thin Films for Photoelectrochemical Energy Conversion

Nathan Taylor Hahn, Ph.D.

The University of Texas at Austin, 2012

Supervisor: Charles Buddie Mullins

The field of solar energy conversion has experienced resurgence in recent years due to mounting concerns related to fossil fuel consumption. The sheer quantity of available solar energy and corresponding opportunity for technological improvement has motivated extensive study of novel light-absorbing semiconductors for solar energy conversion. Often, these studies have focused on new ways of synthesizing and altering thin film semiconductor materials with unique compositions and morphologies in order to optimize them for higher conversion efficiencies. In this dissertation, we discuss the synthesis and electrochemical characterization of a variety of candidate semiconductor materials exhibiting promising characteristics for photoelectrochemical solar energy conversion.

Three specific methods of thin film deposition are detailed. The first is a physical vapor deposition technique used to independently tune the morphology and composition of hematite ($\alpha\text{-Fe}_2\text{O}_3$) based materials. Because of hematite's poor electronic properties, these modifications were able to significantly improve its performance as a photoanode for water oxidation. The second technique is electrodeposition, which was employed to deposit the novel ternary metal oxide, CuBi_2O_4 . The study of these films, along with those prepared by physical vapor deposition, provided insight into the factors limiting the

ability of this photo-active material to function as a photocathode for hydrogen evolution from water. The third technique is chemical spray pyrolysis, which was employed to deposit and optimize films of the bismuth chalcogenides BiOI and BiSI. These studies were used to obtain previously unknown properties of these materials relevant to their utilization in photoelectrochemical cells. The manipulation of deposition temperature had significant effects on these properties and dictated the films' overall photoconversion performance.

Table of Contents

List of Figures	x
Chapter 1: Introduction.....	1
References	17
Chapter 2: Reactive Ballistic Deposition of α -Fe ₂ O ₃ Thin Films for Photoelectrochemical Water Oxidation	19
Introduction	19
Experimental Methods	22
Results and Discussion	25
Conclusions	42
References	43
Chapter 3: Photoelectrochemical Performance of Nanostructured Ti- and Sn-doped α -Fe ₂ O ₃ Photoanodes	46
Introduction	46
Experimental Section	48
Results and Discussion	52
Conclusions	66
References	68
Chapter 4: Electrochemical Synthesis and Characterization of p-CuBi ₂ O ₄ Thin Film Photocathodes.....	71
Introduction	71
Experimental Methods	72
Results and Discussion	75
Conclusions	95
References	96
Chapter 5: Spray Pyrolysis Deposition and Photoelectrochemical Properties of n-type BiOI Nano-Platelet Thin Films	98
Introduction	98
Experimental Section.....	100

Results and Discussion	102
Conclusions	120
References	121
Chapter 6: BiSI Micro-Rod Thin Films: Efficient Solar Absorber Electrodes?	123
Introduction	123
Experimental Section	124
Results and Discussion	126
Conclusions	137
References	138
Chapter 7: Concluding Remarks and Future Research	140
Overview of Completed Work	140
Ongoing and Future Work	143
References	148
Appendix A: Supplemental Information for Reactive Ballistic Deposition of α -Fe ₂ O ₃ Thin Films for Photoelectrochemical Water Oxidation.....	150
Appendix B: Supplemental Information for Photoelectrochemical Performance of Nanostructured Ti- and Sn-doped α -Fe ₂ O ₃ Photoanodes	152
Appendix C: Supplemental Information for Electrochemical Synthesis and Characterization of p-CuBi ₂ O ₄ Thin Film Photocathodes	157
Appendix D: Supplemental Information for Spray Pyrolysis Deposition and Photoelectrochemical Properties of n-type BiOI Nano-platelet Thin Films	163
Appendix E: Supplemental Information for BiSI Micro-Rod Thin Films: Efficient Solar Absorber Electrodes?.....	168
Bibliography	173

Vita 183

List of Figures

- Figure 1.1. Right: Historical and predicted trends in annual world energy consumption. Left: Annual world energy consumption by source. ... 1
- Figure 1.2. Worldwide solar insolation map. 3
- Figure 1.3. US levelized electricity cost by source (2016 predicted national average). 5
- Figure 1.4. Simplified schematic of natural photosynthesis indicating the electron transfer pathways and photosystems (PS's) I and II. 8
- Figure 1.5. Left: Spectral distribution of solar energy. Right: Band gaps and band edge positions of some common semiconductors plotted along with the electrochemical potentials of proton reduction and water oxidation. 10
- Figure 1.6. Left: PEC tandem water splitting cell with two photoelectrodes. Right: Photocatalyst particle scheme using individually tailored particles for oxygen and hydrogen evolution, respectively. 11
- Figure 2.1. Left: X-ray diffraction of an α -Fe₂O₃ film annealed in air for 2 hr at 450°C. Lines belonging to the hematite powder diffraction pattern are included. Other visible peaks are from the FTO substrate. Right: UV-Vis absorbance of an α -Fe₂O₃ film approximately 200 nm thick annealed in air for 2 hr at 450°C. 26
- Figure 2.2. Mott-Schottky plot derived from electrochemical impedance spectroscopy performed at 1000 Hz taken at pH 7 for a film deposited at 0° and annealed to 425°C. 27

Figure 2.3. Left: SEM images of α -Fe₂O₃ films deposited at various angles and annealed to 450°C. Right: High resolution SEM of a cluster of nanocolumns (a), and bright field TEM of the top of a single nanocolumn (b). The samples were scraped off of a film deposited at 82° on FTO and were not annealed. 28

Figure 2.4. Left: Maximum steady-state j_{ph} values at 0.4 V vs Ag/AgCl for films deposited at various angles and annealed for 2 hr at 450°C plotted with the normalized voltametric charge (q^*) transferred during CV sweeps between -0.1 and 0.1 V vs Ag/AgCl in 1M KOH for films of approximately equal thickness and annealed for 2 hr at 450°C. Right: Schematic representation of processes occurring during irradiation of film. (1) light absorption and formation of electron-hole (e^-h^+) pairs; (2) bulk recombination; (3) recombination at electrolyte interface; (4) hole transport; (5) electron transport; (6) recombination at the FTO interface. 29

Figure 2.5. Left: Photocurrent trend at 0.4 V vs. Ag/AgCl as annealing temperature is increased for films deposited at 55° and having thicknesses of ~ 240 nm. Right: Mean crystallite size of the (104) grain size plotted along with the ratio of the (110):(104) peak areas for various annealing temperatures..... 32

Figure 2.6. Left: Photoelectrochemical behavior under white-light illumination in 1M KOH for films annealed to various temperatures. The photocurrent onset potentials (vertical lines) tended to shift negatively as temperature increased. Right: Steady state photocurrent at 0.4 V vs. Ag/AgCl in 1M KOH for a variety of film thicknesses. Films were deposited at 55° and annealed to 450°C for 2 hr..... 34

Figure 2.7. Left: Comparison of photocurrent at 0.4 V vs. Ag/AgCl and photon absorption at 420 nm trends for very thin films annealed to 550°C. Right: IPCE spectra taken at 0.5 V vs. Ag/AgCl in 1M KOH employing front and backside illumination for films deposited at 55° incidence and annealed at the indicated temperatures..... 37

Figure 2.8. Left: IPCE spectrum of an optimized film recorded in 1M KOH at +0.5 V vs. Ag/AgCl. Right: Spectral photocurrent data under AM1.5 illumination calculated from IPCE data at +0.5 V vs. Ag/AgCl. 39

Figure 2.9. Left: IPCE spectrum of an optimized film recorded in 1M KOH at 0.5 V vs. Ag/AgCl. Right: Spectral photocurrent data under AM1.5 illumination calculated from IPCE data at 0.5 V vs. Ag/AgCl..... 40

Figure 3.1. Diagram of the inside of the deposition chamber indicating the orientation of the evaporators and substrate holder. 50

Figure 3.2. Left: XRD profiles for films deposited at 75° incidence having thicknesses of approximately 360 nm and annealed to 550°C for two hr both with and without 4% Ti incorporation. Expected peak locations for hematite (PDF #97-002-4004) are indicated by stars. Right: UV-vis absorbance spectra for films deposited at 75° incidence, also with and without 4% Ti incorporation..... 53

Figure 3.3. Left: SEM images of 4% Ti-doped films approximately 180 nm thick and deposited at various angles. Right: HRSEM images of sections of 4% Ti-doped films deposited at 75° incidence.	54
Figure 3.4. Left: Photocurrent at 1.4 V vs. RHE for 4% Ti-doped films deposited at various angles. Right: Photocurrent at 1.4 V vs. RHE for different doping levels of Ti or Sn.	55
Figure 3.5. Vertical EDS line scan of a section of 4% Ti-doped film deposited at 75° incidence.	59
Figure 3.6. XPS spectra of a 4% Ti-doped film deposited at 75° incidence. Left: Fe 2p region. Right: Ti 2p region.	60
Figure 3.7. Mott-Schottky plots in 1M KOH for films deposited at 75° incidence on top of a dense blocking layer deposited at 0° incidence.	62
Figure 3.8. Left: Chopped light experiments using full spectrum illumination for 4% Ti-doped films deposited at 0° and 80° incidence. Right: Ratio of visible-light to UV-light contributions to the photocurrent at 1.4 V vs. RHE as a function of the calculated porosity of 4% Ti-doped films deposited at angles ranging from 0° to 80°.	63
Figure 3.9. IPCE performance at 1.4 V vs. RHE for films deposited at 75° incidence with either 4% Ti or 4% Sn. Right. Photoelectrochemical j-E curves comparing the performance of an optimized 4% Ti doped film (75° incidence, 550°C anneal) to an optimized undoped film (55° incidence, 450°C anneal) at lower applied potentials under full spectrum illumination.	65

Figure 4.1. Electrodeposited films of Cu-Bi deposited at a) -0.3 V, b) -0.5 V, or c) -0.7 V vs Ag/AgCl from a nitric acid bath. The scale bar applies to all images..... 76

Figure 4.2. EDS analysis results for the ratio of Bi to Cu in the Cu-Bi films deposited at various potentials vs Ag/AgCl. The desired Bi:Cu ratio is indicated by the horizontal dashed line. The error bars represent the standard deviation of the five EDS spot analyses taken on each film. 77

Figure 4.3. Left: XRD patterns for films deposited at -0.5 V vs Ag/AgCl and annealed to various temperatures. A standard kusachiite line pattern (PDF # 00-042-0334) is also displayed. Observable SnO₂ peak positions are indicated by Δ. Right: SEM images of CuBi₂O₄ particulate films deposited at -0.5 V for 2 min with overall cation concentration of 12 mM. These samples were then annealed to a) 350°C, b) 450°C, c) 550°C or d) 600°C for 2 h in air. The scale bar applies to all images.79

Figure 4.4. SEM images of CuBi₂O₄ particulate films deposited -0.5 V with varying overall cation concentrations: a) 24 mM, b) 6 mM, c) 3 mM or d) 1.2 mM. Approximately the same amount of CuBi₂O₄ was deposited in each case and all samples were annealed to 600°C for 2 h in air. The scale bar applies to all images. 80

Figure 4.5. SEM images of CuBi₂O₄ films deposited at -0.5 V from a bath cation concentration of 6 mM for a) 2 min, b) 4 min, and c) 8 min, and annealed at 600°C for 2 h. 82

Figure 4.6. UV-vis-NIR absorptance spectra calculated using a) total transmittance (direct + diffuse) of a film on FTO, b) transmittance + reflectance of a film on FTO, and c) transmittance + reflectance of an FTO substrate only. The films were deposited at -0.5 V for 5 min from a bath concentration of 6 mM. A photograph of the film is shown at top-right.

..... 83

Figure 4.7. Photoelectrochemical response under “chopped” Xe-lamp illumination of a typical film deposited at -0.5 V for 5 min. The inset indicates the switch from anodic to cathodic photocurrent between 1.05 and 1.1 V vs RHE. The electrolyte is N₂ degassed aqueous Na₂SO₄ (adjusted to pH 10.8), and the scan rate is 25 mV/s. 85

Figure 4.8. Left: One hour photocurrent vs. time plots for CuBi₂O₄ films held at constant potentials in pH 10.8 (a) or 3.5 (b) in 0.1M Na₂SO₄ solutions under full spectrum Xe-lamp illumination. Right: XPS Cu 2p spectra for CuBi₂O₄ films after more than one hour of constant photocurrent passage in either pH 10.8 (a) or pH 3.5 (b) aqueous Na₂SO₄ electrolyte. The Cu 2p_{3/2} peak positions for Cu⁺ and Cu²⁺ at 932.4 and 933.8 eV are indicated by the dashed lines. 86

Figure 4.9. Left: IPCE plots for front and backside illumination of a typical CuBi₂O₄ film held at -0.2 V vs Ag/AgCl in pH 10.8 Na₂SO₄ after 1 h steady photocurrent passage. Right: Comparison of IPCE and APCE for a typical film after 1 h steady photocurrent passage at -0.2 V vs Ag/AgCl in pH 10.8 Na₂SO₄. 88

Figure 4.10. Left: Measured photocurrents during LSV scans (25 mV/s) at -0.2 V vs. Ag/AgCl in N₂ bubbled 0.1M Na₂SO₄ (pH 10.8) for various deposition bath temperatures. Right: SEM images of CuBi₂O₄ films deposited from baths at different temperatures at -0.5 V vs. Ag/AgCl for 5 min. with a cation concentration of 6 mM. The scale bar is 2 μm and applies to all images..... 92

Figure 4.11. SEM images of a film synthesized using ballistic deposition. Left: before annealing. Right: after annealing at 600°C. The scale bar applies to both images..... 93

Figure 4.12. Comparison of the PEC performance CuBi₂O₄ films in N₂ bubbled aqueous Na₂SO₄ (pH 10.8). Left: LSV behavior under chopped illumination. Right: IPCE spectra taken at 0.64 V vs. RHE..... 94

Figure 5.1. Left: SEM images of BiOI films deposited at the indicated temperatures on FTO-coated glass substrates. Right: (a) HRTEM image and discrete-fourier-transform (DFT) of a BiOI platelet deposited at 260°C, and (b) HRTEM image and DFT of a platelet deposited at 275°C along with the measured d-spacing.....103

Figure 5.2. Left: Trend in mean platelet thicknesses measured from SEM images for various deposition temperatures. Right: XRD patterns for films deposited at the indicated temperatures. The indices of the peaks corresponding to BiOI are labeled, and the peaks from the FTO substrate are indicated by *.105

Figure 5.3. Left: EDX composition of films deposited at various temperatures. The dashed line is added to guide the eye. Right: Deconvoluted O 1s core-level spectrum obtained for a BiOI film deposited at 260°C. The position of each fitted peak is indicated in the legend.108

Figure 5.4. Left: Absorbance spectra of films deposited at various temperatures calculated from UV-vis transmittance measurements in an integrating sphere. Right: Tauc plots created for the absorbance values above, with linear extrapolations to $(\alpha h\nu)^{1/2} = 0$109

Figure 5.5. Left: LSV behavior in NaI/Acetonitrile for BiOI films deposited at the indicated temperatures. The anodic scan rate employed was 25 mV/s. Right: Photocurrent values measured at 0.4 V vs. Ag/AgCl for these films as well as a film deposited at 260°C.....111

Figure 5.6. Left: LSV plot using a 3-electrode configuration in I⁻/acetonitrile both with and without a 420 nm cut-on filter for an optimized film deposited at 260°C. The anodic scan rate was 25 mV/s. Right: IPCE spectrum recorded at 0.4 V vs Ag/AgCl for a typical film deposited at 260°C with a peak light intensity of 476 $\mu\text{W}/\text{cm}^2$112

Figure 5.7. Log-log plots of photocurrent vs. light intensity at 0.4 V vs. Ag/AgCl for a film deposited at 260°C in the low (a) and high (b) light intensity regimes. The slopes of the resulting plots are indicated.114

Figure 5.8. Left: Mott-Schottky plots measured in 0.5M NaI/0.05M I₂ in acetonitrile for a film deposited at 260°C. Right: Derived Mott-Schottky plot parameters at a frequency of 1 kHz displayed as a function of deposition temperature.115

Figure 5.9. Open circuit potential measurements performed in 0.5M NaI in acetonitrile under 400 mW/cm ² illumination for films deposited at various temperatures.	116
Figure 5.10. Left: LSV's recorded under intermittent illumination both with and without hole scavenger species at pH 7. Right: Photocurrent vs. time plots at a constant potential of 0.5 V vs. Ag/AgCl in the same solutions.	117
Figure 5.11. Left: Photocurrent performance at 0.4 V vs. Ag/AgCl in 1M Na ₂ SO ₃ of a film deposited at 260°C measured (a) before and (b) after 20 min. soaking in the dark at pH 7. Right: XPS O 1s spectrum recorded after soaking a film (deposited at 260°C) in water for several hours.....	118
Figure 6.1. Bulk analyses of BiSI films sprayed at various temperatures. Left: XRD diffraction patterns with the non-BiSI peaks indicated. Right: EDX atomic % ratios of sulfur and iodine to bismuth.	127
Figure 6.2. Electron microscopy images of the micro-rod morphology of the BiSI films. Left: SEM images of films deposited at a) 225, b) 250, c) 275, and d) 300°C. Right: STEM image of a broken micro-rod from a film deposited at 275°C, exposing the internal structure.....	130
Figure 6.3. XPS analyses of BiSI films deposited at various temperatures. Left: Surface atomic % ratios of iodine, sulfur, and oxygen to bismuth. Middle: Core level Bi 4f spectra indicating the designations of the observed peaks. Right: Core level Bi 4f spectra comparing a BiSI and BiOI film deposited at 250°C, with the indicated binding energies of the observed peaks.	131

Figure 6.4. Core level O 1s spectra including the fitted component peak positions for BiSI films deposited at various temperatures.	132
Figure 6.5. Left: Photocurrents recorded at 0.4 V vs. Ag/AgCl for films deposited at various temperatures. Right: LSV behavior (with and without a UV cut-off filter) of a film deposited at 275°C.	134
Figure 6.6. Left: IPCE spectra of a film deposited at 275°C. Right: Optical absorption coefficients calculated for a film deposited at 275°C from transmittance measurements along with a photograph of the film.	135
Figure 6.7. Left: Photocurrent vs. time behavior at 0.4 V vs. Ag/AgCl in 0.25M NaI in acetonitrile for a film deposited at 275°C. Right: SEM images of films tested under the same conditions for the indicated times: a) 1m, b) 2m, c) 5m, d) 10m.	136
Figure 7.1. Band edge energetics of promising semiconductors for PEC water splitting compared to those of hematite and BiVO ₄ . The band edge positions relative to the water splitting redox potentials are estimated from data in the literature. The line color corresponds to the material band gap.	144
Figure 7.2. Left: Photoconversion spectra for pristine and Se-doped BiSI films under the short circuit condition (2-electrode configuration, 0 V vs. Pt) employing I ⁻ /I ₃ ⁻ in acetonitrile as the electrolyte. Illumination was accomplished through the backside of the photoanodes. Right: Proposed layered heterojunction scheme for a PEC cell employing a n-BiSI film and an optimized overlayer material.	147

Figure A.1. XPS Fe 2p spectrum of a film deposited at 80° incidence and annealed at 450°C for 2 h. The core level designations of the primary peaks and the position of the visible satellite peak are indicated.	150
Figure A.2. SEM image of a 1 μm thick α-Fe ₂ O ₃ film deposited at 80°C. The film was scratched to provide a clearer view of the nanocolumnar structure.	151
Figure B.1. Grazing incidence X-ray diffraction patterns for Ti-doped films deposited at 75° incidence with various flux ratios of O ₂ :Fe. The un-indexed peak at 37.5° belongs to cassiterite (SnO ₂).	152
Figure B.2. SEM images of 5% Ti-doped samples deposited at 75° incidence and annealed to either 400°C (bottom) or 550°C (top) for 2 h.	153
Figure B.3. XPS Sn 2p spectrum for a 4% Sn-doped α-Fe ₂ O ₃ film, with the indicated core level peak designations.	154
Figure B.4. XRD profiles of 12% Ti or Sn-doped α-Fe ₂ O ₃ films deposited at 75°C incidence and annealed to 550°C for 2 h. Two-theta peak positions for hematite (PDF #97-002-4004) (o) and cassiterite (PDF #97-000-9163) (Δ) are indicated.	155
Figure B.5. XPS depth profile of a 4% Ti-doped α-Fe ₂ O ₃ film deposited at 0° incidence and annealed to 450°C for 2 h. Ar ⁺ sputter depth was determined using profilometry.	156
Figure C.1. Steady-state photocurrent density at -0.2 V vs. Ag/AgCl (in N ₂ bubbled aqueous Na ₂ SO ₄ , pH ~6) for CuBi ₂ O ₄ films deposited from a bath concentration of 12 mM and annealed to various temperatures.	157

Figure C.2. UV-vis-NIR direct transmittance spectrum of a typical CuBi_2O_4 film deposited from a bath concentration of 6 mM. The inset shows the corresponding Tauc plot indicating an apparent 1.4 eV direct band gap.	158
Figure C.3. XPS (a) Bi 4f and (b) Cu 2p spectra for a film prior to PEC testing. Core-level designations for the observed Bi^{3+} and Cu^{2+} peaks are indicated.	159
Figure C.4. IPCE values for a typical film before and after 1 h steady photocurrent passage at -0.2 V vs. Ag/AgCl in pH 10.8 aqueous Na_2SO_4	160
Figure C.5. SEM images of films deposited at -0.7 V for 3.5 min (a) and 7 min (b) as as -0.9 V for 2.5 min (c) and 5 min (d) from a bath containing a 3:1 ratio of Bi:Cu. The scale bar is 2 μm and applies to all images.	161
Figure C.6. SEM images of CuBi_2O_4 films deposited from baths at different temperatures at -0.5 V vs. Ag/AgCl for 5 min. with a cation concentration of 6 mM. The scale bar is 2 μm and applies to all images.	162
Figure D.1. Monochromatic light intensity at the surface of the film employed for IPCE testing.	163
Figure D.2. XRD patterns of films created by spraying the BiOI precursor solution at low temperatures. The arrows indicate the peak positions of BiI_3 , diamonds indicate unidentified peaks, and all other peaks originate from SnO_2 in the substrate.	164
Figure D.3. XPS core-level spectra (Bi 4f and I 3d) for a BiOI film deposited at 260°C, indicating the positions of the Bi^{3+} and I^- peaks and their orbital designations.	165

Figure D.4. I-V curves in the dark and under illumination for a BiOI film deposited at 260°C tested using a 2-electrode configuration in 0.5M NaI / 0.05M I ₂ in acetonitrile. The working electrode was illuminated from the backside.	166
Figure D.5. Steady-state photocurrent test at 0.4 V vs. Ag/AgCl in 0.25M NaI in acetonitrile. The film was deposited at 260°C and illuminated from the backside.	167
Figure E.1. Mean (210) crystallite sizes calculated from the XRD patterns of films deposited at various temperatures.	168
Figure E.2. Linear sweep voltammogram under chopped illumination at cathodic potentials with and without a 420 nm cut-on filter for a film deposited at 275°C. Anodic photocurrents are displayed in the negative direction. The solution was 0.25M NaI in acetonitrile, and the scan rate was 25 mV/s.	169
Figure E.3. Plots of $\ln(1-\phi)$ vs. $(E-E_{fb})^{1/2}$ under monochromatic illumination for two different BiSI films deposited at 275C. The average calculated hole diffusion length (L_p) for each set of three measurements is displayed.	170
Figure E.4. Linear sweep voltammogram under chopped illumination for films deposited at 275°C on metal foil substrates. The solution was 0.25M NaI in acetonitrile, and the scan rate was 25 mV/s.	171
Figure E.5. Tauc plots constructed using total transfectance measurements for a film deposited at 275°C to determine the indirect (black) and direct (blue) bandgaps of BiSI (1.57 and 1.63 eV) from linear fits indicated by the dashed lines.	172

Chapter 1: Introduction

Throughout the centuries humanity has developed increasingly advanced systems of energy conversion in order to enable the growth of population and technology. In modern times the convenient extraction and implementation of energy-dense carbonaceous resources known as fossil fuels have improved the quality and quantity of global technology by leaps and bounds. As global population and industrialization continue to grow the demand for energy will certainly increase for the foreseeable future, rising to over 25 TW average consumption (750 quadrillion btu per year) by 2035 according to reasonable estimates (Figure 1.1).¹ This rise in energy demand will be accompanied by a number of technological challenges that must be met if reasonable economic growth is to be maintained.

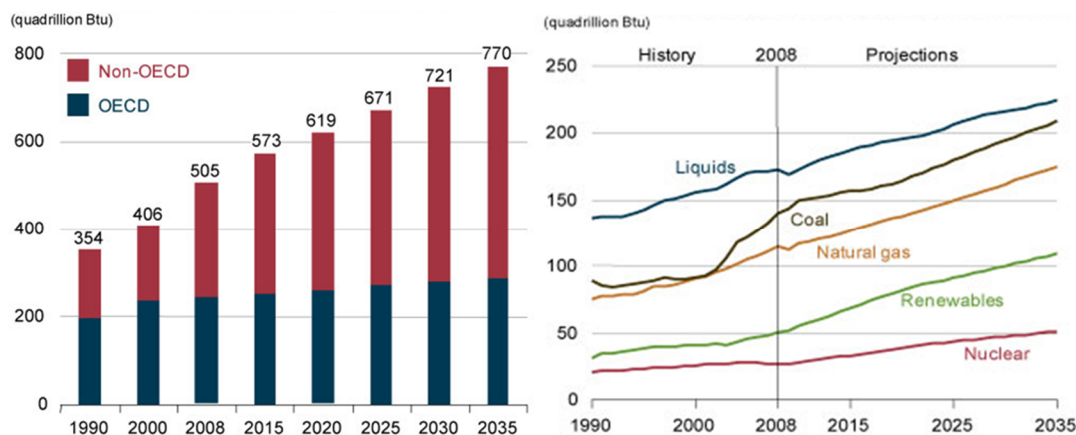


Figure 1.1. Right: Historical and predicted trends in annual world energy consumption. Left: Annual world energy consumption by source.

The dominance of fossil fuels on the global energy landscape is clearly demonstrated in figure 1.1, which shows that 85% of the world's energy supply comes from three primary fossil fuel sources oil, coal, and natural gas.¹ When one considers the

total proven reserves of these three fossil fuels in terms of their global production rates, reserve lifetimes of 46, 118, and 58 years can be estimated for oil, coal and natural gas, respectively.² These lifetimes are typically underestimated since new reserves are found continually, but the bottom line is that these energy sources have finite life spans on the order of tens to hundreds of years. Particularly worrisome is the depletion of oil as it is also a feedstock for the production of many vitally important chemicals and materials. For this reason there is a great deal of motivation to develop alternative energy sources and conversion technologies in order to stave off the depletion of this extremely useful commodity. Additionally, as the scarcity of fossil fuels increases, the effects of their geographically defined availability become more and more apparent in global politics. The largest oil reserves are located in the relatively politically unstable regions of Venezuela and the Middle East, which raises concerns domestically regarding whether the U.S. will have continued access to these at reasonable prices. The unabated depletion of easily obtainable oil and mounting environmental regulations are likely to increase the price of oil for the foreseeable future.

In addition to quickly depleting a finite resource, the over-consumption of fossil fuels also results in the emission of a number of harmful pollutants. Despite extensive advances in combustion operation methods and product treatment technologies, fossil fuel energy sources still account for almost all CO₂ produced by energy-related technologies.³ For several decades climatologists have become increasingly concerned over the phenomenon of anthropogenic climate change. Essentially, the widespread consumption of fossil fuels has changed the composition of the atmosphere such that it has begun to affect a statistically significant increase in mean global temperature.⁴ Although accurate climate prediction is, of course, difficult, the reasonable possibility of disastrous consequences due to unmitigated greenhouse gas emissions is significant

enough motivation for the development of cleaner alternatives to fossil fuel sources. The following section will address a number of such alternative energy technologies.

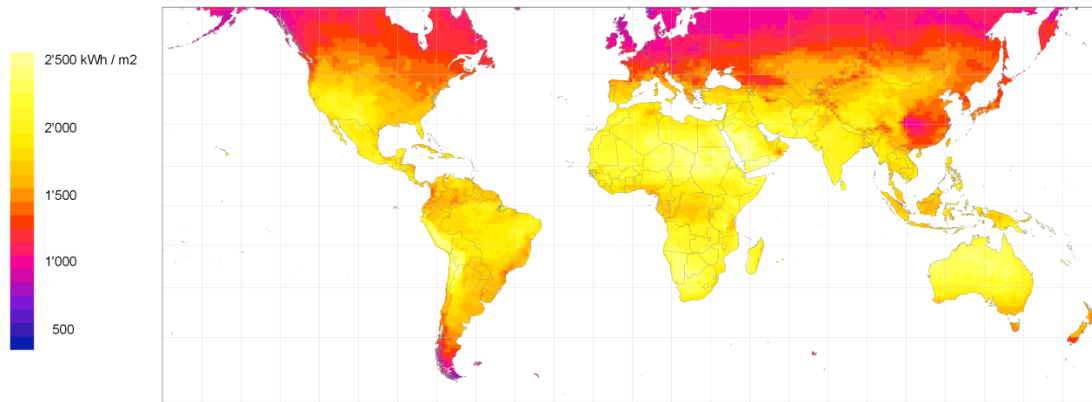


Figure 1.2. Worldwide solar insolation map.

Alternative Energy

A number of alternative energy sources to fossil fuels exist such as nuclear, geothermal, hydropower, wind, and solar. Each comes with its own list of concerns related to safety, capacity, and/or cost, however. Of the renewable strategies the most interesting option from a long-term standpoint is solar. Solar energy, although the least mature of the aforementioned alternative energy sources, possesses the largest potential capacity by far. The sun irradiates the earth with an average of 120,000 TW of power, meaning that only a miniscule fraction of the available solar energy must be harvested in order to supply power on the order of 25 TW or more. For instance, using a modest conversion efficiency of 10%, only 0.25% of the incident energy at the earth's surface is required to generate an average power of 25 TW. Additionally, solar energy is not localized to the degree that some of the other renewable options such as hydropower and geothermal are. Although certain regions enjoy greater average intensities than others,

the majority of the world population lives in regions enjoying an average of 1.5 MWh/m²/yr or more (Figure 1.2).⁵

The most common direct solar energy conversion technology of today is the photovoltaic (PV) or solar cell, which converts the energy of solar photons into electrical power. Unfortunately, due to the diffuse nature of sunlight large panels of these cells are required to convert a reasonable amount of power at a given location, and the materials and manufacturing methods for these cells often incur large production costs. As a result, solar-generated electricity is currently much more expensive than that from any other source (Figure 1.3).⁶ In addition to prohibitive costs, solar energy is plagued by variability. Although some of this variability is predictable (seasonal, diurnal), local weather patterns add an element of unpredictability, and the problem of matching the energy supply to the demand is significant. So, despite an enormous capacity for growth, there are obvious technological hurdles to overcome in order to achieve large scale solar energy implementation. Although it is the fastest growing energy technology on a relative basis, the current global installed capacity is only 33 GW,⁶ and significant research is needed to develop more cost-effective strategies of converting solar energy into usable forms. As a result, extensive research into new solar cell absorber materials, i.e., those consisting of thin film materials such as CuInGaSe₂, CdTe, a-Si, and Cu₂ZnSnS₄. Thin film solar energy conversion devices are attractive compared to the more widespread crystalline silicon cells due to their smaller raw material requirements. Of particular interest are compounds consisting of earth-abundant elements, which are a necessity if installation on the TW-scale is desired, and research into new absorber materials is quite active.

The time variant nature of solar and wind energy sources as well as the desire to achieve mobile alternatives to gasoline-fueled internal combustion engines necessitate the

development of efficient and transportable energy storage schemes. Some of the most interesting candidates include electromechanical (*e.g.* flywheels), electrochemical (*e.g.* batteries), and chemical (*e.g.* hydrogen) means. However, the energy and power densities of fuels such as hydrogen dwarf those of other transportable energy storage media. This, as well as the fact that hydrogen does not produce harmful emissions when combusted or reacted in a fuel cell, has caused many to christen it the fuel of the future, forming the backbone of the “Hydrogen Economy.”⁷ Although significant technical challenges still exist regarding the storage and conversion of hydrogen, much research is underway to develop new ways of producing hydrogen sustainably, particularly by utilizing solar energy.

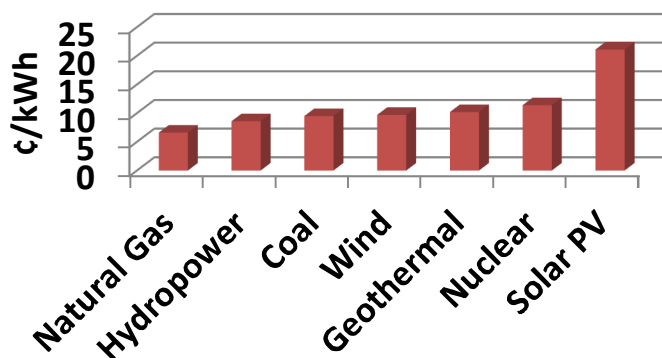


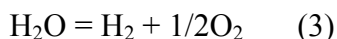
Figure 1.3. US levelized electricity cost by source (2016 predicted national average).

In addition to its promising energy storage ability, hydrogen is an extremely useful chemical feedstock, and in the US alone roughly 6 million tons per day are consumed in the refining of petrochemicals and the production of ammonia.⁸ These chemical processes account for nearly all hydrogen consumption worldwide as well. Unfortunately the bulk of this hydrogen is produced from fossil fuel sources so the same

issues plaguing fossil fuels apply to hydrogen as it is currently produced. The most common method involves the steam reforming of a hydrocarbon (such as methane), according to eq. 1. A second reaction step known as the water-gas shift reaction can be used to remove CO and produce more hydrogen (eq. 2).



It can be clearly observed that this method of producing hydrogen is associated with the production of CO₂ (5.5 tons of CO₂ are made for every ton of H₂) in addition to the consumption of a fossil fuel feedstock, meaning that this would not be a sustainable strategy for hydrogen production in the long-term. The primary alternative means of producing hydrogen in practice today is electrolysis. This involves the direct electrochemical liberation of hydrogen from water along with the production of either molecular oxygen (the water splitting reaction, eq. 3) or chlorine and sodium hydroxide (the brine splitting or chlor-alkali reaction, eq.4).



Electrolysis only accounts for roughly 4% of the hydrogen produced in the US due to the cost of electricity, which is consumed in large amounts as a result of the large thermodynamic requirements of 1.23 and 1.35 V for water splitting and brine splitting, respectively. Due to high kinetically induced overpotentials, especially at the anode, even larger voltages (more than 1.5 V) are required in practice. This electrical power requirement combined with the relatively large capital cost of an electrolyzer system hamper its cost-effective utilization in areas without a cheap nearby source of electricity.

Despite these drawbacks, the fact that such a system requires only electricity in addition to a cheap and abundant resource (water or brine) makes electrolysis schemes

very attractive in the long-term for sustainable hydrogen production when married to a renewable electrical power source. The main problem is that the renewable resource with the largest long-term capacity (solar) is also the most expensive. Hence, the combination of an expensive electrolyzer with an expensive source of electricity is quite unattractive at present, and a more ambitious option, the direct photoelectrochemical (PEC) conversion of solar energy to chemical energy through the fusion of these two systems into a single device, is of great interest.

Artificial Photosynthesis

Although water splitting is the most common reaction studied for this application, PEC energy conversion could theoretically be applied to a number of photosynthetic reactions, including the chlor-alkali reaction or even the synthesis of hydrocarbons such as methanol or methane *via* the reduction of CO₂ (combined with the oxidation of water to oxygen). In general, all of these solar-fuel producing schemes are referred to as artificial photosynthesis since they mimic the biological photosynthetic process used by plant-life throughout the world.⁹ Plants utilize two photon absorption steps, photosystems I and II, to increase the energy of electrons extracted from water such that they can drive the electrochemical conversion of CO₂ to carbohydrates. Ignoring the many intermediate charge transfer and reaction steps, one can consider photosynthesis as the combination of two redox half reactions: water oxidation and CO₂ reduction (Figure 1.4). Thus, photosystems I and II act as photocathodes and photoanodes, respectively, in an analogous photoelectrochemical cell. The most efficient plants are able to convert a maximum of about 1% of the incident solar energy incident upon them into energy stored in carbohydrates.¹⁰

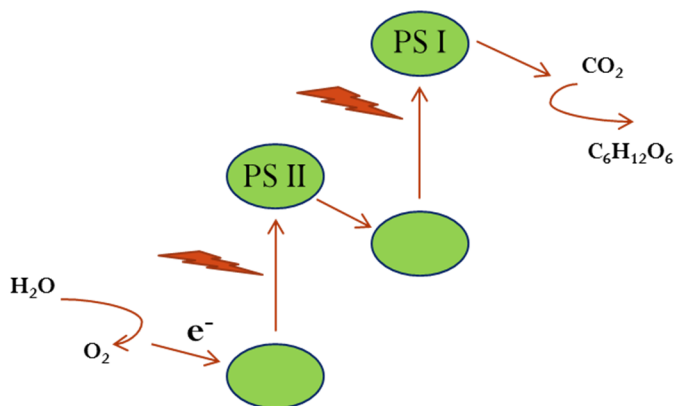


Figure 1.4. Simplified schematic of natural photosynthesis indicating the electron transfer pathways and photosystems (PS's) I and II.

The main obstacle to the practical implementation of artificial photosynthesis is high costs as a result of low solar energy conversion efficiencies. Solar-to-hydrogen (STH) efficiencies are defined as the chemical energy obtained in hydrogen divided by the solar energy input,¹¹ and a common target efficiency quoted to achieve reasonable cost parity with other hydrogen generation schemes (10%)⁹ could be achieved easily enough with a 70% efficient electrolyzer (producing hydrogen from water) and a 14% efficient solar cell. In fact, a state-of-the-art GaAs/GaInP₂ solar cell employed as a photocathode and wired to a platinum anode has demonstrated a STH efficiency of 12.4%, although the materials constituting the solar cell were extremely expensive and also unstable in aqueous environments under illumination.¹¹ The best *stable* PEC water splitting systems that have been demonstrated in the laboratory are only in the 1 to 5% efficiency range.^{13,14} Hence, the main thrust of research in this area is toward developing photo-active materials that are simultaneously stable, efficient, and cheap.

However, materials showing high activity tend to be unstable for aqueous photoelectrochemistry, and those exhibiting good stability are typically unattractive due to poor solar conversion properties. The problem of stability is related to the

phenomenon of photocorrosion, which occurs when energetic charge carriers created in a semiconductor by the absorption of photons drive a reaction that alters or dissolves the semiconductor itself. This is often exacerbated in the presence of water. For example, conduction band electrons generated in p-Cu₂O preferentially reduce Cu⁺ to Cu⁰ rather than reducing protons to H₂, and experimental results have indicated that the PEC activity decreases remarkably quickly.¹⁶ In other words, the electrochemical potential of Cu₂O reduction is more favorable (more positive) than that of the desired proton reduction reaction. This is the reason one cannot simply use a good PV material as a photoelectrode in a PEC cell without taking measures to prevent photocorrosion from occurring. In practice the stabilization of such materials has been very difficult to accomplish without simultaneously diminishing photoelectrode performance.

The problem of conversion efficiency is a combination of poor solar absorption and fast charge-carrier recombination. Since the energy of the solar spectrum lies primarily in the 400 to 1100 nm wavelength range (photon energies between roughly 1 and 3 eV), semiconductors of interest must possess appropriate band gaps and absorption coefficients to absorb as many of the photons in this region as possible (Figure 1.5). Another constraint, however, lies in the fact that the band edge energetics must also be optimized relative to the electrochemical potentials of the reactions of interest. If a certain amount of overpotential (extra electrochemical potential possessed by the electrons in the conduction band relative to the proton reduction potential, for instance) is unavailable, the charge transfer reaction will either not proceed at all, or only at low rates leading to the buildup and recombination of charge carriers at the surface. The required overpotential depends significantly on the kinetics of the particular reaction. Water oxidation, for example, even with a good catalyst requires 200 to 400 mV of overpotential to achieve current densities on the order of 10 mA/cm², whereas catalyzed

proton reduction requires approximately 50 mV.¹⁶ Therefore, the electrochemical potentials of these two reactions (1.23 V vs. RHE for water oxidation and 0 V vs. RHE for proton reduction) along with their associated overpotential requirements place minimum boundaries on the band edge positions of a potential photoelectrode/photocatalyst. A number of common examples are shown in Figure 1.5. As shown, materials with insufficiently negative conduction band edges cannot drive proton reduction, whereas those with insufficiently positive valence band edges cannot drive water oxidation. Hence, the combination of two photoelectrodes (each optimized for one half-reaction) is often a necessity.

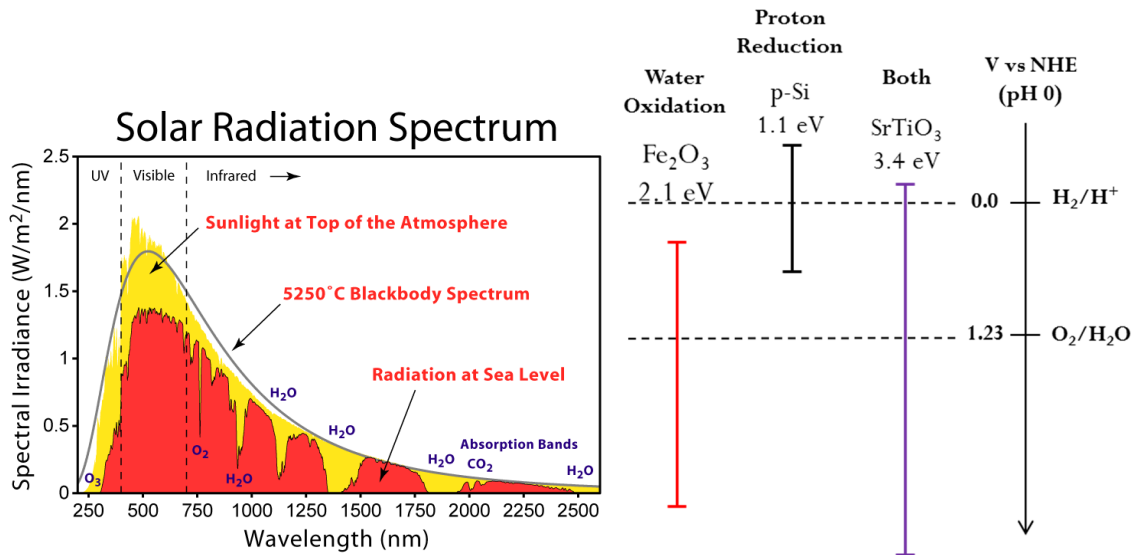


Figure 1.5. Left: Spectral distribution of solar energy.¹⁸ Right: Band gaps and band edge positions of some common semiconductors plotted along with the electrochemical potentials of proton reduction and water oxidation.

In addition to satisfying these thermodynamic and reaction kinetic demands, a PEC material must also possess sufficiently good electronic properties in order to maximize the rate of electron and hole transport to their respectively desired destinations before recombining. These properties can be quite sensitive to preparation method, and

material quality can thus be manipulated a great deal experimentally. Low carrier mobilities can also be compensated for by minimizing their required transport distances through the tuning of film morphology on the nanoscale. Because of this, a good approach to developing PEC materials is to select an initial material for study based on its optical properties and band edge energetics and then engineer its morphology and electronic properties to achieve higher photoconversion efficiencies.

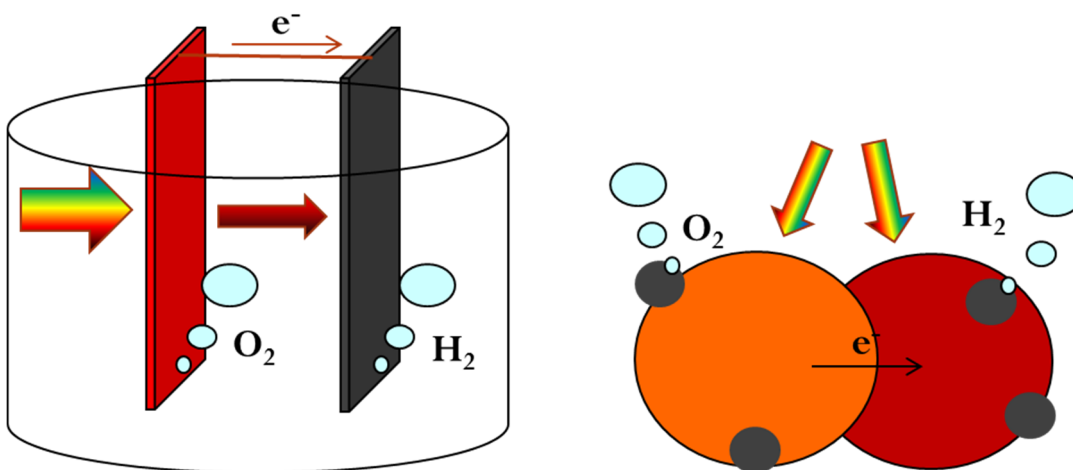


Figure 1.6. Left: PEC tandem water splitting cell with two photoelectrodes. Right: Photocatalyst particle scheme using individually tailored particles for oxygen and hydrogen evolution, respectively.

Generally, there are two primary PEC water splitting systems of interest (aside from the PV-electrolysis type mentioned earlier). The first type utilizes electrodes wired together to create a photoelectrochemical cell (Figure 1.6). In this case each half reaction occurs at one of the electrodes (at least one of which is a semiconductor photoelectrode), and the products are separated spatially. The second type utilizes semiconductor photocatalyst particles dispersed in a solution with no external electrical wiring (Figure 1.6). The water splitting half reactions may both occur on a single particle, or they may require two different particles either physically joined together (called a “photochemical

diode¹⁷⁾) or dispersed separately in a solution with a redox shuttle. Ideally, a single photoelectrode or photocatalyst particle would be employed for simplicity of implementation, but finding a single material with the proper band-energetics to drive both redox reactions and good photocatalytic properties under solar light has proven impossible in practice so far. The goal of our research is to identify, characterize, and optimize promising photoelectrode materials for either the water oxidation or proton reduction half reaction. Materials were selected for study based on the identification of desirable properties as found in the literature. Once a candidate material was identified, a deposition technique was selected based on novelty and potential ease of synthesizing photoelectrodes of the material. This technique was then used to manipulate film characteristics with the goal of a) obtaining a better understanding of material properties relevant to photoelectrochemistry and b) optimizing the material's performance for one of the water splitting half-reactions.

This thesis is divided into seven chapters. Chapter 1 provides general background information related to the motivation for and development of novel solar energy conversion and storage strategies and also introduces some of the technical challenges facing the development of solar absorber materials for artificial photosynthesis schemes. The following five chapters detail scientific studies in the area of PEC energy conversion materials that have been submitted to and/or published in peer-reviewed journals. Finally, chapter 7 presents several conclusions based on the previously detailed research as well as recommendations for future work along these lines.

Chapter 2 describes the preparation of α -Fe₂O₃ electrodes for photoelectrochemical (PEC) water oxidation using a technique known as reactive ballistic deposition, which was used to control the morphology and porosity of the α -Fe₂O₃ films. Iron metal was evaporatively deposited in an oxygen ambient, and synthesis parameters

such as deposition angle, film thickness, and annealing temperature were manipulated to optimize the structural and morphological properties in order to improve their PEC efficiency. Incident photon to current conversion efficiencies (IPCE) were used to calculate an AM1.5G photocurrent of 0.55 mA/cm^2 for the optimized films with an IPCE reaching 10% at 420 nm in 1M KOH at 0.5 V vs. Ag/AgCl. We also observed that the typically low photo-activity of extremely thin hematite films on fluorine-doped tin oxide substrates may be improved by modification of annealing conditions in some cases.

Chapter 3 takes this study further, detailing the modification of film composition through the incorporation of “dopants” such as titanium and tin. These doped films of $\alpha\text{-Fe}_2\text{O}_3$ were prepared by co-evaporating iron and titanium or tin in a reactive oxygen ambient, and their physical, chemical, and photoelectrochemical properties (primarily PEC water oxidation activity) were studied. It was found that manipulating the deposition angle had a profound effect on the photoelectrochemical water oxidation performance of 4% Ti-doped $\alpha\text{-Fe}_2\text{O}_3$ films, and a maximum in photocurrent at 1.4 V vs. RHE was achieved for films grown at 75° incidence. It was also found that the nanocolumnar morphology and superior porosity attained using glancing angles improved the relative conversion of visible-light ($\lambda > 420 \text{ nm}$) photons compared to dense films deposited at normal incidence. Sn-doped films were also prepared using the same deposition conditions, and although they were substantially better than undoped films, their performance was somewhat worse than that of the Ti-doped films. The Ti-doped films deposited using optimum conditions resulted in incident photon-to-current efficiencies (IPCE) reaching 31% at 360 nm and 1.4 V vs. the reversible hydrogen electrode (RHE). By comparison, Sn-doped films reached only 21% under the same conditions. The increased photo-conversion efficiency brought about through Ti^{4+} or

Sn^{4+} incorporation appears to be due to both the improvement of electron transport within the bulk of the film and the suppression of recombination at the film-electrolyte interface.

In chapter 4 the focus of the research shifts from the more widely studied binary oxide, $\alpha\text{-Fe}_2\text{O}_3$, to the novel ternary metal oxide material CuBi_2O_4 . This study also represents a deviation from the previous chapters in that it focuses on a photocathode material rather than a photoanode material. The details of this chapter concern the synthesis of visible-light active thin films of p- CuBi_2O_4 utilizing electrodeposition for the first time. Bimetallic films of copper and bismuth were deposited from a single bath onto fluorine-doped tin oxide (FTO) substrates and thermally oxidized in air. The effects of deposition parameters such as potential, time, and bath concentration on film morphology and photoelectrochemistry were investigated. In general, the films consisted of interconnected particles roughly 250 nm in diameter and showed an onset of light absorption at 680 nm (1.8 eV). The films were characterized by PEC techniques in order to provide insight into the critical PEC properties of CuBi_2O_4 such as flat-band potential, photocurrent stability and IPCE. Despite having a narrow band gap and quite suitable band edge positions for PEC H_2 generation, the films' stable calculated AM1.5G photocurrents in N_2 degassed Na_2SO_4 were relatively small ($\sim 50 \mu\text{A}/\text{cm}^2$ at 0.64 V vs. RHE) due to maximum UV quantum yields of $\sim 1\text{-}2\%$ that decreased significantly throughout the visible range, becoming negligible at about 700 nm. Studies of ballistically deposited films of CuBi_2O_4 were also performed to further demonstrate the effects of film morphology on performance. Stability tests under constant illumination revealed that the films were more unstable in acidic electrolyte (pH 3.5) due to the reduction and dissolution of Cu but were stable in basic electrolyte (pH 10.8) after an initial $\sim 50\%$ decrease in performance.

The trend toward more exotic materials continues in chapters 5 and 6, which introduce an entirely new class of materials: bismuth chalcogenides. Chapter 5 concerns the evaluation of BiOI. Bismuth oxy-iodide is a potentially interesting visible-light-active photocatalyst, yet there is little research regarding its photoelectrochemical properties. In this study, BiOI nanoplatelet photoelectrodes were deposited by spray pyrolysis onto fluorine-doped tin oxide (FTO) substrates at various temperatures. The films exhibited n-type conductivity, most likely caused by the presence of anion vacancies, and optimized films possessed incident photon conversion efficiencies of over 20% in the visible range for the oxidation of I^- to I_3^- at 0.4 V vs. Ag/AgCl in acetonitrile. Visible-light photons ($\lambda > 420$ nm) contributed approximately 75% of the overall photocurrent under AM1.5G illumination. A deposition temperature of 260°C was found to result in the best performance due to the balancing of morphology, crystallinity, impurity levels, and optical absorption, leading to photocurrents of roughly 0.9 mA/cm² at 0.4 V vs. Ag/AgCl. Although the films performed stably for up to 1 h in acetonitrile, their performance decreased significantly upon extended exposure to water, which was apparently caused by a loss of surface iodine and the subsequent formation of an insulating bismuth hydroxide layer.

In chapter 6, the oxygen atom in BiOI was replaced with sulfur and the resulting material, BiSI, was evaluated in a similar manner. Polycrystalline BiSI thin films exhibiting promising PEC properties were deposited onto both metal foils and fluorine-doped tin oxide coated glass slides by spray pyrolysis using a single solution precursor source. The films' strong light absorption in the visible range and well-crystallized layered structure gave rise to their excellent PEC performance through improved charge carrier generation and separation under simulated sunlight. The structure and surface composition of the films were dependent on deposition temperature, resulting in dramatic

differences in performance over the temperature range studied. These results reveal the potential of n-BiSI as an alternative thin film solar energy conversion material, and should stimulate further investigation into V-VI-VII compounds for these applications.

REFERENCES

1. U.S. Energy Information Administration. *International Energy Outlook 2011*.
2. British Petroleum. *Statistical Review of World Energy*, June 2011.
3. International Energy Agency. *World Energy Outlook 2010*.
4. Worldwide Solar Insolation map, generated by meteonorm 6.0, <http://www.solarfeedintariff.net/worldmap.html>, last accessed 6/26/2012.
5. National Aeronautics and Space Administration. *Global Climate Change – Key Indicators*; <http://climate.nasa.gov/keyIndicators/>, last accessed 6/26/2012.
6. U.S. Energy Information Administration. *Annual Energy Outlook 2011*.
7. National Academy of Engineering. *The Hydrogen Economy: Opportunities, Costs, Barriers, and R&D Needs*. 2004, Washington, D.C.: The National Academies Press. ISBN 0-309-53068-7. Retrieved 26 June 2012.
8. "Appendix C. Existing Hydrogen Production Capacity". *The Impact of Increased Use of Hydrogen on Petroleum Consumption and Carbon Dioxide Emissions*. U.S. Energy Information Administration. August 2008.
9. Bard, A.J.; Fox, M.A. Artificial Photosynthesis - Solar Splitting of Water to Hydrogen and Oxygen. *Acc. Chem. Res.* 1995, 28, 141-145.
10. Blankenship, R.E. et al. *Science* 2011, 332, 805-809.
11. Chen, Z. et al. *J. Mater. Res.* 2010, 25, 3-16.
12. Khaselev, O.; Turner, J.A. *Science* 1998, 280, 425-427.
13. Brillet, J.; Cornuz, M.; Le Formal, F.; Yum, J.H.; Grätzel, M.; Sivula, K. *J. Mater. Res.* 2010, 25, 17-24.
14. Kelly, N.A.; Gibson, T.L. *Int. J. Hydrogen Energ.* 2006, 31, 1658–1673.
15. Paracchino, A.; Laporte, V.; Sivula, K.; Grätzel, M.; Thimsen, E. *Nature Mater.* 2011, 10, 456-461.
16. Weber, M.F.; Dignam, M.J. *J. Electrochem. Soc.* 1984, 131, 1258-1265.
17. Nozik, A.J.; *Appl. Phys. Lett.* 1977, 30, 567-569.

18. Solar Radiation Spectrum, prepared by Robert A. Rohde, http://en.wikipedia.org/wiki/File:Solar_Spectrum.png, last accessed 07/25/2012.

Chapter 2: Reactive Ballistic Deposition of α -Fe₂O₃ Thin Films for Photoelectrochemical Water Oxidation

INTRODUCTION

Efficient solar driven hydrogen production using cheap, stable materials has been an ambitious dream for several decades, with an explosion of study originating with the suggestion of water splitting in a Pt-TiO₂ electrochemical cell in the early 1970's.¹ Due to the recent ecological and energy crises related to fossil fuel dependence such avenues for solar energy conversion have once again been thrust into the public view,² and research efforts along these lines are accelerating throughout the world with a recent emphasis on the development of novel, nanostructured materials for hydrogen production through photoelectrochemical water splitting. Due to the difficulty of discovering a single semiconductor that can simultaneously produce oxygen and hydrogen from water, a common approach is to develop and optimize semiconductor materials for the oxidation and reduction steps of the water splitting reaction independently. In this work, we employ a new technique known as reactive ballistic deposition³⁻⁶ to prepare and optimize nanostructured α -Fe₂O₃ films for the photo-oxidation of water.

In recent years a number of groups have investigated thin films consisting of vertically oriented nanocolumnar structures, which are thought to be ideal for photoelectrochemical water splitting due to their ability to absorb a significant fraction of light while still providing short charge carrier transport distances to the electrolyte, minimizing recombination losses.⁷ For example, extensive research has been performed on TiO₂ nanotube arrays produced by electrochemical anodization, and impressive

photoconversion efficiencies have been obtained, indicating that such architectures are quite useful for the photo-oxidation of water under UV irradiation.^{8,9} However, to achieve necessary solar-to-hydrogen conversion efficiencies of more than 10%,¹⁰ materials with the ability to absorb a good fraction of the visible light spectrum (> 400 nm) are needed. Hematite (α -Fe₂O₃) was introduced as a PEC material over 30 years ago, and its 2.2 eV band gap theoretically suggests that it can achieve a maximum photoconversion efficiency under solar illumination of 12.9%.¹¹ However, the best performing thin film materials developed to date fall well short of this value.¹² This is attributed to a number of factors including poor mobility of carriers, slow water oxidation kinetics, and high recombination rates compared to other semiconductors of interest such as TiO₂ and WO₃.¹³ The means of improving photocurrent response in α -Fe₂O₃ films are essentially directed at aiding charge transport in the bulk and at the surface relative to recombination in both locations. Manipulation of preparation conditions in order to optimize film properties such as morphology and crystallinity can improve rates of charge transport in the bulk, while the addition of a co-catalyst to the surface of the film can improve heterogeneous charge transfer kinetics. Doping foreign elements into α -Fe₂O₃ films can also be used to achieve similar improvements. Elements such as Si,¹² Ti,¹⁴ Sn,¹⁵ Pt,¹⁶ and others have shown the ability to increase the photoelectrochemical performance of hematite films. The use of multiple dopants simultaneously has also been investigated with some success.^{15,17} For this reason there is still hope for α -Fe₂O₃ based materials in the field of photoelectrochemical water splitting, and there has been a recent surge of activity in the preparation of such thin films by techniques including spray pyrolysis,¹⁴⁻¹⁶

chemical vapor deposition (CVD),^{12,20} electrodeposition,^{21,22} and electrochemical anodization.^{23,24}

One technique that has received some recent attention for photoelectrochemical applications is glancing or oblique angle deposition (GLAD or OAD).²⁵ The method employs a ballistic shadowing phenomenon, which occurs when a material is directionally deposited onto a relatively cool substrate at glancing angles. The initial roughening of the substrate surface caused by random variations in the local deposition rate results in small agglomerates of atoms, which begin to intercept greater and greater amounts of depositing material and shadow other regions of the surface. As this process continues, these deposits of atoms begin to form nanocolumnar structures with characteristic dimensions that depend on the deposition angle and substrate temperature used. By increasing the angle between evaporant flux and substrate surface normal (deposition angle) the films become more porous and eventually form individual nanocolumns. A number of groups have characterized this technique extensively, applying it to materials such as TiO₂,²⁶ MgF₂,²⁷ indium tin oxide (ITO),²⁸ and Pd.²⁹ GLAD techniques carried out via the directional evaporation of a metal component in an ambient reactive gas are known as reactive ballistic deposition³ (RBD), and can be used to control both composition and morphology independently. However, to our knowledge no work has been done to characterize its efficacy for producing thin films for efficient photoelectrochemistry, although recently groups have used GLAD to evaporate TiO₂³⁰ and ZnO,³¹ producing nanostructured electrodes for water splitting applications. In this

work we utilize RBD to prepare undoped $\alpha\text{-Fe}_2\text{O}_3$ films with the ultimate goal of understanding how this method may be applied to the synthesis of useful PEC materials.

EXPERIMENTAL METHODS

Film Preparation

Hematite films were deposited onto fluorine-doped tin oxide (FTO) coated glass substrates (Pilkington, TEC15) held at room temperature by evaporating Fe metal in a background of O_2 under high vacuum conditions ($\sim 10^{-6}$ torr). The vacuum chamber was first pumped down to below 5×10^{-8} torr and then backfilled to approximately 1×10^{-6} Torr with O_2 (99.99%, Matheson) using a leak valve (the majority of the remaining background is H_2O). This level of backfilling was found to be well in excess of the amount required to fully oxidize the films based on quartz crystal microbalance uptake measurements. Iron was evaporated from a 0.25" diameter rod (3N5 purity, ESPI) using an electron-beam evaporator (Tectra). The substrate holder could be rotated, allowing for utilization of the entire possible range of deposition angles (0° to 90°), and the source to substrate distance was approximately 10 cm. After deposition the samples were annealed in air at temperatures ranging from 400 to 550°C for 2 h in a box furnace (Neytech). The temperature was brought from room temperature to the desired annealing temperature at a rate of $10^\circ\text{C}/\text{min}$, and the samples were allowed to cool naturally after the desired hold time was reached.

Film Characterization

Scanning electron microscopy (SEM) was performed on a LEO 1530 SEM using a 10 kV focus voltage and on a Hitachi S-5500 Scanning Transmission Electron Microscope (STEM) using a 30 kV focus voltage. The Hitachi S-5500 was also used to perform energy dispersive X-ray spectroscopy (EDX) and transmission electron microscopy (TEM). X-ray diffraction (XRD) experiments utilized a Phillips diffractometer. UV-vis transmission spectra were taken with a Cary 5000 spectrophotometer using a blank substrate as a baseline standard. Optical penetration depths (α^{-1}) were calculated using:

$$\alpha^{-1} = -\frac{D}{\ln(T)} \quad (1)$$

Here α is the absorption coefficient, D is the thickness of the film, and T is the measured transmittance. Therefore, α^{-1} is the distance over which photons of the wavelength of interest are attenuated to an intensity equal to their original intensity multiplied by 1/e (0.368). X-ray photoelectron spectroscopy (XPS) was performed using a Kratos AXIS X-ray photoelectron spectrometer.

Electrochemical Testing

The electrochemical and photoelectrochemical properties of each sample were tested using a 3-electrode electrochemical cell with a Ag/AgCl reference electrode and Pt mesh counter electrode. The working electrode (the photoanode consisting of the α -Fe₂O₃ film) with illuminated area 0.21 cm² was immersed in 1M KOH and illuminated using an unfiltered 150 W xenon lamp (Oriel) with a white-light intensity of ~130

mW/cm². A monochromator (Oriel) was also employed to study spectral response and was used in conjunction with a power meter and photodiode (Newport) to calculate IPCE, given by:

$$\text{IPCE} = \frac{1240 \times j_{\text{ph}}}{\lambda \times I} \times 100\% \quad (2)$$

Here j_{ph} is the steady state photocurrent density, λ is the wavelength of the incident light, and I is the light power intensity at the film surface. A potentiostat (CH Instruments) was operated by a desktop computer to perform electrochemical measurements. Steady-state photocurrents for comparing the films to one another were recorded at +0.4 V vs. Ag/AgCl, whereas incident photon conversion efficiency (IPCE) experiments were performed at +0.5 V in order to maximize the ratio of illuminated current to dark current (dark currents began to increase beyond +0.5 V). Electrochemical impedance spectroscopy was performed using a Solartron frequency response analyzer and electrochemical interface system. Plots of inverse square capacitance (C^{-2}) versus potential (E) can be used to determine the flat-band potential (E_{fb}) and donor density (N_{d}) of n-type semiconductor films using the Mott-Schottky equation:

$$C^{-2} = \frac{2}{e\epsilon\epsilon_0 N_{\text{d}}} \left(E - E_{\text{fb}} - \frac{kT}{e} \right) \quad (3)$$

Here e is the elementary charge, ϵ is the dielectric constant of the electrode material, ϵ_0 is the permittivity of vacuum, and C is the capacitance of the electrode. The x-intercept of a linear fit to a plot of C^{-2} versus E reveals the flat-band potential while the slope of this fit can be used to calculate N_{d} .

RESULTS AND DISCUSSION

General Characterization

Immediately following deposition the films appeared dark brown, but after annealing for two hours at temperatures greater than 400°C the color of the films changed to reddish orange. EDX performed prior to annealing reveal that the Fe:O ratio is already close to 2:3 after removing the samples from the vacuum chamber. XRD performed on films as-deposited showed no noticeable hematite (α -Fe₂O₃) formation, revealing only the presence of a small amount of maghemite (γ -Fe₂O₃) indicating that the films are mostly amorphous before annealing. After annealing, XRD showed the presence of α -Fe₂O₃ with a preferred (104) orientation, consistent with powder standards (PDF#01-071-5088) (Figure 2.1), although some amorphous iron oxide most likely remains in the film. No other peaks other than those belonging to the fluorine-doped tin oxide (FTO) substrate could be observed. XPS confirmed that the films consisted of Fe₂O₃ after annealing (see Appendix A, Figure A.1). UV-vis transmission experiments performed on annealed films showed an absorption onset at just below 600 nm, indicating that these films possess a band gap of about 2.1 eV (Figure 2.1). The absorbance spectrum also possesses a shoulder at 540 nm and a peak at 400 nm, which are typical of α -Fe₂O₃ films and arise from indirect Fe³⁺ d to d and direct O²⁻ p to Fe³⁺ d orbital transitions.¹⁵

Electrochemical Impedance Spectroscopy

A film deposited at normal incidence (having little to no porosity) was analyzed in order to study the semiconducting properties of hematite films prepared by our

technique. Impedance spectroscopy was performed in pH 7 electrolyte using frequencies ranging from 500 to 2000 Hz and an AC amplitude of 10 mV at each potential. Some frequency dependence was observed, although the general behavior remained very similar over this frequency range. By taking the x-intercept of a linear fit to the Mott-Schottky plot for 1000 Hz (Figure 2.2), a flat-band potential of -0.27 V *vs.* Ag/AgCl (-0.07 V *vs.* NHE or +0.34 V *vs.* RHE) was estimated, which agrees well with that expected for α -Fe₂O₃.¹¹ The Mott-Schottky slope was used, assuming a dielectric constant of 80,³² to estimate a donor density on the order of 10^{17} cm⁻³. This is also in good agreement with literature values for single crystalline hematite electrodes,^{32,33} and indicates that the α -Fe₂O₃ films produced by RBD in this work possess the expected semiconducting properties of hematite.

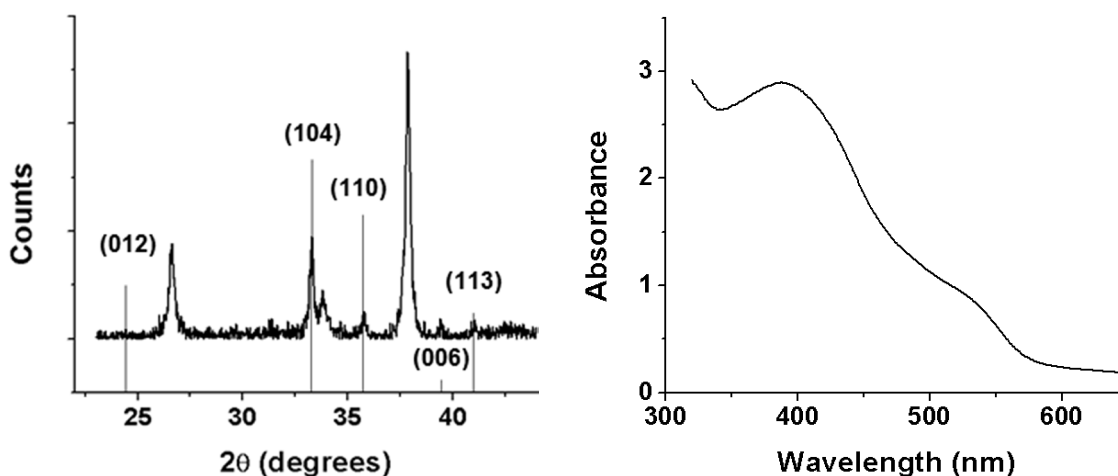


Figure 2.1. Left: X-ray diffraction of an α -Fe₂O₃ film annealed in air for 2 hr at 450°C. Lines belonging to the hematite powder diffraction pattern are included. Other visible peaks are from the FTO substrate. Right: UV-vis absorbance of an α -Fe₂O₃ film approximately 200 nm thick annealed in air for 2 hr at 450°C.

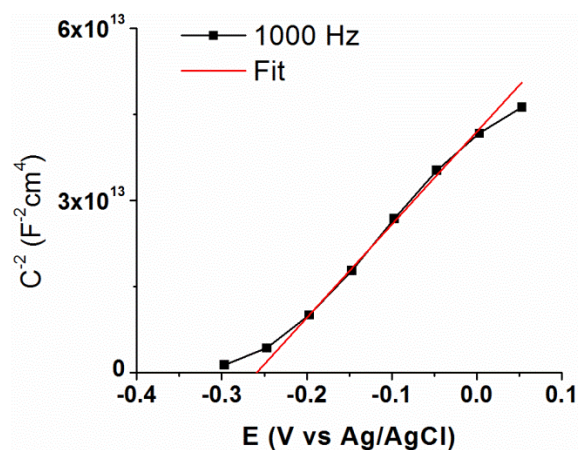


Figure 2.2. Mott-Schottky plot derived from electrochemical impedance spectroscopy performed at 1000 Hz taken at pH 7 for a film deposited at 0° and annealed to 425°C .

Deposition Angle Effects

Glancing angle deposition techniques allow for control of thin film morphologies by taking advantage of ballistic shadowing and creating porous, columnar structures of the desired material. Such structures are thought to be necessary for achieving useful water splitting efficiencies with $\alpha\text{-Fe}_2\text{O}_3$ thin films by creating a large film/electrolyte interfacial area and relatively short diffusion distances to this interface for holes generated within the bulk of the film by the absorption of photons – thus improving the rate of charge transport relative to recombination. To investigate these effects various incident angles ranging from 0° (normal incidence) to 83° were used to deposit films of iron oxide, which were then annealed in air to produce crystalline hematite. Since bulk thickness is a critical factor in determining photoelectrochemical efficiency for $\alpha\text{-Fe}_2\text{O}_3$ films, especially when effective dopants such as Si are not included,³⁴ multiple samples

of different thicknesses were prepared at each deposition angle to clarify any trends in activity.

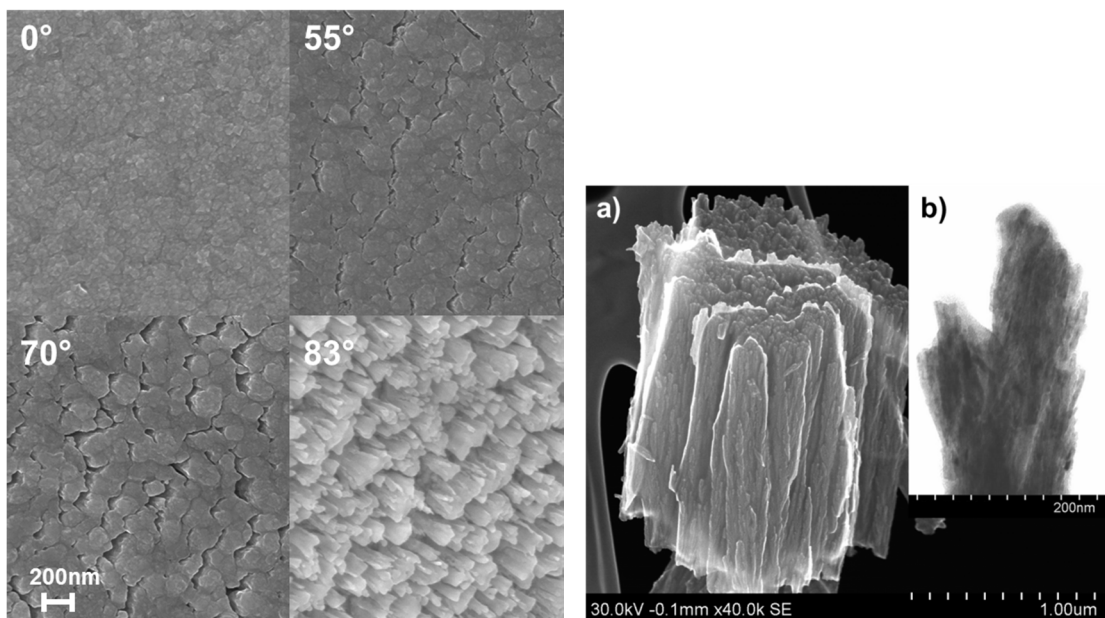


Figure 2.3. Left: SEM images of α - Fe_2O_3 films deposited at various angles and annealed to 450°C . Right: High resolution SEM of a cluster of nanocolumns (a), and bright field TEM of the top of a single nanocolumn (b). The samples were scraped off of a film deposited at 82° on FTO and were not annealed.

SEM images revealed expected differences in morphology with films deposited at normal incidence showing very little visible nanostructuring (essentially rough, dense films), and films deposited at glancing angles ($> 55^\circ$) showing more porous structures (Figure 2.3). This exemplifies the ballistic shadowing effect, which becomes more significant when glancing deposition angles and relatively low substrate temperatures are employed in a physical vapor deposition process.²⁵ Sections of films deposited at 55° and 82° were scraped off onto copper grids for TEM analyses. The 82° deposition angle

enabled examination of the surfaces of individual nanocolumns, whereas cross-sectional images of the 55° film appeared mostly dense at this level of resolution (Figure 2.3).

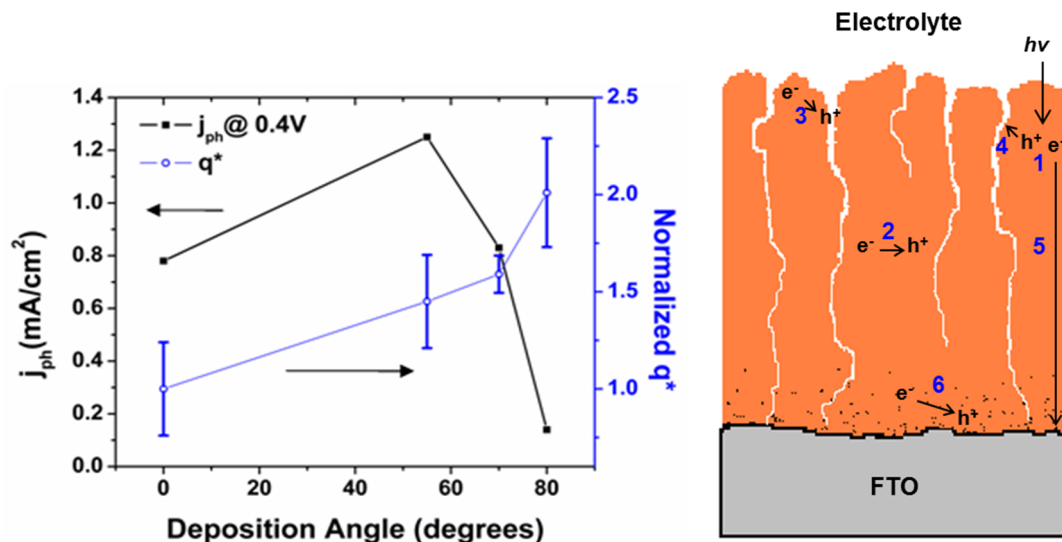


Figure 2.4. Left: Maximum steady-state j_{ph} values at 0.4 V vs Ag/AgCl for films deposited at various angles and annealed for 2 hr at 450°C plotted with the normalized voltametric charge (q^*) transferred during CV sweeps between -0.1 and 0.1 V vs Ag/AgCl in 1M KOH for films of approximately equal thickness and annealed for 2 hr at 450°C. Right: Schematic representation of processes occurring during irradiation of film. (1) light absorption and formation of electron-hole (e^-h^+) pairs; (2) bulk recombination; (3) recombination at electrolyte interface; (4) hole transport; (5) electron transport; (6) recombination at the FTO interface.

Films deposited at 55° consistently showed higher photocurrents under white light illumination than those deposited at other angles (the best performing films for each deposition angle are shown in Figure 2.4). This is a surprising result since it was expected that the more porous, nanocolumnar structures present in films deposited at more glancing angles would allow for easier hole transport to the electrolyte due to (theoretically) more optimal feature size and interfacial area. Additionally, preliminary

results obtained from TiO₂ films deposited under very similar conditions in our laboratory showed highest photocurrents when deposited at 80°. It may be that the morphology of films deposited at high deposition angles is indeed better for hole transport, but other factors such as electron transport limitations and recombination centers act to mask this improvement in the case of α -Fe₂O₃. Films deposited at more glancing angles have greater porosity and consequently larger penetration depths (smaller photon absorption probability per unit thickness) than dense films, and photon absorption deeper in the film and close to the film-substrate interface is not desired since electrons and holes generated in this region are known to suffer from higher recombination rates due to factors which will be discussed more thoroughly below. For example, the penetration depths (α^{-1}) for 420 nm photons in films deposited at 55° and 80° are approximately 27 and 66 nm, respectively, based on UV-vis transmittance experiments. In a 150 nm thick film deposited at 55°, only 15% of the 420 nm photons are absorbed in the bottom 100 nm of the film, but in an equivalent film deposited at 80°, nearly 50% would be absorbed within the bottom 100 nm, revealing that many photons would be absorbed in a layer where their probability of contributing to the photocurrent is significantly reduced. Although 100 nm is used in this example, the actual thickness and behavior of the “dead” layer is not well understood and probably depends on synthesis conditions as is investigated below. A seemingly obvious approach, then, for improving films deposited at 80° would be to significantly increase their thickness to keep so many photons from being absorbed near the FTO interface. However, now an appreciable amount of α -Fe₂O₃ lies between electrons generated near the top of the film and the

external circuit, and the poor electronic conductivity of hematite leads to a low probability for these electrons to “complete the journey” before recombining with holes. These competing factors are illustrated in figure 2.4 and may provide at least some explanation for the poor performance of high-porosity films deposited at angles above 70°, although the decrease in photocurrent as deposition angle is changed from 55° to 80° is clearly greater than what would be expected based on the preceding discussion, indicating that another factor, probably related to the concentration of surface states, must be important also.

The specific surface areas of thin films deposited by RBD can vary widely as deposition angle is changed.^{4,5} However, a better metric for evaluating thin films for PEC quality using materials with relatively poor charge transport properties like α -Fe₂O₃ may be surface area per unit thickness, since surface area improvements due to increased film thickness are not beneficial.²² Films of approximately equal thickness (180 nm) but deposited at different angles (0°, 55°, 70°, and 80°) were evaluated using cyclic voltammetry (CV). The total voltammetric charge transferred during a potential scan in which only capacitive (non-faradaic) charge transfer occurs is proportional the number of available surface sites.³⁵ Integration of the charge passed during potential cycles from -0.1 to 0.1 V vs. Ag/AgCl in 1M KOH at 20 mVs⁻¹ performed on films in the dark indicated that the electrochemically active surface area doubled as the deposition angle increased from 0° to 80° (Figure 2.4). It should be noted that the surface area of α -Fe₂O₃ *per unit mass* actually increased by nearly a factor of six over this range. In the case of the more porous films there may be some error introduced due to a contribution from

exposed FTO substrate with the electrolyte. Although 80° showed the highest surface area of the deposition angles tested, it is unknown whether even higher deposition angles would result in even higher surface areas. Various groups have shown that the deposition angle corresponding to greatest surface area for ballistically deposited films is not the same for all materials (i.e., TiO₂ shows a maximum at 70°,⁴ while Pd shows a maximum at 85°²⁹). A high surface area per unit film thickness would theoretically be advantageous for PEC water splitting since it implies that a significant fraction of the holes generated in the film will be created near the interface between the film and electrolyte, minimizing their required transport distance. However, in this study there does not appear to be a strong correlation between available surface area (on a film thickness basis) and photocurrent for the more porous films indicating that other factors such as electron transport and surface recombination limit the PEC performance of films deposited at glancing angles.

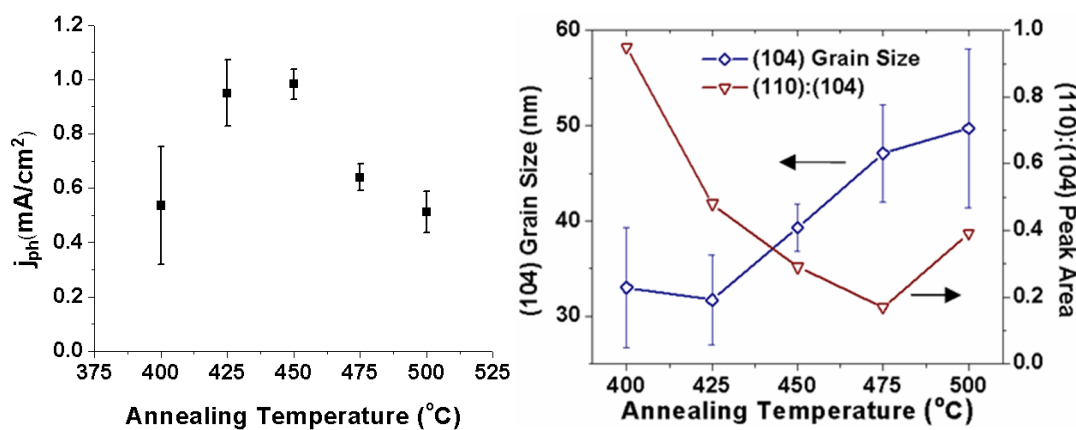


Figure 2.5. Left: Photocurrent trend at 0.4 V vs. Ag/AgCl as annealing temperature is increased for films deposited at 55° and having thicknesses of ~ 240 nm. Right: Mean crystallite size of the (104) grain size plotted along with the ratio of the (110):(104) peak areas for various annealing temperatures.

Annealing Temperature and Bulk Thickness Effects

Films with thicknesses of ~ 240 nm were deposited at 55° and annealed for 2 h in air at temperatures ranging from 400 to 500°C to investigate the sensitivity of PEC performance to post-deposition heat treatment (Figure 2.5). A significant increase in photocurrent was observed as the annealing temperature increased from 400 to 425 and 450°C , followed by a noticeable decrease for samples annealed beyond 450°C . The expected reason for the initial rise in photocurrent with annealing temperature is the improvement of crystalline order and reduction of defects within the film. This should theoretically improve charge carrier transport relative to recombination, which is a strong limiting factor in the PEC performance in undoped $\alpha\text{-Fe}_2\text{O}_3$ films. Most peaks in the XRD spectrum belonging to $\alpha\text{-Fe}_2\text{O}_3$, particularly the (104) plane, show a marked increase in intensity relative to the SnO_2 peaks as the annealing temperature increased from 425 to 500°C , indicating a general improvement in crystalline character of the $\alpha\text{-Fe}_2\text{O}_3$ film. The Scherrer equation was used to calculate the mean grain size of the (104) plane for films at each annealing temperature (Figure 2.5). As expected, the mean (104) grain size generally grows with increasing temperature, increasing from 33 nm to 50 nm over the range of annealing temperatures studied. However, this is not observed between 400 and 425°C . In fact, the only obvious difference between 400 and 425°C annealed films appears to be a *decrease* in (110) orientation relative to other planes. That this change is accompanied by a strong *increase* in photocurrent is surprising, since a preferred (110) orientation is thought to be beneficial to vertical electron transport within $\alpha\text{-Fe}_2\text{O}_3$ films due to the anisotropic conductivity of hematite, although this orientation

may not be as important as other factors.^{12,14} It is quite possible that an increase in annealing temperature from 400 to 425°C reduces the number of defects in the film, but in a way that is not easily detectable by XRD, and this is responsible for the improvement in photocurrent over this range.

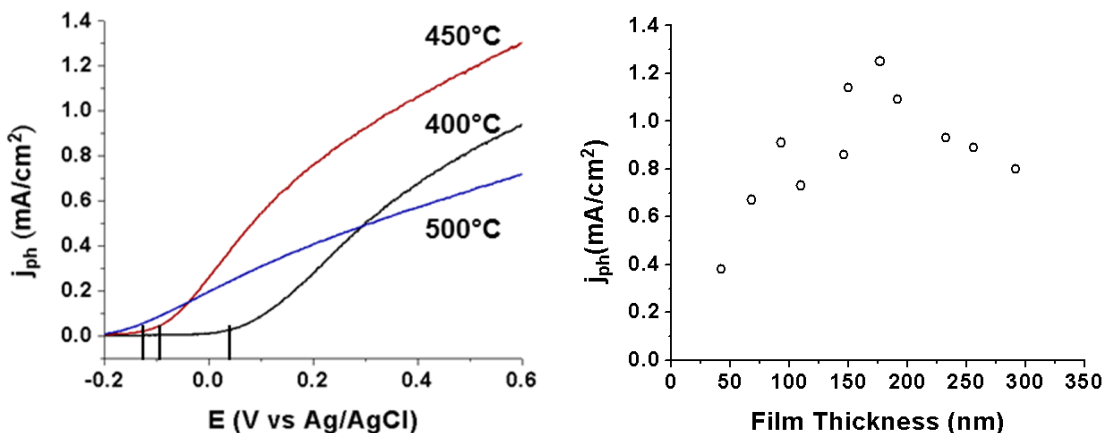


Figure 2.6. Left: Photoelectrochemical behavior under white-light illumination in 1M KOH for films annealed to various temperatures. The photocurrent onset potentials (vertical lines) tended to shift negatively as temperature increased. Right: Steady state photocurrent at 0.4 V vs. Ag/AgCl in 1M KOH for a variety of film thicknesses. Films were deposited at 55° and annealed to 450°C for 2 hr.

Although changes in crystallinity and defect concentration are likely explanations for the initial rise in photocurrent from 400 to 450°C, they do not explain the significant drop in photocurrent as the annealing temperature increases from 450 to 500°C. Since fine, nano-scale features provide improved transport to the film-electrolyte interface for holes photo-generated within the film, the agglomeration of these features and corresponding increase in hole transport distance is the most likely explanation for the decrease in performance from 450 to 500°C, although voltammetric charge integration

experiments performed on films annealed over this temperature range do not show significant differences in surface area. This method may not be precise enough to elucidate such subtle differences. Surprisingly, the decrease in performance at higher annealing temperatures is not observed for extremely thin films since the limiting factor in their performance appears to be recombination due to defects near the film-FTO interface rather than poor hole transport due increased feature size after annealing. Additionally, SEM images of the thinnest films indicate that these have a more open structure since, initially, Fe_2O_3 preferentially deposits on the peaks of the rough FTO substrate layer. In the thin film case, deposition was halted before these deposits could thicken and grow together as they normally would when employing a 55° deposition angle, causing their morphology to be somewhat different than that of the thicker films even though all other conditions were held constant.

Although photocurrent decreased when annealing temperatures increased above 450°C , a noticeable negative shift in the photocurrent onset potential was also observed (Figure 2.6). The trends in both peak photocurrent and photocurrent onset are very similar to those observed by Cesar, *et al.* for Si-doped films prepared by CVD³⁴ and annealed from temperatures ranging from 450 to 490°C . The shift in photocurrent onset was attributed to a decrease in recombination on the $\alpha\text{-Fe}_2\text{O}_3$ surface, which could be due to differences in surface area and/or the nature of surface sites. Temperature programmed desorption studies performed on MgO films³ and others produced by RBD indicate that the surface site distribution on such materials can be manipulated through annealing although it is not clear whether this effect would be significant over the

annealing temperature range studied here. It may be that the sites prevalent on α -Fe₂O₃ surfaces in the case of the lower temperature annealed films are somehow less effective from the point of view of charge transfer or recombination or the observed effects could be entirely due to a decrease in surface area as previously suggested.³⁴

A number of films were deposited at 55° with varying thicknesses in order to study the effects of film thickness on photocurrent performance. Increasing thickness allows for greater light absorption but decreases electron extraction efficiency in α -Fe₂O₃ due to poor electron transport over such distances. Indeed, the observed trend of photocurrent performance shows a volcano-like dependence on film thickness (Figure 2.6). However, the observed performance trend for very thin films annealed to 450°C does not match the corresponding photon absorbance trend. For films less than 150 nm thick the photocurrent drops off quite rapidly despite the fact that these films still absorb over 90% of the available photons in the incident light. Put another way, even the *absorbed* photon to current conversion efficiency (APCE) must be much lower for the thinner films, which is somewhat counter-intuitive since one would expect electrons generated near the surface of a thinner film to have a higher probability of reaching the back contact if all other factors remained constant. Clearly the increase in photocurrent observed as film thickness is increased to ~ 180 nm is not solely due to improved photon absorption, but may be more related to the fact that most of the electrons and holes are not generated adjacent to the film-FTO interface since it has been suggested that charge carriers generated near this interface suffer from higher recombination rates.^{34,36,37} If few photons are absorbed in this region, as is the case for thicker films, then only majority

carriers (electrons) are present near the film-FTO interface as they pass through to the back contact. Since minority carrier (hole) concentrations should be low near the interface in thick films, recombination would not be as problematic.

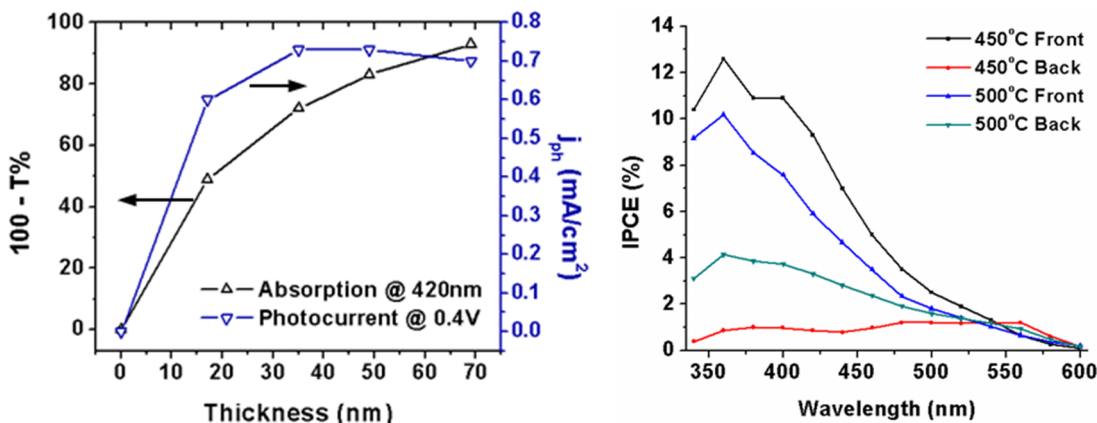


Figure 2.7. Left: Comparison of photocurrent at 0.4 V vs. Ag/AgCl and photon absorption at 420 nm trends for very thin films annealed to 550°C. Right: IPCE spectra taken at 0.5 V vs. Ag/AgCl in 1M KOH employing front and backside illumination for films deposited at 55° incidence and annealed at the indicated temperatures.

One possible reason put forth for this is the extension of electrons from the FTO substrate into the bottom layers of the α -Fe₂O₃ film,³⁶ although this effect would likely be limited to a small fraction of even the thinnest films investigated here. A more probable cause of excessive electron-hole recombination near the film-FTO interface could be crystal defects (amorphous regions, grain boundaries, strain effects, *etc.*) acting as recombination centers in the region.³⁴ It has been suggested that intermediate energy levels in α -Fe₂O₃ can be formed due to stress near the film-FTO interface and resultant lattice defects, which are then associated with electron trapping and higher recombination rates.³⁷ Extremely thin films (18 - 70 nm) were deposited and annealed to higher

temperatures (500 - 550°C) in an attempt to improve the crystalline order near the film-substrate interface. The thicknesses of these thin films were estimated by depositing thick films (which could be more easily measured), calculating their resulting film thicknesses as functions of deposited Fe mass, and using this relationship to calculate the thicknesses of thinner films prepared by depositing a known mass of Fe. However, shadowing due to the roughness of the FTO substrate causes these thin films to possess larger void fractions and be somewhat thicker than what is calculated by this method. Interestingly enough, the films annealed to higher temperatures (greater than 450°C) showed much better photoactivity than the films of similar thickness annealed to 450°C, in stark contrast to the behavior of thicker films. Films annealed to 450°C show quite different activity-thickness trends compared to those annealed to 550°C with the photocurrents of the former films leveling off at thicknesses of 180 nm, compared to only 35 nm in the latter case (Figure 2.7). The trend in performance of the films annealed to 550°C seems to match the optical absorption trend much more closely for small film thicknesses, indicating that recombination near the film-FTO interface was suppressed relative to that in films annealed to 450°C. IPCE experiments using both front and back-side illumination were performed on films deposited at 55° incidence (~ 240 nm thick) and annealed to either 450 or 500°C (Figure 2.7). For front-side experiments a blank substrate was attached to the front of the electrochemical cell to mimic the transmittance loss that would occur in the back-side illumination experiments. While films annealed to 450°C showed drastically diminished photoconversion, especially for higher energy photons, the films annealed to 500°C showed a much less precipitous drop in photo-

activity when back-side illumination was employed. The preferential recombination of higher-energy photons can be easily explained since their penetration depths are much shorter, and are thus absorbed nearer the film-FTO interface. Although clear improvements in the photoconversion of photons absorbed near the film-FTO interface were achieved using annealing temperatures higher than 450°C, the best performing films overall using front-side illumination were thicker films annealed to 450°C.

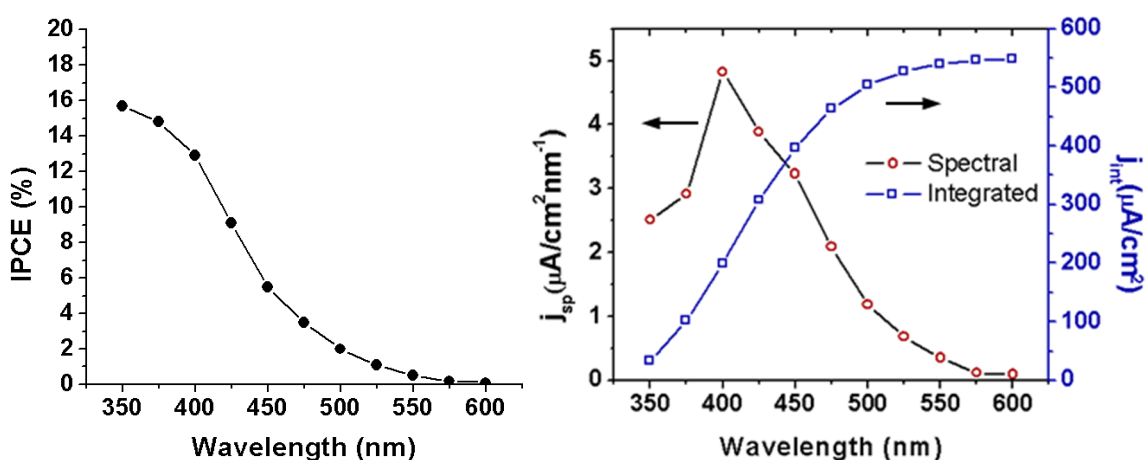


Figure 2.8. Left: IPCE spectrum of an optimized film recorded in 1M KOH at +0.5 V vs. Ag/AgCl. Right: Spectral photocurrent data under AM1.5 illumination calculated from IPCE data at +0.5 V vs. Ag/AgCl.

Photoconversion Performance

Films deposited using seemingly optimum conditions (55° deposition angle, 180 nm thick, 450°C annealing for two hours) were assessed using incident photon conversion efficiency (IPCE) calculations at wavelengths ranging from 350 nm to 600 nm at a potential of +0.5 V vs. Ag/AgCl (Figure 2.8), which is just below the onset of noticeable dark electrolysis current in 1M KOH. When integrated over the AM1.5 solar spectrum³⁸

the IPCE data results in a solar photocurrent density of $549 \mu\text{A}/\text{cm}^2$ (Figure 2.8), which is less than half of the white-light photocurrent measured under the Xe lamp irradiation used in these experiments (Figure 2.9) due to the higher intensity of the lamp illumination at the sample relative to AM1.5 as well as to the spectral mismatch between the two sources. Additionally, the filling of trap states by photons of a wide range of energies available under white-light illumination may allow for greater charge carrier mobility and thus contribute to a higher photocurrent compared to the case in which monochromatic illumination is used.

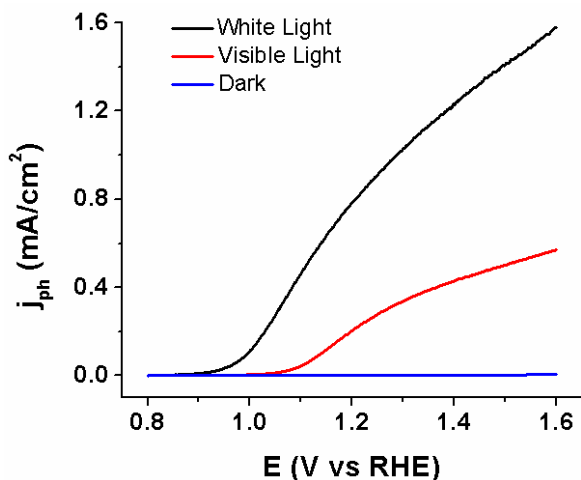


Figure 2.9. Left: IPCE spectrum of an optimized film recorded in 1M KOH at 0.5 V vs. Ag/AgCl. Right: Spectral photocurrent data under AM1.5 illumination calculated from IPCE data at 0.5 V vs. Ag/AgCl.

The photocurrent values achieved in this study are reasonable when compared with literature values for undoped $\alpha\text{-Fe}_2\text{O}_3$ prepared by various methods with most showing values in the several hundred $\mu\text{A}/\text{cm}^2$ range under AM1.5 illumination,¹⁵ although IPCE values are often not reported. The highest IPCE values reported so far for

undoped α -Fe₂O₃ films appear to belong to films prepared by spray pyrolysis with a peak IPCE of just over 20% in the UV range^{14,16} compared to 15% found in this study under similar conditions. The rapid drop-off in quantum yield beyond 400 - 420 nm has been noted by many authors and seems to occur regardless of the technique used to prepare the α -Fe₂O₃ thin film.^{34,36,39} This is a significant problem with regard to achieving practical water splitting efficiencies under solar irradiation since the bulk of the photons available to α -Fe₂O₃ lie in the 450 - 585 nm range. One possible reason for this behavior is the larger penetration depths of lower energy photons in hematite as evidenced by the UV-vis absorption spectrum, which possesses a similar shape to the IPCE spectrum. Holes generated by these photons in planar electrodes are less likely to reach the film-electrolyte interface before recombination because of the notoriously low hole diffusion distance in undoped α -Fe₂O₃ of 2-4 nm.³⁹ Nanoporous or nanocolumnar materials consisting of structures that closely match this hole diffusion length have been proposed to alleviate such problems, but in practice this strategy does not seem to significantly alter the shape of the IPCE spectrum for α -Fe₂O₃ films.³⁴ This implies that holes generated by low energy photons are somehow less inherently efficient for water oxidation than those generated by high energy photons in α -Fe₂O₃. The reasons for this are unclear, especially considering that holes generated in the O_{2p} band should seemingly relax to the lowest energy states available in the valence band (the top of the Fe_{3d} band) prior to participating in any processes at the surface of the electrode.⁴⁰ It has been hypothesized that holes created at Fe³⁺ sites are somehow less available for water oxidation than those created at O²⁻ sites, resulting in a weaker contribution to the

photocurrent.³⁹ Films tested for several minutes under constant illumination showed very little (~1%) decrease in photocurrent, and the accumulation of small bubbles could be observed on the film surface indicating that the photocurrent is due to oxygen evolution rather than photo-corrosion of the film.

CONCLUSIONS

We have reported on the use of a novel technique known as reactive ballistic deposition (RBD) for preparing and optimizing α -Fe₂O₃ thin films on FTO substrates for water splitting applications. By manipulating parameters such as film thickness, morphology, and crystallinity it is possible to tune the PEC properties of potentially interesting materials for the photo-oxidation of water such as α -Fe₂O₃. Changing the angle of deposition between 0° to 83° resulted in substantial morphological differences between the films, which played a strong role in determining their PEC performance and incident photon to current conversion efficiencies (IPCE). Various film thicknesses and annealing temperatures were also investigated in order to determine the optimum film synthesis conditions. Films approximately 180 nm thick, deposited at 55° incidence and annealed to 450°C show the highest photocurrents of those studied here for the photo-oxidation of water in 1M KOH under Xe lamp illumination. These synthesis conditions appear to balance competing effects related to photon absorption, charge carrier transport and recombination in α -Fe₂O₃ films. The optimized films of undoped α -Fe₂O₃ in this study show good performance with photocurrents exceeding 0.5 mA/cm² under solar illumination as calculated by integration of the IPCE values over the AM1.5 spectrum.

REFERENCES

1. Fujishima, A.; Honda, K. *Nature* 1972, 238, 37-38.
2. Lewis, N.; Crabtree, G. *Basic Research Needs for Solar Energy Utilization*. 2005, U.S. Department of Energy.
3. Dohnalek, Z.; Kimmel, G. A.; McCready, D. E.; Young, J. S.; Dohnalkova, A.; Smith, R. S.; Kay, B. D. *J. Phys. Chem. B* 2002, 106, 3526-3529.
4. Flaherty, D. W.; Dohnalek, Z.; Dohnalkova, A.; Arey, B. W.; McCready, D. E.; Ponnusamy, N.; Mullins, C. B.; Kay, B. D. *J. Phys. Chem. C* 2007, 111, 4765-4773.
5. Flaherty, D. W.; Hahn, N. T.; Ferrer, D.; Engstrom, T. R.; Tanaka, P. L.; Mullins, C. B. *J. Phys. Chem. C* 2009, 113, 12742-12752.
6. Flaherty, D. W.; May, R. A.; Berglund, S. P.; Stevenson, K. J.; Mullins, C. B. *Chem. Mater.* 2010, 22, 319-329.
7. van de Krol, R.; Liang, Y.Q.; Schoonman, J. *J. Mater. Chem.* 2008, 18, 2311-2320.
8. Shankar, K.; Basham, J. I.; Allam, N. K.; Varghese, O. K.; Mor, G. K.; Feng, X. J.; Paulose, M.; Seabold, J. A.; Choi, K. S.; Grimes, C. A. *J. Phys. Chem. C* 2009, 113, 6327-6359.
9. Park, J.H.; Kim, S.; Bard, A. J. *Nano Letters* 2006, 6, 24-28.
10. Bard, A. J.; Fox, M. A. Artificial Photosynthesis - Solar Splitting of Water to Hydrogen and Oxygen. *Acc. Chem. Res.* 1995, 28, 141-145.
11. Murphy, A. B.; Barnes, P. R. F.; Randeniya, L. K.; Plumb, I. C.; Grey, I. E.; Horne, M. D.; Glasscock, J. A. *Int. J. Hydrogen Energ.* 2006, 31, 1999-2017.
12. Kay, A.; Cesar, I.; Gratzel, M. *J. Am. Chem. Soc.* 2006, 128, 15714-15721.
13. Lindgren, T.; Vayssieres, L.; Wang, H.; Lindquist, S. E. Photo-Oxidation of Water at Hematite Electrodes. In *Chemical Physics of Nanostructured Semiconductors*; Bahnemann, D.W., Ed.; VSP: Utrecht, 2003; 83-110.
14. Glasscock, J. A.; Barnes, P. R. F.; Plumb, I. C.; Savvides, N. *J. Phys. Chem. C* 2007, 111, 16477-16488.

15. Jang, J. S.; Lee, J.; Ye, H.; Fan, F. R. F.; Bard, A. J. *J. Phys. Chem. C* 2009, *113*, 6719-6724.
16. Hu, Y. S.; Kleiman-Shwarscstein, A.; Forman, A. J.; Hazen, D.; Park, J. N.; McFarland, E. W. *Chem. Mater.* 2008, *20*, 3803-3805.
17. Sartoretti, C. J.; Alexander, B. D.; Solaraska, R.; Rutkowska, W. A.; Augustynski, J.; Cerny, R. *J. Phys. Chem. B* 2005, *109*, 13685-13692.
18. Duret, A.; Gratzel, M. *J. Phys. Chem. B* 2005, *109*, 17184-17191.
19. Khan, S.U.M.; Akikusa, J. *J. Phys. Chem. B* 1999 *103*, 7184-7189.
20. Hardee, K. L.; Bard, A. J. *J. Electrochem. Soc.* 1976, *123* 1024-1026.
21. Kleiman-Shwarscstein, A.; Hu, Y. S.; Forman, A. J.; Stucky, G. D.; McFarland, E. W. *J. Phys. Chem. C* 2008, *112*, 15900-15907.
22. Spray, R.L.; Choi, K. S. *Chem. Mater.* 2009, *21*, 3701-3709.
23. LaTempa, T. J.; Feng, X. J.; Paulose, M.; Grimes, C. A. *J. Phys. Chem. C* 2009, *113*, 16293-16298.
24. Mohapatra, S. K.; John, S. E.; Banerjee, S.; Misra, M. *Chem. Mater.* 2009, *21*, 3048-3055.
25. Hawkeye, M.M.; Brett, M. J. *J. Vac. Sci. Technol. A* 2007, *25*,1317-1335.
26. Xi, J. Q.; Schubert, M. F.; Kim, J. K.; Schubert, E. F.; Chen, M. F.; Lin, S. Y.; Liu, W.; Smart, J. A. *Nat. Photonics* 2007, *1*, 176-179.
27. Robbie, K., Brett, M. J.; Lakhtakia, A. *Nature* 1996, *384*, 616-616.
28. Kim, J. K.; Chhajed, S.; Schubert, M. F.; Schubert, E. F.; Fischer, A. J.; Crawford, M. H.; Cho, J.; Kim, H.; Sone, C. *Adv. Mater.* 2008, *20*, 801-804.
29. Kim, J.; Dohnalek, Z.; Kay, B. D. *Surf. Sci.* 2005, *586*, 137-145.
30. Wolcott, A.; Smith, W. A.; Kuykendall, T. R.; Zhao, Y. P.; Zhang, J. Z. *Small* 2009, *5*, 104-111.

31. Wolcott, A.; Smith, W. A.; Kuykendall, T. R.; Zhao, Y. P.; Zhang, J. Z. *Adv. Funct. Mater.* 2009, *19*, 1849-1856.
32. Kennedy, J.H.; Frese, K. W. *J. Electrochem. Soc.* 1978, *125*, 723-726.
33. Eggleston, C. M.; Shankle, A. J. A.; Moyer, A. J.; Cesar, I.; Gratzel, M. *Aquat. Sci.* 2009, *71*, 151-159.
34. Cesar, I.; Sivula, K.; Kay, A.; Zboril, R.; Graetzel, M. *J. Phys. Chem. C* 2009, *113*, 772-782.
35. Spinolo, G.; Ardizzone, S.; Trasatti, S. *J. Electroanal. Chem.* 1997, *423*, 49-57.
36. Itoh, K.; Bockris, J. O. *J. Electrochem. Soc.* 1984, *131*, 1266-1271.
37. Souza, F. L.; Lopes, K. P.; Longo, E.; Leite, E. R. *Phys. Chem. Chem. Phys.* 2009, *11*, 1215-1219.
38. NREL AM 1.5 Global solar spectrum derived from SMARTS v.2.9.2; <http://rredc.nrel.gov/solar/spectra/am1.5/>.
39. Kennedy, J.H.; Frese, K. W. *J. Electrochem. Soc.* 1977, *125*, 709-714.
40. Nozik, A.J.; Memming, R. *J. Phys. Chem.* 1996, *100*, 13061-13078.

Chapter 3: Photoelectrochemical Performance of Nanostructured Ti- and Sn-doped α -Fe₂O₃ Photoanodes

INTRODUCTION

The search for efficient, robust photocatalytic materials has persisted for nearly forty years since the ground-breaking work of Fujishima and Honda, which demonstrated the photoelectrochemical oxidation of water over an illuminated semiconducting TiO₂ film.¹ Since this discovery, countless attempts to develop materials capable of producing hydrogen *via* the “water splitting” reaction have been made with varying degrees of success. The generally quoted suggestion of the necessary solar-to-hydrogen (STH) efficiency requirement for a photoelectrochemical water splitting device stands at 10% in order for the process to attain commercial viability.² Of course, along with this conversion efficiency benchmark comes the requirement of long-term stability on the order of several years as well as reasonable affordability. To date, no material or combination of materials has been discovered that can satisfy all of these demands. Most semiconductors having favorable band-gaps and charge transport properties are quite unstable for photoelectrochemistry in aqueous solutions. For instance, Turner, *et. al.* demonstrated a monolithic p-n junction water splitting device capable of achieving 12.4% STH efficiency using optimized semiconductors for the individual water oxidation and proton reduction half-reactions, but were unable to achieve satisfactory stability.³

More recently, research has focused on improving the photo-conversion efficiency of inherently stable materials such as metal oxides through nanostructuring or other means, although these materials often either possess too wide a band gap (TiO₂, WO₃) to utilize solar light effectively or poor photo-conversion efficiency (α -Fe₂O₃). IPCE values greater than 70% have been attained for photoelectrochemical water oxidation in each of the former cases, although only at relatively short wavelengths ($\lambda <$

450 nm).^{4,5} In the latter case, however, less impressive photo-conversion efficiencies are observed for a variety of synthesis techniques.^{6,7,8} For this reason dopants such as Si,^{9,10} Ti,^{11,12} Mo,¹³ Pt,¹⁴ and Al¹⁵ have each been utilized individually to greatly improve the efficiency of α -Fe₂O₃ thin films produced by many different methods, especially in the case of Si-doping through chemical vapor deposition (CVD).⁹ In a few cases, combinations of dopants such as Ti/Al and Sn/Be have had a synergistic effect on photoelectrochemical performance.^{12,16} Despite these successes, more improvement is clearly necessary if α -Fe₂O₃ is to be utilized as a photocatalyst for water oxidation. The interest in α -Fe₂O₃ stems from its good stability in aqueous environments (pH > 3) and relatively narrow band gap (2.0-2.2 eV).¹⁷ Additionally, although its conduction band edge position is too far positive to produce hydrogen *via* the reduction of protons, it could be utilized as the photoanode for water oxidation in a tandem photoelectrochemical device.¹⁸

A number of groups have employed combinatorial techniques to rapidly screen combinations of mixed-metal or doped metal oxides.^{16,19,20,21} One recent study in particular indicated that manipulation of the Ti or Sn concentration in α -Fe₂O₃ is critical to obtaining optimum photocurrent densities, with 4 at.% (M/(M + Fe) = 0.04) giving the best water oxidation performance in both cases.¹⁶ This previous work employed a drop casting method to produce photocatalyst “spots”, which are not necessarily uniform and do not possess an optimized morphology for the photoelectrochemical oxidation of water. In the present work, reactive ballistic deposition (RBD) is employed along with glancing angle deposition (GLAD) as a film preparation technique since the co-deposition of metal sources in a desired ratio would allow for the preparation of uniform, well controlled, nanostructured thin films having the desired composition. RBD refers to the ballistic physical vapor deposition (PVD) of a material along with the simultaneous reaction of

this material with a non-directional ambient gas,^{22,23} and GLAD refers to the ballistic deposition of a material at glancing or oblique angles of incidence (70° or greater).^{24,25,26,27,28} The latter technique can be used to prepare nanocolumnar thin films by taking advantage of the self-shadowing growth mechanism arising from the preferential deposition of material on surfaces having direct line-of-sight to the deposition source. At extremely glancing angles, random islands of atoms formed during the initial stages of deposition intercept the majority of the incoming atomic flux, shadowing the regions behind them that no longer have line-of-sight to the source. As deposition continues these islands evolve into nanocolumnar structures and can be quite porous having extremely high specific surface areas approaching $800 - 1000 \text{ m}^2/\text{g}$.^{22,29,30,31} GLAD has previously been used to deposit films of TiO_2 ,^{32,33,34} ZnO ,³⁵ and WO_3 ³⁶ for solar energy conversion applications. Recently we demonstrated the preparation and optimization of nanostructured, undoped $\alpha\text{-Fe}_2\text{O}_3$ thin films using RBD technique, and the photo-conversion efficiencies of these films compare well with those produced by other methods.³⁷ For this reason along with the inherent compositional flexibility allowed by co-evaporation we thought it promising to utilize RBD to produce films of $\alpha\text{-Fe}_2\text{O}_3$ doped with promising secondary components such as Ti or Sn and investigate their performance for photoelectrochemical water oxidation.

EXPERIMENTAL SECTION

Film Preparation

Films were deposited onto fluorine-doped tin oxide (FTO) coated glass substrates (Pilkington, TEC15) held at room temperature by evaporating Fe metal along with the desired metal dopant in a background of O_2 under high vacuum conditions ($\sim 10^{-6}$ torr). The base pressure of the film deposition chamber is approximately 1×10^{-8} torr, which

was increased to approximately 1×10^{-6} torr by leaking in O₂ (99.99%, Matheson) using a leak valve. Iron and Ti were evaporated from rods (Alfa) having a minimum purity of 99.9% using one home-built and one commercial (Tetra) electron-beam evaporator. Tin was evaporated using tin shot (99.999%, Alfa) heated in a Ta crucible that was mounted in a home-built electron-beam evaporator. Deposition rates were measured prior to depositing the films using a quartz crystal microbalance (QCM, Inficon), which was mounted on a linear translator such that the QCM could be positioned directly where the substrate would be during deposition. The substrate holder could be rotated, allowing for utilization of the entire possible range of deposition angles (0° to 90°), and the source to substrate distance was approximately 17 cm for all evaporators. A diagram of the deposition scheme is shown in figure 3.1. After deposition the samples were annealed in air at 550°C for 2 hr in a box furnace (Neytech). The temperature was brought from room temperature to the desired annealing temperature at a rate of 10 °C/min, and the samples were allowed to cool naturally after the desired hold time was reached.

Film Characterization

Scanning electron microscopy (SEM) was performed on a LEO 1530 SEM using a 10 kV focus voltage and on a Hitachi S-5500 Scanning Transmission Electron Microscope (STEM) using a 30 kV focus voltage. The Hitachi S-5500 was also used to perform energy dispersive X-ray spectroscopy (EDS) for elemental analysis. Porosity (P) was calculated using the following equation:

$$P = \frac{D_p - D_d}{D_p} \times 100\% \quad (1)$$

Here D_p is the thickness of the porous film and D_d is the thickness of a dense film consisting of the same amount of deposited material. Standard X-ray diffraction (XRD)

and grazing incidence X-ray diffraction (GIXRD) experiments utilized a Bruker D8 diffractometer. UV-vis transmission spectra were taken with a Cary 5000 spectrophotometer using a blank substrate as a baseline standard. Optical penetration depths (α^{-1}) were calculated using the Beer-Lambert law:

$$\alpha^{-1} = -\frac{D}{\ln T} \quad (2)$$

Here α is the absorption coefficient, D is the thickness of the film, and T is the measured transmittance. Therefore, α^{-1} is the distance over which photons of the wavelength of interest are attenuated to an intensity equal to their original intensity multiplied by 1/e (0.368). X-ray photoelectron spectroscopy (XPS) was performed using a Kratos AXIS X-ray photoelectron spectrometer. A Veeco surface profiler was used to measure the thickness of dense films and quantify sputtering rates for XPS depth profiles.

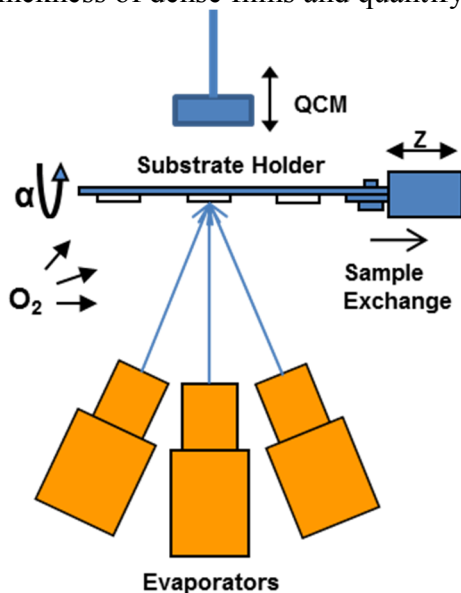


Figure 3.1. Diagram of the inside of the deposition chamber indicating the orientation of the evaporators and substrate holder.

Electrochemical Testing

The electrochemical and photoelectrochemical properties of each sample were tested using a 3-electrode electrochemical cell with a Ag/AgCl reference electrode and Pt wire counter electrode. The working electrode (the photoanode consisting of the α -Fe₂O₃ film) with illuminated area 0.21 cm² was immersed in 1M KOH and illuminated using a 100 W xenon lamp (Newport) through a UV/IR filter (Schott, KG3). A monochromator (Newport) was also employed to study spectral response and was used in conjunction with a power meter and photodiode (Newport) to calculate the IPCE, given by:

$$IPCE = \frac{1240 \times j_{ph}}{\lambda \times I} \times 100\% \quad (3)$$

Here j_{ph} is the steady state photocurrent density, λ is the wavelength of the incident light, and I is the light power intensity at the film surface. A potentiostat (CH Instruments -- CHI832) was operated by a desktop computer to perform electrochemical measurements. Electrochemical impedance spectroscopy (EIS) was performed using a CHI 660 electrochemical workstation. Plots of inverse square capacitance (C^{-2}) versus potential (E) can be used to determine the flat-band potential (E_{fb}) and donor density (N_d) of n-type semiconductor films using the Mott-Schottky equation:

$$C^{-2} = \frac{2}{e \varepsilon \varepsilon_0 N_d} \times \left(E - E_{fb} - \frac{kT}{e} \right) \quad (4)$$

Here e is the elementary charge, ε is the dielectric constant of the electrode material, ε_0 is the permittivity of vacuum, and C is the capacitance of the electrode. The x-intercept of a linear fit to a plot of C^{-2} versus E reveals the flat-band potential while the slope of this fit can be used to calculate N_d .

RESULTS AND DISCUSSION

Preliminary Characterization

XRD profiles for 0% and 4% Ti doped films roughly 360 nm thick are shown in figure 3.2a. Only a slight increase in the relative peak intensities of the hematite (PDF# 97-002-4004) (110) and (113) planes could be observed in the doped film. An enhancement in the (110) orientation of the film could provide for improved electron transport vertically through the film due to the higher conductivity normal to this plane relative to others in hematite, although this may be a minor effect.^{9,11} UV-vis spectra for 180 nm thick films deposited at 75° with 0 and 4% Ti are shown in figure 3.2b. Both spectra show features typical of α -Fe₂O₃ films with an absorption onset of about 575 nm (2.2 eV), shoulder at 540 nm (2.3 eV), and peak at 430 nm (2.9 eV), which are due to the well-known indirect Fe³⁺ 3d - 3d and direct O²⁻ 2p - Fe³⁺ 3d transitions.³⁸ No obvious changes in the optical absorption of α -Fe₂O₃ caused by Ti incorporation could be observed at these concentrations. Different background O₂ pressures were also employed during the deposition of Ti-doped films at 75° to see if any differences in film crystallography arose. The ratio of O₂ to Fe atomic flux was varied between 0:1 and 20:1, and all samples were subjected to the standard 2 hr, 550°C heat treatment in air. The GIXRD results for these samples showed no evidence for other iron oxide phases besides hematite, and there was little to no discernible trend in the preferred orientation of the films with all showing (104) as the dominant diffraction peak (see Appendix B, Figure B.1).

Electron Microscopy

To study the effect of morphology on the performance of Ti-doped α -Fe₂O₃ films, various deposition angles ranging from 0° to 80° were used employing a Fe:Ti deposition

ratio of 24:1 (4% Ti) as determined by QCM calibration before each growth. This composition was selected based on the previously mentioned combinatorial screening results.¹⁶ Two to three films were deposited at each angle. All film thicknesses were maintained at about 180 nm, and the porosity of the films could thus be determined by calculating the total number of iron and titanium atoms deposited using the QCM calibration and comparing this to the number of metal atoms required to deposit a dense film at normal incidence of the same thickness (see equation 1). The porosities of the films deposited at 55°, 70°, 75°, and 80° are estimated (employing equation 1) to be approximately 12%, 35%, 47%, and 60%, respectively, after annealing to 550°C. These values roughly agree with expected trends in porosity evolution in films prepared by GLAD as calculated from geometric considerations.³⁹

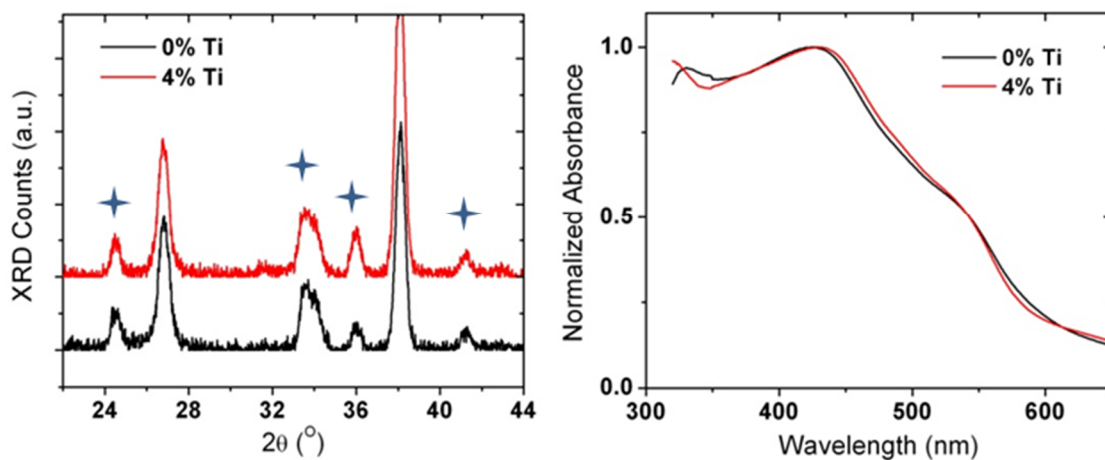


Figure 3.2. Left: XRD profiles for films deposited at 75° incidence having thicknesses of approximately 360 nm and annealed to 550°C for two hr both with and without 4% Ti incorporation. Expected peak locations for hematite (PDF #97-002-4004) are indicated by stars. Right: UV-vis absorbance spectra for films deposited at 75° incidence, also with and without 4% Ti incorporation.

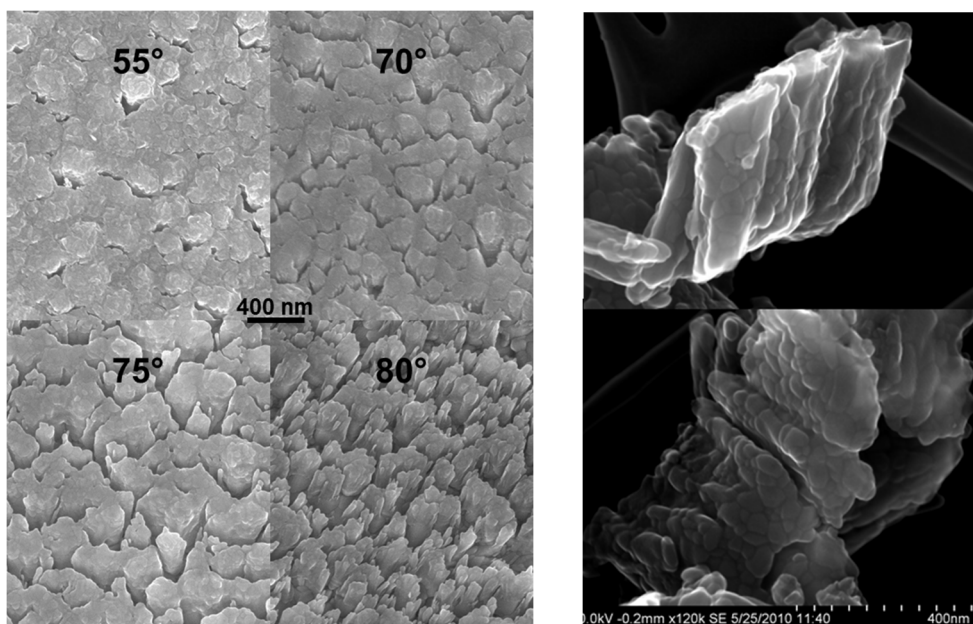


Figure 3.3. Left: SEM images of 4% Ti-doped films approximately 180 nm thick and deposited at various angles. Right: HRSEM images of sections of 4% Ti-doped films deposited at 75° incidence.

SEM images of representative samples are shown in figure 3.3. The appearances of the doped films are quite similar to those of undoped $\alpha\text{-Fe}_2\text{O}_3$ deposited at the same angles, indicating that this level of Ti incorporation had little to no effect on their morphology.³⁷ High-resolution SEM images of sections of a 360 nm film deposited at 75° incidence and scraped off onto a lacey carbon grid are shown in figure 3.3 in order to provide a clearer view of the film morphology. The individual hematite crystal grains are clearly visible at this level of resolution. The effect of the high annealing temperatures on nanoscale morphology is somewhat noticeable when the SEM image of a Ti-doped film deposited at 75° and annealed at 400°C (the lowest temperature at which these $\alpha\text{-Fe}_2\text{O}_3$ films could be crystallized) is compared to one annealed at 550°C (see Appendix B, Figure B.2). This reduction of nanoscale features and corresponding loss of surface area theoretically decrease photoconversion efficiency, but the poorer performance of

films annealed to temperatures less than 550°C indicates that superior crystallinity and/or a reduced number of surface defects overcome this drawback at higher temperatures.

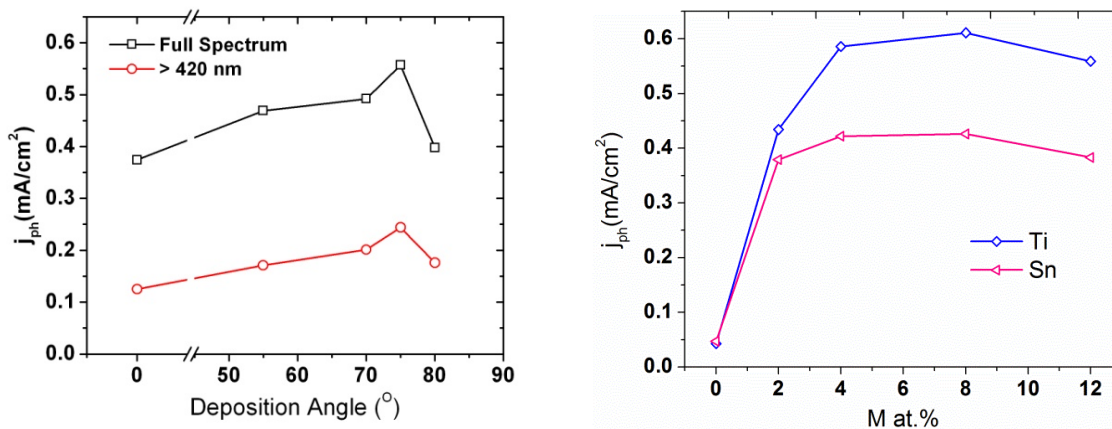


Figure 3.4. Left: Photocurrent at 1.4 V vs. RHE for 4% Ti-doped films deposited at various angles. Right: Photocurrent at 1.4 V vs. RHE for different doping levels of Ti or Sn.

Water Oxidation Performance

The water oxidation performance in 1M KOH for films deposited at various angles from 0° to 80° and annealed to 550°C is shown in figure 3.4. Films deposited at 75° incidence showing significantly higher photocurrents at 0.4 V vs. Ag/AgCl (1.4 V vs. RHE) than those deposited at other angles. These films show over 50% greater white light photocurrent than films deposited at 0° incidence (585 vs. 375 $\mu\text{A}/\text{cm}^2$). At this potential the band-bending within the film should be quite strong, allowing the bulk solid-state processes within the film to dominate the photocurrent response, rather than charge transfer limitations at the surface.³⁸ The strong photocurrent response of Ti-doped films deposited at very glancing angles (75° and 80°) is quite different from what was observed for undoped $\alpha\text{-Fe}_2\text{O}_3$ films, which only performed well when deposited at angles $\leq 70^\circ$.³⁷ This may be a result of the suppression of recombination at the surface,

which is a greater problem at more glancing angles, possibly due to a larger number of surface defects as discussed in more detail below.

Typically, the photocurrent enhancement by the substitution of Ti^{4+} for Fe^{3+} is thought to arise from the improvement of electron transport in bulk $\alpha\text{-Fe}_2\text{O}_3$,⁹ which is carried out by a polaron hopping mechanism in which electrons hop from Fe^{2+} to Fe^{3+} sites *via* thermal activation rather than by free conduction, hence the poor measurable electron mobility reported in the literature.³⁸ It has been observed that the charge compensation of incorporated Ti^{4+} (or M^{4+} in general) *via* the reduction of additional Fe^{3+} species to Fe^{2+} increases the n-type conductivity of $\alpha\text{-Fe}_2\text{O}_3$ single crystals and films.³⁸ Another effect of increasing the donor density by Ti^{4+} incorporation is a reduction of the depletion layer width, which should increase the strength of the electric field within the semiconductor near the film-electrolyte interface and improve the separation of photogenerated charge carriers in this region. The passivation of recombination at grain boundaries has also been suggested as a possible reason for the improved photo-conversion efficiency of Ti or Si-doped $\alpha\text{-Fe}_2\text{O}_3$ films.¹¹

Films of 4% Ti-doped Fe_2O_3 that were deposited at 75° with a thickness of 360 nm showed almost identical performance to the 180 nm films, whereas films of undoped $\alpha\text{-Fe}_2\text{O}_3$ produced by RBD showed diminishing activity as their thickness was increased beyond 180 nm.³⁷ This reveals that vertical electron transport through the film is improved by Ti-doping. Cesar, *et al.* showed that Si-doped $\alpha\text{-Fe}_2\text{O}_3$ electrodes produced by CVD did not suffer from a decreased in photocurrent for films as thick as 700 nm, which was also quite different from the behavior of their undoped $\alpha\text{-Fe}_2\text{O}_3$ films.⁴⁰ The addition of a +4 dopant in these cases appears to improve electron transport from the top of the film to the conductive substrate.

In order to test another +4 dopant, Sn was evaporated along with Fe using a Sn:Fe ratio of 1:24 (4% Sn-doping). The incorporation of Sn⁴⁺ was confirmed by XPS (see Appendix B, Figure B.3). These films were deposited at 75° incidence and had thicknesses of ~ 180 nm. There was a clear increase in the performance of the Sn-doped films relative to undoped films prepared using the same conditions, although they still fell short of the Ti-doped films. Films with even higher Sn concentrations (up to 12%) were prepared, but 4 – 8% appeared to be the optimum range for both Sn and Ti (Figure 3.4).

The differences in performance between the Ti and Sn-doped electrodes might be related to the size of the dopant ion. A recent study on Al³⁺ doped Fe₂O₃ used density functional theory (DFT) calculations to show that a contraction of the hematite lattice volume could enhance its polaronic conductivity to some extent by improving the rate of carrier hopping between cations.¹⁵ However, in that behavior was only explicitly predicted for iso-valent doping in α -Fe₂O₃ (substituting a foreign +3 species for Fe³⁺). The ionic radii of Ti⁴⁺ and Sn⁴⁺ are 61 and 69 pm, respectively (Fe³⁺ is 65 pm). It may be reasonable to expect that as long as the hematite crystal structure is maintained, substituting a smaller +4 species such as Ti⁴⁺ for Fe³⁺ could induce similar changes in unit cell volume, enhancing polaronic conductivity and, assuming conduction remains dominated by polarons, the photocurrent. Conversely, substituting the larger Sn⁴⁺ ion for Fe³⁺ would not have this benefit, which lessens its positive impact on photoelectrochemical performance compared to Ti-doping. Berry, *et al.* found that doping α -Fe₂O₃ with Sn or Ti did in fact alter the unit cell volume in the manner expected (slight increase for Sn and slight decrease for Ti) when 10% of the dopant was incorporated *via* the hydrothermal method.⁴¹ In the present work XRD measurements of 12% Ti films seem to reveal a slight contraction of the (110) d-spacing relative to 12% Sn films as indicated by a slight increase in the 2 θ value for the (110) diffraction peak (see

Appendix B, Figure B.4). However, these films showed somewhat worse performance than those doped with only 4% Ti or Sn, and the much more prominent (104) peak of 12% Ti doped α -Fe₂O₃ films may indicate that superior overall crystallinity is the more critical factor. Interestingly, the best performing α -Fe₂O₃ films to date are doped with Si⁴⁺,⁹ which has an ionic radius of only 40 nm - far smaller than any transition metal +4 species, indicating that the size of the dopant atom may indeed have an effect on the photoelectrochemical performance. However, another reason for the photocurrent enhancement by reducing dopant size could be an improved ability to incorporate at interstitial sites or to diffuse to and passivate grain boundary states.

Chemical Characterization

The incorporation and distribution of Ti atoms was characterized using EDS and XPS techniques. To perform EDS, a 360 nm thick film deposited at 75° incidence was scraped off of the FTO substrate and deposited on a TEM grid so that the distribution of Ti could be observed. EDS line scans indicate that the distribution of Ti is fairly uniform along the nanocolumnar structures (Figure 3.5) with no obvious signs of segregation. This is quite different from the behavior observed for dense films, in which Ti was segregated quite far from the surface during annealing (see Appendix B, Figure B.5). XPS performed on a film deposited at 75° incidence having 4% Ti and annealed to 550°C reveals that Ti is in the +4 state as evidenced by the 2p_{1/2} and 2p_{3/2} peaks present in the Ti 2p spectrum at 458.5 and 464 eV, respectively (Figure 3.6). The Fe 2p spectrum, also shown in figure 3.6, possesses the typical 2p_{1/2} and 2p_{3/2} peaks of Fe³⁺. The calculated concentration of Ti (on a metals basis) from the XPS spectra of O, Ti, and Fe is 3.5%. Although some evidence for the reduction of Fe³⁺ to Fe²⁺ would be expected from the substitution of 3.5% Ti⁴⁺ for Fe³⁺, no Fe²⁺ satellite peaks at 715 or 730 eV could be

observed. This may be because the overall atomic concentration of Ti is quite low (1.33%), and only a small amount of the Ti^{4+} ions are compensated for by the formation of Fe^{2+} ions. On the other hand, any Fe^{2+} species present may simply not remain in this state at the surface due to the oxidizing annealing conditions employed here.

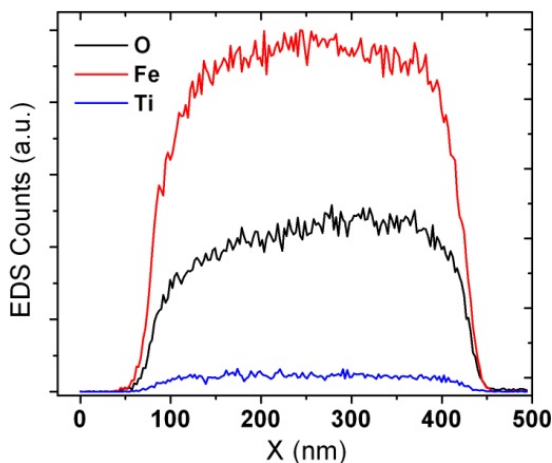


Figure 3.5. Vertical EDS line scan of a section of 4% Ti-doped film deposited at 75° incidence.

A number of groups have investigated the doping of Ti into $\alpha\text{-Fe}_2\text{O}_3$ from both theoretical and experimental perspectives to attempt to explain how Ti is incorporated and how this incorporation affects the electronic structure of the parent hematite material. The hematite lattice consists of a hexagonally close-packed array of O^{2-} ions with Fe^{3+} ions occupying 2/3 of the associated octahedral sites, and in general Ti^{4+} (or other cationic dopant) ions may substitute for Fe^{3+} ions at these octahedral sites and/or occupy interstitial octahedral sites. Authors have suggested that the most energetically favorable process is one in which groups of three Ti^{4+} ions are incorporated as “defect clusters” at both substitutional and interstitial octahedral sites with the removal of four Fe^{3+} ions as the charge compensating mechanism.⁴² Others have calculated that in the substitutional

case the extra electron from Ti^{4+} is likely to be localized on an adjacent Fe^{3+} species, reducing it to Fe^{2+} and giving the typically observed increase in n-type conductivity upon M^{4+} substitution.⁴³ The former observation is based on a relatively large dopant concentration ($\text{M}/(\text{M}+\text{Fe}) = 0.2$) whereas the latter considers $\text{M}/(\text{M}+\text{Fe}) = 0.04$, which could account for the difference in their conclusions. In the present work no reduction to Fe^{2+} is observed using XPS, but this could be due to differences at the surface and may not be indicative of the bulk state of Fe.

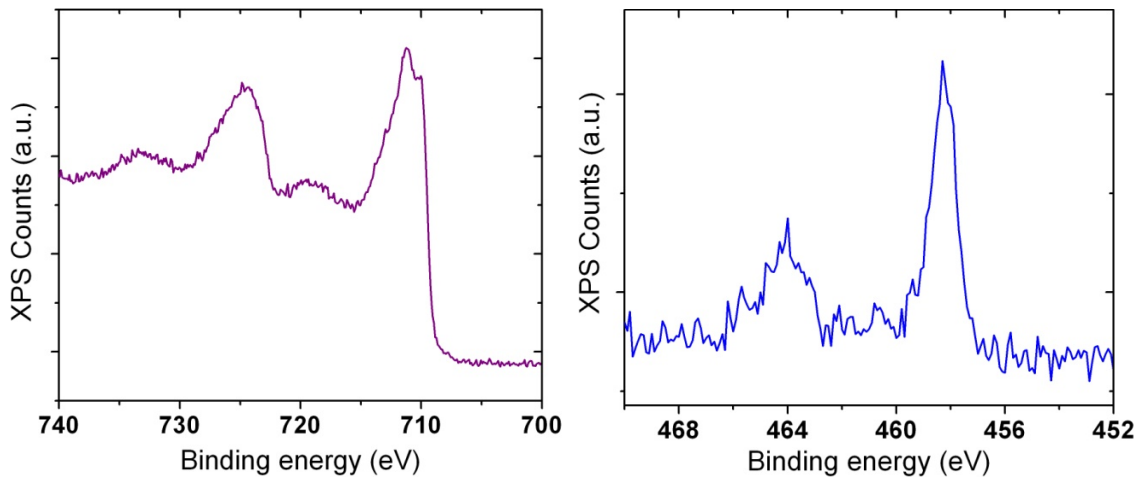


Figure 3.6. XPS spectra of a 4% Ti-doped film deposited at 75° incidence. Left: Fe 2p region. Right: Ti 2p region.

Mott-Schottky Analysis

Electrochemical impedance spectroscopy (EIS) was employed to study the electronic properties of both Ti-doped and undoped films deposited at 75° incidence. The films were analyzed in the dark at pH 13.5. In order to minimize the effect of exposing bare FTO to the electrolyte a thin (~ 6 nm) dense layer of iron oxide was deposited on the substrate at normal incidence before depositing the nanocolumnar films. Representative Mott-Schottky plots for films containing 0% and 4% Ti are shown in figure 3.7. A minor

dependence on AC frequency was observed, and the plots displayed in figure 3.7 were recorded at 1000 Hz. Films both with and without Ti showed super linear behavior similar to what was observed for Si-doped α -Fe₂O₃ films by others, which was attributed to a decrease in the active surface area of nanostructured films as a function of potential.⁴⁰ The theory is that as nano-scale features on the surface become fully depleted they no longer contribute to the effective capacitive surface area, resulting in a changing capacitance with potential. The slope in the quasi-linear regions of the Mott-Schottky plots near E_{fb} (between -0.4 and -0.55 V vs. Ag/AgCl) where the depletion layer remains very thin and results in a nearer approximation to a flat-plate electrode was used to calculate donor densities of 2.0×10^{19} and 1.2×10^{20} cm⁻³ for the undoped and 4% Ti-doped films, respectively. The value calculated for the undoped film deposited at 75° incidence is much higher than that calculated in a previous work for a film deposited at normal incidence (1×10^{17} cm⁻³).³⁷ Clearly the nanostructured morphology affects the calculated donor density. The apparent donor density of the Ti-doped film is approximately 9×10^{19} cm⁻³ greater than that of the undoped film, and if an Fe³⁺ density of 4×10^{22} cm⁻³ is assumed for hematite this represents a donor incorporation of only 0.23% - much lower than the bulk incorporation level of Ti measured by XPS and EDS. This could mean that only a small fraction of Ti⁴⁺ incorporation results in the reduction of Fe³⁺ to Fe²⁺ and that the rest is compensated *via* the defect clusters involving Fe³⁺ vacancies suggested by Berry, *et al.*⁴² Flat-band potentials (E_{fb}) of -0.61 V vs. Ag/AgCl (0.41 V vs. RHE) and -0.62 vs. Ag/AgCl (0.38 V vs. RHE) were calculated for the undoped and 4% Ti-doped electrodes, respectively, showing that the E_{fb} was not significantly affected by Ti incorporation.

The increased donor density as a result of Ti-doping decreases the space-charge layer thickness and consequently strengthens the electric field near the film-electrolyte

interface for a given applied potential, which should lead to more effective separation and transport of electrons and holes at this interface and may be significant reason for the improvement in photocurrent response. However, doping with Sn^{4+} increased the donor density by a similar amount yet did not improve the photocurrent response to the same degree, meaning other characteristics of Ti cause it to be a superior dopant in RBD grown $\alpha\text{-Fe}_2\text{O}_3$ films.

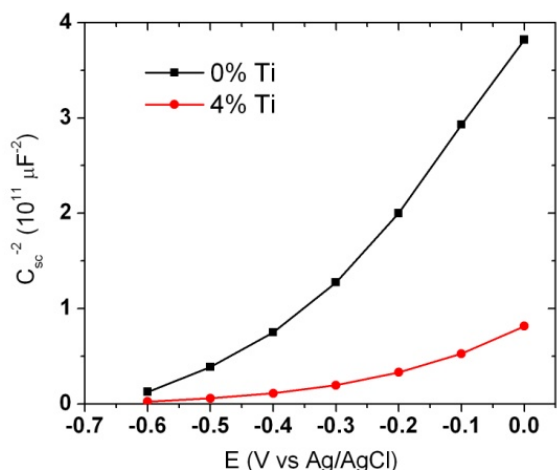


Figure 3.7. Mott-Schottky plots in 1M KOH for films deposited at 75° incidence on top of a dense blocking layer deposited at 0° incidence.

Deposition Angle Effects

Several different photoelectrochemical tests were performed to elucidate the effects of deposition angle on the photocurrent response of the 4% Ti-doped $\alpha\text{-Fe}_2\text{O}_3$ electrodes. Light chopping experiments were performed between 0.6 and 1.6 V vs. RHE to study transient photocurrent response. For all films the ratio of transient to steady-state photocurrent decreased with increasing applied potential, which is a well-documented behavior on semiconductor electrodes and on $\alpha\text{-Fe}_2\text{O}_3$ in particular.³⁸ The generally accepted theory is that when a photoanode is illuminated there is an initial buildup of intermediate oxidation products on the electrode surface, and as their

concentration increases during this initial period they begin to scavenge photoelectrons generated and/or trapped at the surface resulting in a cathodic current that decreases the observed anodic current until a steady-state balance is achieved.³⁸ Once illumination is halted this cathodic current persists until the intermediates are exhausted, resulting in cathodic current spikes when the light is blocked. The extent of these recombination events is probably related to the number of electron trap sites on the electrode surface since electrons located in these traps are unable to migrate away from the surface under mildly depleting conditions (at lower applied potentials) and are left to react with a surface electron scavenger.⁴⁴ Under high band-banding conditions more of these electrons are able to escape these surface states *via* the stronger electric field and thus avoid being scavenged. The ratio of transient to steady-state photocurrent at a given potential, then, may reveal whether the surface trapping of electrons and subsequent back reaction are significant limiting factors for the water oxidation performance of a given film.

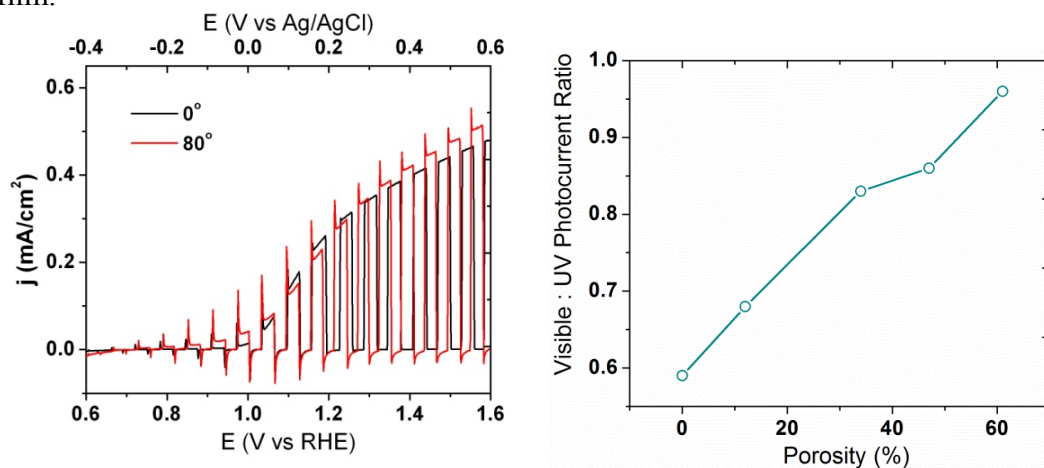


Figure 3.8. Left: Chopped light experiments using full spectrum illumination for 4% Ti-doped films deposited at 0° and 80° incidence. Right: Ratio of visible-light to UV-light contributions to the photocurrent at 1.4 V vs. RHE as a function of the calculated porosity of 4% Ti-doped films deposited at angles ranging from 0° to 80°.

In this work a positive trend in the transient to steady-state photocurrent ratio was observed as deposition angle was increased, indicating that films deposited at more glancing angles possess a greater number of surface defects and traps, thus limiting the steady-state photocurrent, most notably at lower potentials. As an example, j-E curves under chopped illumination for films deposited at 0° and 80° incidence are shown in figure 3.8. However, although surface recombination appears to be a more significant problem in the films deposited at glancing angles, their morphologies appear to facilitate better bulk charge separation and transport as evidenced by the higher transient photocurrents (that is, before back reaction becomes a significant problem). Interestingly, films deposited at 75° but without Ti incorporation exhibit very large transient to steady state photocurrent ratios even compared to the Ti-doped films deposited at 80°, which may indicate that the stronger band-bending near the surface of the film as a result of doping drives electrons away from surface traps more readily, and they are less likely to react with surface species. Alternatively this could be a surface state passivation effect. This was also observed for Sn-doped films.

Another trend that was observed as deposition angle increased was in the relative contribution of visible and UV photons to the front-side photocurrent. Due to its indirect band gap an α -Fe₂O₃ film does not absorb visible photons ($\lambda > 420$ nm) with a high probability resulting in significantly longer α^{-1} as the wavelength of incident photons is increased. For example, the α^{-1} of a 470 nm photon is twice that of a 370 nm photon in α -Fe₂O₃ (50 vs. 25 nm), as measured for a dense film. A highly porous or nanocolumnar film allows more of these more deeply penetrating visible photons to be absorbed relatively close the electrolyte interface since this interface permeates through much of the film, decreasing the required transport distance of the resulting photoholes and reducing their probability of recombining with electrons in the bulk. The ratio of visible

to UV photocurrent was observed to increase with increasing deposition angle. In fact, when plotted against the estimated porosity of the films it shows an almost linear dependence over this range of porosities (Figure 3.8). This seems to indicate that the nanostructuring brought about by utilizing more glancing angles improves the relative conversion of photons absorbed more deeply within the film, which helps to increase the visible-light conversion efficiency of Ti-doped α -Fe₂O₃.

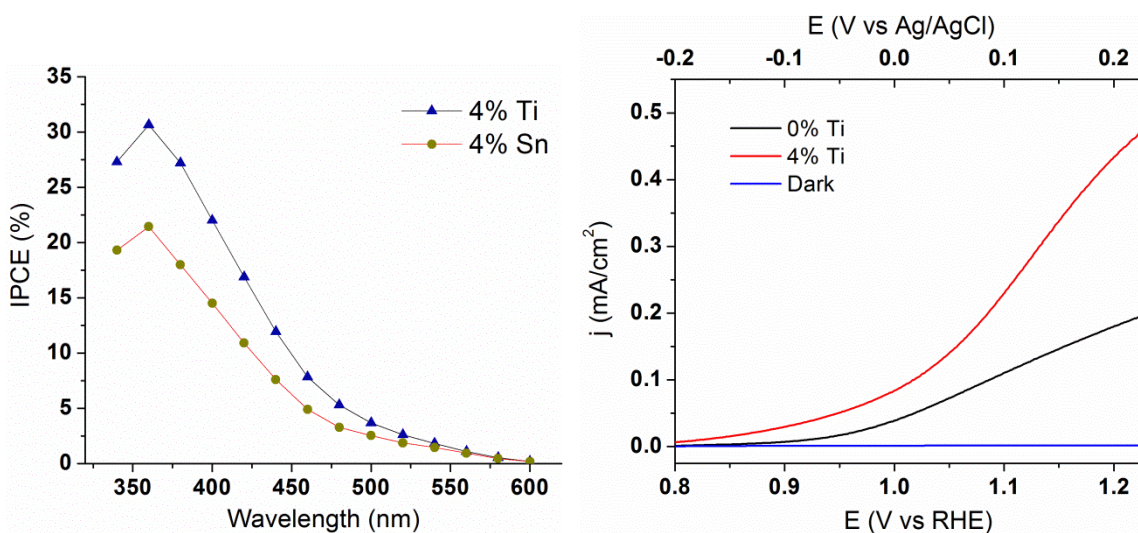


Figure 3.9. IPCE performance at 1.4 V vs. RHE for films deposited at 75° incidence with either 4% Ti or 4% Sn. Right. Photoelectrochemical j-E curves comparing the performance of an optimized 4% Ti doped film (75° incidence, 550°C anneal) to an optimized undoped film (55° incidence, 450°C anneal) at lower applied potentials under full spectrum illumination.

Photoconversion Efficiency

IPCE tests were performed in 1M KOH to evaluate the spectral response for water oxidation between 340 and 600 nm of the Ti-doped and Sn-doped α -Fe₂O₃ deposited at 75° (Figure 3.9). Using a potential of 1.4 V vs. RHE the Ti-doped film reached IPCE values of 31% and 17% at 360 and 420 nm. Unfortunately these values dropped significantly at longer wavelengths (i.e. < 4% at 500 nm), indicating that the conversion

of photons in the green to yellow region of the visible spectrum is still quite poor. The Sn-doped film reached IPCE values of 21% and 11% at the same wavelengths. When the IPCE values are integrated over the AM1.5 solar spectrum⁴⁵ they result in solar photocurrents of 0.94 and 0.63 mA/cm², respectively, which, although superior to previously reported films of Ti-doped α -Fe₂O₃ (0.57 mA/cm²),¹¹ still fall well short of Si-doped photoanodes showing greater than 2.0 mA/cm².⁴⁰ Both films performed much better than the best undoped films studied in our previous work on α -Fe₂O₃ prepared by RBD, which reached only 16% at 350 nm using a slightly more positive applied potential of 1.5 V vs. RHE.³⁷ Since in a realistic photoelectrochemical system lower applied potentials would be employed, it is important to note that this improvement in performance due to doping is not solely evident at very positive potentials (> 1.23 V vs RHE). In fact, optimized Ti-doped films outperform optimized undoped films over the entire range of potentials tested by a factor of two or more (Figure 3.9).

CONCLUSIONS

Reactive ballistic deposition (RBD) was employed along with glancing angle deposition (GLAD) to deposit nanostructured films of M-doped α -Fe₂O₃ by evaporating Fe and Ti or Sn simultaneously in vacuum by e-beam bombardment. Titanium doping resulted in a higher photocurrent when each were incorporated at a level of approximately 4 at.%. Incorporating M⁴⁺ into α -Fe₂O₃ appears to improve charge transport while decreasing recombination both in the bulk and on the surface of the film. The effects of doping with Ti were investigated further while manipulating the morphology and porosity of the films by varying the deposition angle. A clear effect of the deposition angle on the photocurrent at 1.4 V vs. RHE could be observed with a deposition angle of 75° giving the highest value under Xe lamp illumination.

Additionally, porous films deposited at glancing angles showed a greater contribution of visible light ($\lambda > 420$ nm) photons to the photocurrent. IPCE results for the optimized films show good conversion of UV photons at 1.4 V vs. RHE, with quantum yields exceeding 30% at 360 nm, but the visible light conversion efficiency, although somewhat improved by nanostructuring, remains poor, limiting the films' AM1.5 photocurrent significantly.

REFERENCES

1. Fujishima, A.; Honda, K. *Nature*. **1972**, *238*, 37-38.
2. Bard, A. J.; Fox, M. A. *Accounts Chem. Res.* **1995**, *28*, 141-145.
3. Khaselev, O; Turner, J.A. *Science* **1998**, *280*, 425-427.
4. Varghese, C. K.; Paulose, M.; Shankar, K.; Mor, G. K.; Grimes, C. A. *J. Nanosci. Nanotechnol.* **2005**, *5*, 1158–1165.
5. Santato, C.; Ulmann, M.; Augustynski, J. J. *Phys. Chem. B* **2001**, *105*, 936-940.
6. Khan, S. U. M.; Akikusa, J. J. *Phys. Chem. B*, **1999**, *103*, 7184-7189.
7. Prakasam, H. E.; Varghese, O. K.; Paulose, M.; Mor, G. K.; Grimes, C. A. *Nanotechnology* **2006**, *17*, 4285–4291.
8. LaTempa, T. J.; Feng, X.; Paulose, M.; Grimes, C. A. *J. Phys. Chem. C* **2009**, *113*, 16293–16298.
9. Kay, A.; Cesar, I.; Gratzel, M. J. *Am. Chem. Soc.* **2006**, *128*, 15714-15721.
10. Liang, Y.; Enache, C. S.; van de Krol, R. *Int. J. Photoenergy* **2008**, Article ID 739864.
11. Glasscock, J. A.; Barnes, P. R. F.; Plumb, I. C.; Savvides, N. J. *Phys. Chem. C* **2007**, *111*, 16477-16488.
12. Sartoretti, C. J.; Alexander, B. D.; Solarska, R.; Rutkowska, W. A.; Augustynski, J.; Cerny, R. J. *Phys. Chem. B* **2005**, *109*, 13685-13692.
13. Kleiman-Shwarsstein, A.; Hu, Y. S.; Forman, A. J.; Stucky, G. D.; McFarland, E. W. *J. Phys. Chem. C* **2008**, *112*, 15900-15907.
14. Hu, Y. S.; Kleiman-Shwarsstein, A.; Forman, A. J.; Hazen, D.; Park, J. N.; McFarland, E. W. *Chem. Mater.* **2008**, *20*, 3803-3805.
15. Kleiman-Shwarsstein, A.; Huda, M. N.; Walsh, A.; Yan, Y.; Stucky, G. D.; Hu, Y.; Al-Jassim, M. M.; McFarland, E. W. *Chem. Mater.* **2010**, *22*, 510–517.
16. Jang, J. S.; Lee, J.; Ye, H.; Fan, F. R. F.; Bard, A. J. *J. Phys. Chem. C* **2009**, *113*, 6719-6724.

17. Hardee, K. L.; Bard, A. J. *J. Electrochem. Soc.* **1976**, *123*, 1024.
18. Miller, E. L.; Rocheleau, R. E.; Khan, S. *Int. J. Hydrogen Energ.* **2004**, *29*, 907 – 914.
19. Woodhouse, M.; Parkinson, B. A. *Chem. Mater.* **2008**, *20*, 2495–2502.
20. Arai, T.; Konishi, Y.; Iwasaki, Y.; Sugihara, H.; Sayama, K. *J. Comb. Chem.* **2007**, *9*, 574-581.
21. Katz, J. J.; Gingrich, T. R.; Santori, E. A.; Lewis, N. S. *Energy Environ. Sci.*, **2009**, *2*, 103–112.
22. Dohnalek, Z.; Kimmel, G. A.; McCready, D. E.; Young, J. S.; Dohnalkova, A.; Smith, R. S.; Kay, B. D. *J. Phys. Chem. B* **2002**, *106*, 3526-3529.
23. Flaherty, D. W.; Dohnalek, Z.; Dohnalkova, A.; Arey, B. W.; McCready, D. E.; Ponnusamy, N.; Mullins, C. B.; Kay, B. D. *J. Phys. Chem. C* **2007**, *111*, 4765-4773.
24. Hawkeye, M.M.; Brett, M. J. *J. Vac. Sci. Technol. A* **2007**, *25*, 1317-1335.
25. Robbie, K.; Brett, M. J. *J. Vac. Sci. Technol. A* **1997**, *15*, 1460-1465.
26. Robbie, K.; Brett, M. J.; Lakhtakia, A. *Nature* **1996**, *384*, 616.
27. Abelmann, L.; Lodder, C. *Thin Solid Films* **1997**, *305*, 1-21.
28. Robbie, K.; Sit, J. C.; Brett, M. J. *J. Vac. Sci. Technol. B* **1998**, *16*, 1115-1122.
29. Flaherty, D. W.; Hahn, N. T.; Ferrer, D.; Engstrom, T. R.; Tanaka, P. L.; Mullins, C. B. *J. Phys. Chem. C* **2009**, *113*, 12742-12752.
30. Flaherty, D. W.; May, R. A.; Berglund, S. P.; Stevenson, K. J.; Mullins, C. B. *Chem. Mater* **2010**, *22*, 319-329.
31. May, R. A.; Flaherty, D. W.; Mullins, C. B.; Stevenson, K. J. *J. Phys. Chem. Lett.* **2010**, *1*, 1264-1268.
32. Suzuki, M.; Ito, T.; and Taga, Y. *Appl. Phys. Lett.* **2001**, *78*, 3968-3970.
33. Wolcott, A.; Smith, W. A.; Kuykendall, T. R.; Zhao, Y. P.; Zhang, J. Z. *Small* **2009**, *5*, 104-111.

34. Kiema, G. K.; Colgan M. J.; Brett M. J. *Sol. Energ. Mat. Sol. Cells* **2005**, *85*, 321-331.
35. Wolcott, A.; Smith, W. A.; Kuykendall, T. R.; Zhao, Y. P.; Zhang, J. Z. *Adv. Funct. Mater.* **2009**, *19*, 1849-1856.
36. Smith, W.; Zhao, Y. P. *Catalysis Communications* **2009**, *10*, 1117–1121.
37. Hahn, N. T.; Ye, H.; Flaherty, D. W.; Bard, A. J.; Mullins, C. B. *ACS Nano* **2010**, *4*, 1977-1986.
38. Anderman, M.; Kennedy, J. H. In *Semiconductor Electrodes*, Finklea, H. O., Ed.; Elsevier: Amsterdam, 1988; Chapter 3.
39. Poxson, D. J.; Mont, F. W.; Schubert, M. F.; Kim, J. K.; Schubert, E. F. *Appl. Phys. Lett.* **2008**, *93*, 101914.
40. Cesar, I.; Sivula, K.; Kay, A.; Zboril, R.; Graetzel, M. *J. Phys. Chem. C* **2009**, *113*, 772-782.
41. Berry, F. J.; Greaves, C.; Helgason, O.; McManus, J.; Palmer, H. M.; Williams, R. T. *J. Solid State Chem.* **2000**, *151*, 157-162.
42. Berry, F. J.; Bohorquez, A.; Moore, E. A. *Solid State Commun.* **1999**, *109*, 207-211.
43. Velev, J.; Bandyopadhyay, A.; Butler, W. H.; Sarker, S. *Phys. Rev. B* **2005**, *71*, 205208.
44. Rao, M. V.; Rajeshwar, K.; Pal Verneker, V. R.; DuBow, J. J. *Phys. Chem.* **1980**, *84*, 1987-1991.
45. NREL AM 1.5 Gobal solar spectrum derived from SMARTS v.2.9.2; <http://rredc.nrel.gov/solar/spectra/am1.5/>

Chapter 4: Electrochemical Synthesis and Characterization of p-CuBi₂O₄ Thin Film Photocathodes

INTRODUCTION

An effective PEC H₂ generation scheme *via* water splitting requires efficient, stable and relatively abundant photoelectrode materials. The lack of a material capable of simultaneously evolving H₂ and O₂ from water with high solar conversion efficiencies (10% or more)¹ has motivated researchers to pursue tandem-cell devices utilizing two separate solar light absorbing materials as photocathode and photoanode.^{2,3,4} Such approaches have demonstrated commercially viable solar-to-hydrogen (STH) efficiencies greater than 10%, if not long-term stability.³ These types of devices require proper matching of the photocurrents (limited by the solar absorption of the material and its quantum yield) and also the photovoltages of the two photoelectrodes for proton reduction and water oxidation.⁵ Although high photocurrents have been attained with some photocathode materials, their low photovoltages make effective pairing with a photoanode material difficult. For example, stable photocurrents from H₂ evolution of at least 8 mA/cm² were achieved using photocathodes consisting of p-Si,⁶ p-CuGaSe₂,⁷ or p-CuInGaSe₂.⁸ However, the maximum cathodic photocurrent onset potentials relative to the reversible hydrogen electrode (RHE) demonstrated for these materials were approximately 0.5, 0.14, and 0.4 V, respectively.⁶⁻⁸ In a tandem-cell such materials place an excessively large demand on the photoanode, which must provide similar photocurrents while simultaneously making up the rest of the 1.23 V (plus overpotential) required for unbiased water splitting. This is especially difficult to achieve since stable

photoanode materials, such as α -Fe₂O₃, typically exhibit poorer electronic properties than photocathode materials, and must also drive the more kinetically challenging water oxidation reaction.

One recently discovered photocathode material of promise is the spinel-type CuBi₂O₄.⁹ This material is claimed to possess a band gap of 1.5 eV and a cathodic photocurrent onset of 1.0 V vs. RHE.¹⁰ However, photo-induced H₂ generation has not been reported and limited PEC characterization has been performed. If high, stable photo-conversion efficiency could be demonstrated, the favorable band edge positions of p-CuBi₂O₄ would make it an effective photocathode in a tandem PEC device for water splitting. We report the synthesis of p-CuBi₂O₄ thin films by electrodepositing a bimetallic film of Cu and Bi followed by oxidation in air at elevated temperatures. A number of materials for solar energy utilization have been deposited by electrodeposition including CuInGaSe₂,¹¹ α -Fe₂O₃,¹² and Cu₂O,¹³ and many other groups have demonstrated a high degree of manipulation of thin film properties using this technique. This method was selected for the formation of CuBi₂O₄ films due to the proximity of the Cu and Bi deposition potentials, which allows for co-deposition from a single bath containing both Cu²⁺ and Bi³⁺ ions.

EXPERIMENTAL METHODS

Film Preparation

Bath solutions for Cu-Bi co-deposition were prepared by dissolving Bi(NO₃)₃·5(H₂O) and Cu(NO₃)₂·3(H₂O) in 10% nitric acid. Nitric acid was required to

dissolve the bismuth nitrate precursor. Deposition was carried out in a three-electrode cell using a Pt wire counter electrode and Ag/AgCl reference electrode. Substrates used for deposition were ultrasonically cleaned and rinsed FTO-coated glass (Hartford Glass) with a typical total deposition area of 1.5 to 2 cm². A CH Instruments CHI832 potentiostat was operated in potentiostatic mode to accomplish the cathodic co-deposition. Pulsed cathodic electrodeposition was accomplished using a CHI660 potentiostat. Following deposition the samples were rinsed with de-mineralized water and dried in an air stream. Annealing was performed in air at various temperatures to oxidize and crystallize the films using the desired temperature and duration in a muffle furnace (Ney). A heating rate of 10°C/min was employed, and the samples were allowed to cool naturally.

Film Characterization

Scanning electron microscopy (SEM) and energy dispersive X-ray spectroscopy (EDS) were performed using a Quanta FEG 650 electron microscope (FEI). X-ray diffraction (XRD) experiments utilized a Bruker D8 diffractometer. Mean grain size was calculated using the Scherrer equation:

$$D = \frac{0.9\lambda}{\beta \cos \theta} \quad (1)$$

Here D is the mean crystallite size, λ is the X-ray wavelength employed (0.154 nm), β is the full-width at half-max of the diffraction peak of interest at scattering angle θ . X-ray photoelectron spectroscopy (XPS) was performed using a Kratos AXIS X-ray photoelectron spectrometer. UV-vis-NIR direct transmittance measurements were made

with a Cary 5000 UV-vis-NIR spectrophotometer, using a bare substrate as a baseline and measuring the directly transmitted beam. Total transmittance and diffuse reflectance spectra were measured with a Cary 500 UV-vis-NIR spectrophotometer attached to a Labsphere DRA-CA-5500 integrating sphere. For total transmittance experiments samples were mounted on the entrance port of the integrating sphere, and the total transmitted light (direct + diffuse) was measured. For transmittance + reflectance (transflectance) experiments samples were suspended in the center of the integrating sphere using a clip-style center mount, and both the transmitted and reflected light were collected simultaneously. In the latter case, the absorptance (A) is given by:

$$A = 100\% - (T + R) \quad (2)$$

Here, A is the percentage of incident light absorbed by the sample and the quantity ($T + R$) is the measured transflectance of the sample suspended in the integrating sphere.

Electrochemical Testing

The electrochemical and PEC properties of each sample were tested using a 3-electrode electrochemical cell with a Ag/AgCl reference electrode and Pt wire counter electrode. All potentials are given relative to Ag/AgCl unless otherwise stated. The working electrode (the photocathode consisting of the CuBi₂O₄ film) with illuminated area 0.21 cm² was immersed in 0.1M Na₂SO₄ (the pH of which was adjusted by adding either KOH or H₂SO₄) or in a phosphate buffer solution (pH 6.7) and illuminated by a 100 W xenon lamp (Newport) through a UV/IR filter (Schott, KG3) with a measured overall power density at the sample surface of 73 mW/cm² as measured by a thermopile

(Newport). A 420 nm cut-on filter was employed at times to remove any remaining UV photons. During linear sweep voltammograms (LSV's) a scan rate of 25 mV/s was used. A monochromator (Newport) was employed to study spectral response and was used in conjunction with a monochromatic power meter and photodiode (Newport) to calculate the IPCE, given by:

$$IPCE = \frac{j_{ph}}{I} \times 100\% \quad (3)$$

Here j_{ph} is the steady state photocurrent density and I is the photon flux at the film surface for the wavelength of interest. Absorbed photon-to-current efficiencies (APCE) were calculated by dividing the IPCE by the absorbance of the film from eq. 2 at each wavelength of interest. A potentiostat (CH Instruments – CHI660) was operated by a desktop computer to perform electrochemical measurements.

RESULTS AND DISCUSSION

Deposition potential effects

Films of Cu and Bi were deposited from nitric acid baths containing 4 mM $\text{Cu}(\text{NO}_3)_2$ and 8 mM $\text{Bi}(\text{NO}_3)_3$ at potentials ranging from -0.3 V to -0.8 V vs Ag/AgCl. Most films appeared dark-grey to black, depending on thickness, although films deposited at more negative potentials showed a copper-like color. The deposition time was decreased when more negative potentials were employed in order to deposit similar amounts of metal in each case. SEM and EDS were used to investigate how the deposition potential affected the morphology and composition of the films. SEM images

revealed that the films consist of clusters of particles that are about 100 nm in diameter. Variations in film morphology were observed as the deposition potential was changed, with a general trend toward smaller particles and higher nucleation density at the more negative potentials (Figure 4.1). EDS analyses indicated that the Cu content of the films increases as deposition potential becomes more negative (Figure 4.2). The general trend in composition appears to indicate that films near the desired Bi:Cu ratio of 2:1 are deposited at potentials between -0.4 and -0.6 V vs Ag/AgCl so a potential of -0.5 V was selected to deposit subsequent films.

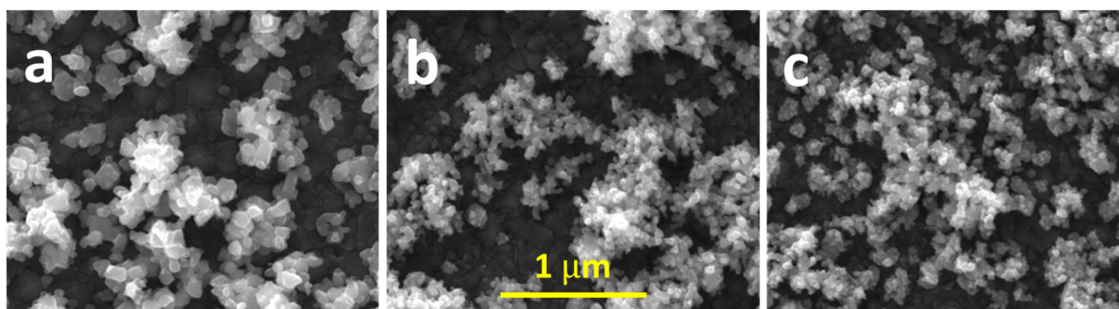


Figure 4.1. Electrodeposited films of Cu-Bi deposited at a) -0.3 V, b) -0.5 V, or c) -0.7 V vs Ag/AgCl from a nitric acid bath. The scale bar applies to all images.

Bi and Cu electrodeposition onto conductive oxide substrates such as FTO typically proceeds *via* instantaneous nucleation and three-dimensional growth, yielding films with poor surface coverage.^{14,15} The sequence of Bi deposition onto FTO films has been described as: cluster formation after double-layer discharge, critical nuclei formation, coalescence of nuclei, and diffusion controlled growth.¹⁶ Deposition from Bi-rich baths led to films with more particle clustering and lower nucleation density at the same deposition potentials. Bi appears to be the main contributor to the poor surface

coverage of mixed metal particle clusters. Deposition from a bath containing only $\text{Bi}(\text{NO}_3)_3$ resulted in branched Bi nanowires across the substrate, as has been reported by others.¹⁴

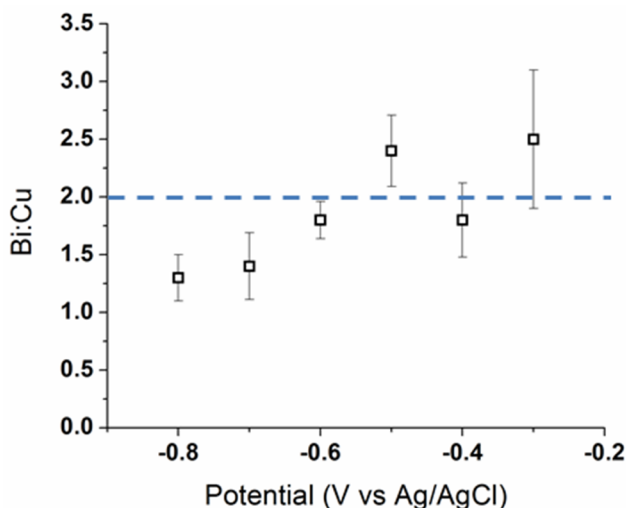


Figure 4.2. EDS analysis results for the ratio of Bi to Cu in the Cu-Bi films deposited at various potentials vs Ag/AgCl. The desired Bi:Cu ratio is indicated by the horizontal dashed line. The error bars represent the standard deviation of the five EDS spot analyses taken on each film.

Annealing temperature effects

In order to form the desired CuBi_2O_4 phase, films deposited at -0.5 V were annealed in air at temperatures ranging from 350 to 600°C. XRD was used to investigate the dependence of crystal structure on annealing temperature (Figure 4.3). Prior to annealing only crystalline Bi (PDF# 01-071-4642) and SnO_2 (PDF# 01-070-6153) are observed. When a bath containing only Cu was employed a faint peak suggestive of crystalline Cu was observed in the XRD pattern of the deposited film, but films deposited from a mixed bath did not show this feature, and the Bi peak positions were not shifted

from their expected values, presumably indicating that the Cu in these films remains amorphous rather than crystallizing to any great extent or forming a solid solution with Bi. Annealing the bimetallic films at 350°C for 2 h resulted in crystallization, and a number of bismuth oxide phases appeared. At 450°C, peaks belonging to the kusachiite CuBi_2O_4 phase (PDF # 00-042-0334) developed and by 600°C only kusachiite and SnO_2 peaks from the FTO substrate remained. All CuBi_2O_4 films show preferred (211) orientation, as observed for CuBi_2O_4 materials prepared by other methods.^{9,17} The present annealing conditions for the co-deposited Cu-Bi films are much less demanding than those required for the solid state reaction of CuO and Bi_2O_3 (700°C, 24-25 h).^{10,17} In addition to becoming more phase pure, the films demonstrate greater crystallinity at higher temperatures, as indicated by both an increase in CuBi_2O_4 peak height relative to SnO_2 and an increase in the average CuBi_2O_4 (211) grain size, calculated *via* the Scherrer equation from 19 nm at 450°C to 21 nm at 550°C and 24 nm at 600°C. Further annealing the 600°C samples for another 2 hours increased the intensity of all CuBi_2O_4 peaks relative to those of the substrate, but did not appear to increase the (211) grain size. Increased annealing temperature led to larger, smoother particles that appeared to be better interconnected (Figure 4.3). Preliminary PEC testing in pH 6 electrolyte (0.1M Na_2SO_4) showed higher and more consistent photocurrents at -0.2 V vs Ag/AgCl (the onset potential of large dark current) for films annealed at 600°C compared to those annealed at lower temperatures (see Appendix C, Figure C.1). These photocurrents, below $50 \mu\text{A}/\text{cm}^2$, are quite low for a material capable of absorbing through the entire visible range, revealing that the photo-conversion efficiency must be very poor for these

films. However, they lie in the same range as those observed by others for films deposited by metal-organic decomposition (MOD), although only currents were reported rather than current densities.^{9,10} It is quite possible that p-CuBi₂O₄ inherently contains a large number of defect states acting as recombination centers.

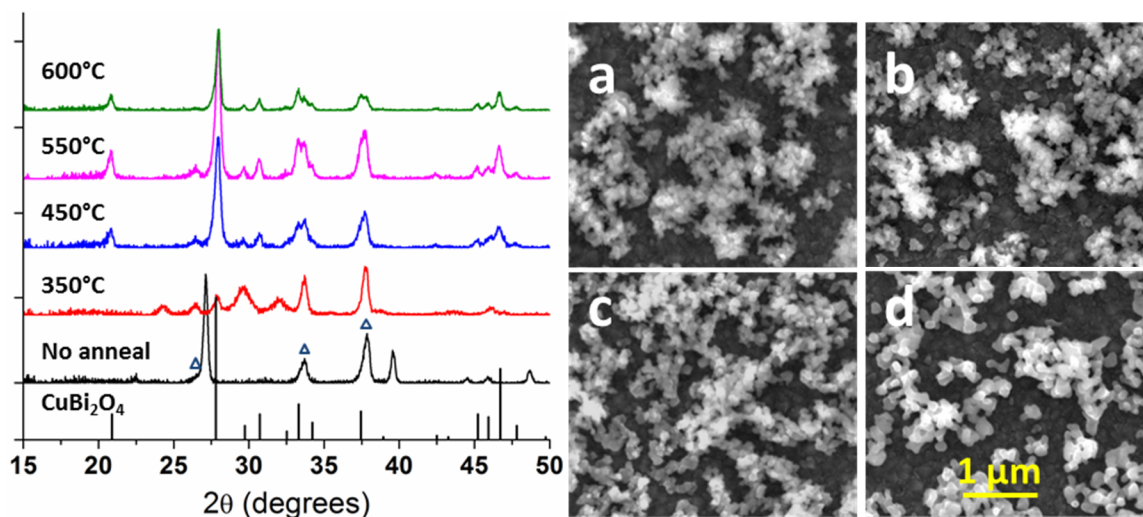


Figure 4.3. Left: XRD patterns for films deposited at -0.5 V vs Ag/AgCl and annealed to various temperatures. A standard kusachiite line pattern (PDF # 00-042-0334) is also displayed. Observable SnO₂ peak positions are indicated by Δ. Right: SEM images of CuBi₂O₄ particulate films deposited at -0.5 V for 2 min with overall cation concentration of 12 mM. These samples were then annealed to a) 350°C, b) 450°C, c) 550°C or d) 600°C for 2 h in air. The scale bar applies to all images.

Bath concentration effects

Another possible hindrance to the photo-conversion efficiency of the present films for water reduction could be their poor coverage of the FTO substrates. Therefore, the PEC performance may be improved by increasing the nucleation density of Cu-Bi clusters and improving the contact between the particles and the substrate. Various bath cation concentrations ranging from 24 mM (8 mM Cu²⁺, 16 mM Bi³⁺) down to 1.2 mM

(0.4 mM Cu^{2+} , 0.8 mM Bi^{3+}) were employed in an effort to study their effects on film morphology. In each case the deposition potential was maintained at -0.5 V. Due to the differences in deposition rate among the various bath concentrations, the deposition time was adjusted in each case to result in a similar amount of deposited material. SEM images reveal that the nucleation density and surface coverage could be manipulated to a large extent by altering the bath concentration, with lower concentrations yielding improved coverage and somewhat smaller particles, even after annealing (Figure 4.4). However, only a minor influence on PEC performance was observed.

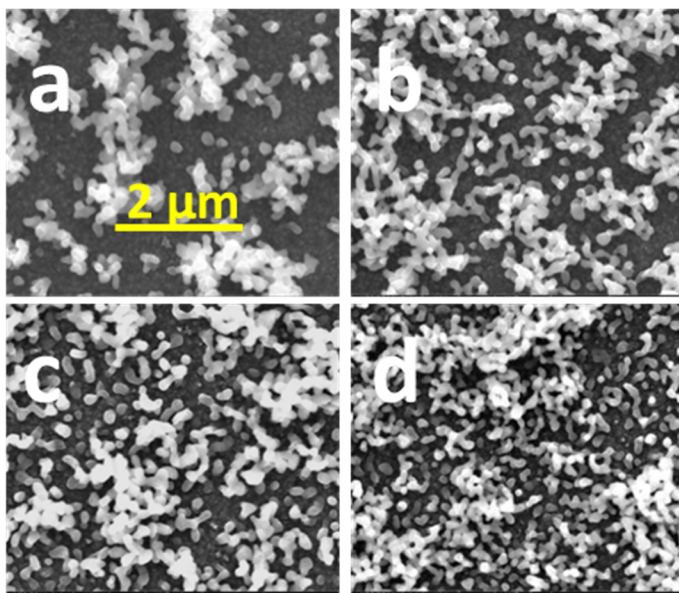


Figure 4.4. SEM images of CuBi_2O_4 particulate films deposited -0.5 V with varying overall cation concentrations: a) 24 mM, b) 6 mM, c) 3 mM or d) 1.2 mM. Approximately the same amount of CuBi_2O_4 was deposited in each case and all samples were annealed to 600°C for 2 h in air. The scale bar applies to all images.

Film thickness effects

In an attempt to study the effects of deposition time and thus, film thickness, films were deposited at -0.5 V for times ranging from 2 to 8 min from a bath concentration of 6 mM and annealed at 600°C (Figure 4.5). At 2 min the films consist of a relatively uniform layer of particles (1 to 3 particles thick) with a surface coverage of approximately 50%. At longer times the surface coverage does not increase, but appears to decrease slightly due to particle coalescence. Apparently, new particles are added on top of existing ones rather than attaching directly to the substrate. From the various SEM images, it would appear that for the CuBi_2O_4 films deposited for longer than 2 min, relatively few particles are actually in close contact with the FTO substrate. PEC performance did not show clear correlation with deposition time over the range investigated, likely due to the fact that increased light absorption was balanced by decreased hole collection efficiency. One would expect that holes photo-generated near the top of a thick film can only reach the substrate by traversing numerous grain and particle boundaries where recombination is likely. In films deposited for 2 min or less, this would appear to be less of an issue as most of the particles in these films seem to be adjacent to or within one or two particle layers of the substrate. However, the physical interaction of the particles with the substrate may not be particularly strong, as indicated by the relative ease with which the films can be wiped off by dragging a tissue across the surface. This poor contact at the film-substrate interface and resulting poor electron transfer is another likely source of recombination in all films, regardless of thickness.

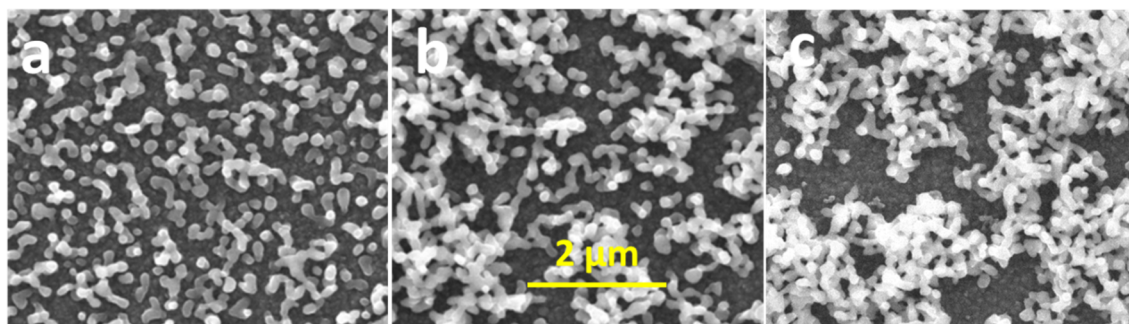


Figure 4.5. SEM images of CuBi_2O_4 films deposited at -0.5 V from a bath cation concentration of 6 mM for a) 2 min, b) 4 min, and c) 8 min, and annealed at 600°C for 2 h.

Optical properties

Interestingly, all films appeared light brown after annealing unlike CuBi_2O_4 powder formed in our lab by the solid state reaction of Cu_2O and Bi_2O_3 at 700°C for 24 h, which was black. However, when placed in front of a white light source so that only transmitted light was viewed, the films had a dark reddish grey color. A likely explanation is that light scattering from the particle clusters plays a significant role in the optical properties of these films, leading to the lighter color when reflected light is viewed. The UV-vis-NIR absorbance spectra, taken in transmittance and transflectance mode, respectively, for films deposited for 5 min from a 6 mM bath and annealed to 600°C are shown in figure 4.6. The films show a noticeable absorption threshold at 680 nm (1.8 eV) and weak, featureless absorption at longer wavelengths. The absorbance of the FTO substrate appears to contribute to a majority of the observed NIR absorbance of the film. The light-brown color of the films appears to be due to the reflected light in the 500 to 700 nm range. When only directly transmitted light was measured the absorbance gradually increased starting from wavelengths longer than 1200 nm, peaked near 600 nm

and decreased at shorter wavelengths (see Appendix C, Figure C.2). Tauc analyses of these plots tended to yield estimated direct band gaps of 1.4 - 1.5 eV, which agree with early reports.^{9,17} However, it is clear that diffusely reflecting and transmitting light must be taken into account in order to obtain an accurate view of the light absorbing properties of films that exhibit significant light scattering. When these are taken into account the observed band gap appears to be 1.8 eV. Although the estimated band gap is promising, the overall absorbance in the UV-vis range is somewhat weak, which is due to the incomplete coverage of the substrate by the CuBi_2O_4 film and significant reflectance by the particles in the film.

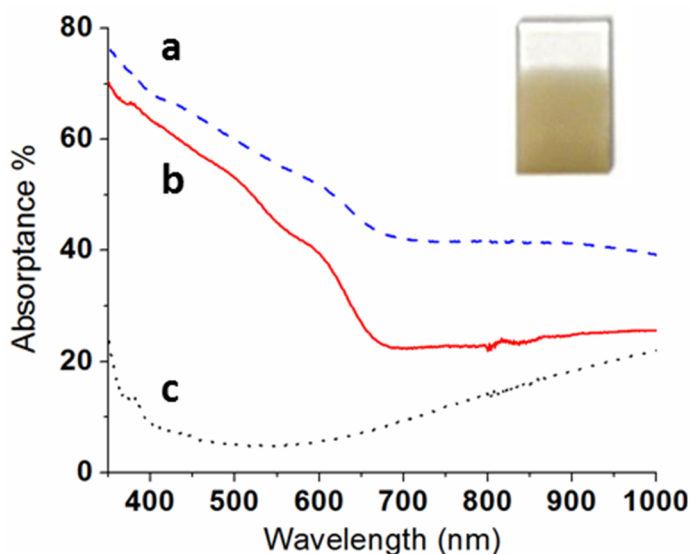


Figure 4.6. UV-vis-NIR absorbance spectra calculated using a) total transmittance (direct + diffuse) of a film on FTO, b) transmittance + reflectance of a film on FTO, and c) transmittance + reflectance of an FTO substrate only. The films were deposited at -0.5 V for 5 min from a bath concentration of 6 mM. A photograph of the film is shown at top-right.

PEC behavior

The PEC performance of films deposited from a 6 mM bath cation concentration for 5 min was tested in neutral (phosphate buffer: pH 6.7), acidic (pH 3.5), and basic (pH 10.8) electrolytes. Photocurrents were similar in each electrolyte when the potential ranges were corrected for a Nernstian shift with pH. However, testing in basic electrolyte tended to result in slightly more positive photocurrent and dark current onset potentials. A cathodic photocurrent onset potential between 1.05 and 1.1 V *vs* RHE was determined at pH 10.8, which is similar to that observed in a previous study in pH 5.8 electrolyte (Figure 4.7).¹⁰ At pH 10.8 significant dark currents were observed at potentials below 0.6 V *vs*. RHE and could originate from a number of processes such as reduction of the p-CuBi₂O₄ film or of the exposed FTO substrate or possibly the reduction of cathodically unstable impurity phases in the film undetected by XRD, such as Cu_xO or Bi_xO_y. A previous study on p-CuBi₂O₄ that showed similar dark current behavior also demonstrated a turnover number of over 13 for long-term illumination, indicating satisfactory PEC stability despite this dark reduction current.⁹ To assess the PEC stability of our films over time, constant potential tests were performed at the dark current onset potential (-0.2 V for pH 10.8 and 0.0 V for pH 3.5) under full-spectrum illumination for over 1 h (Figure 4.8). The performance in acid and basic electrolyte differed remarkably. Although both films showed a large initial drop in photocurrent, the photocurrent stabilized at a steady-state value of 33 $\mu\text{A}/\text{cm}^2$ in basic electrolyte. However, in acidic electrolyte the photocurrent continued to decay throughout the experimental time window, dropping to 5 $\mu\text{A}/\text{cm}^2$ after 1 h. Examination of the films confirmed a slightly

darkened color for those films tested in both electrolytes over long times, although the color change was more pronounced for the acidic electrolyte.

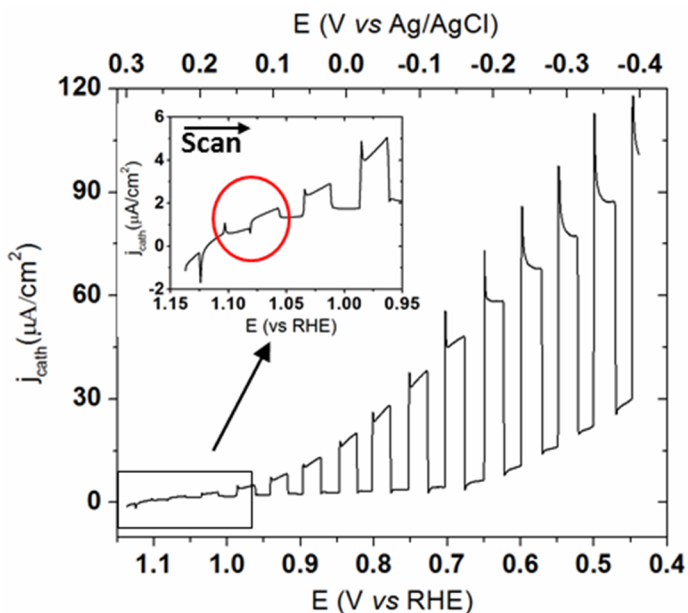


Figure 4.7. Photoelectrochemical response under “chopped” Xe-lamp illumination of a typical film deposited at -0.5 V for 5 min. The inset indicates the switch from anodic to cathodic photocurrent between 1.05 and 1.1 V vs. RHE. The electrolyte is N_2 degassed aqueous Na_2SO_4 (adjusted to pH 10.8), and the scan rate is 25 mV/s.

The photo-cathodic instability of metal oxides such as Cu_xO is typically due to the preferential reduction of metal cations such as Cu^{2+} or Cu^+ to Cu rather than the reduction of protons to H_2 .¹⁹ If this were the case for $CuBi_2O_4$, one would expect the surface Cu^{2+} or Bi^{3+} species of the particles to be reduced after testing. Films subjected to 1.5 h of steady state photocurrent passage in each electrolyte (pH 3.5 and pH 10.8) were studied by XPS to elucidate any surface chemical/compositional differences between the films before and after testing. Prior to testing, the XPS spectra for Cu and Bi showed peaks indicative of Cu^{2+} and Bi^{3+} as expected (see Appendix C, Figure C.3).^{20,21} Although the

Bi 4f spectra remained largely unchanged, clear differences between the films could be discerned in the Cu 2p spectra (Figure 4.8). Both films showed a strong Cu²⁺ peak at 933.8 eV prior to testing and the addition of a reduced Cu⁺ (or Cu) peak at 932.4 eV after. However, for the acid-tested film the Cu²⁺ peak essentially disappeared after testing and the Cu 2p peak intensities were diminished overall indicating that the acidic environment promoted the dissolution of Cu. After prolonged testing the films showed surface Cu:Bi ratios of 0.16 and 0.43 for acid and base, respectively.

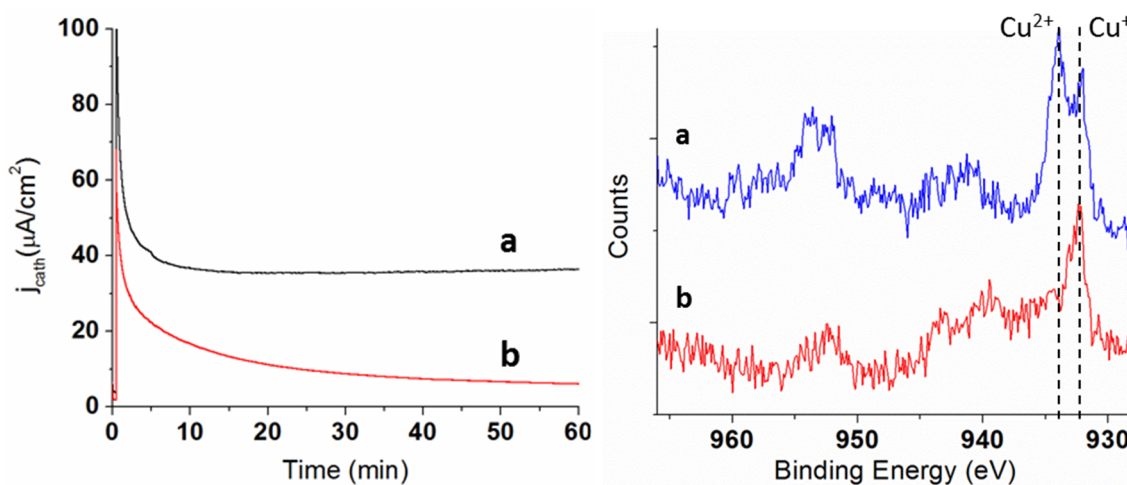


Figure 4.8. Left: One hour photocurrent vs. time plots for CuBi₂O₄ films held at constant potentials in pH 10.8 (a) or 3.5 (b) in 0.1M Na₂SO₄ solutions under full spectrum Xe-lamp illumination. Right: XPS Cu 2p spectra for CuBi₂O₄ films after more than one hour of constant photocurrent passage in either pH 10.8 (a) or pH 3.5 (b) aqueous Na₂SO₄ electrolyte. The Cu 2p_{3/2} peak positions for Cu⁺ and Cu²⁺ at 932.4 and 933.8 eV are indicated by the dashed lines.

These results are consistent with the photocurrent vs. time behavior, which showed a continuous reduction in activity for the acid-tested film but only transient reduction leading to eventually steady photo-activity for the base-tested film. In base, the

CuBi₂O₄ films appear to suffer from photocathodic corrosion for a brief period, but eventually reach a passivated state after which further photocorrosion either does not occur or only occurs very slowly. In acid, the films do not appear to reach this passivated state. In basic electrolyte the fact that this steady-state photocurrent proceeds indefinitely while the electrolyte is continuously bubbled with N₂ indicates that the photo-current is most likely from the reduction of protons or water to form H₂, although at quite low rates.

Photo-conversion efficiency

The IPCE spectra of films deposited at -0.5 V for 5 min from a bath concentration of 6 mM were recorded in pH 10.8 electrolyte after extensive steady-state photocurrent passage in order to assess their stable PEC performance as a function of wavelength of incident light for both front and backside illumination (Figure 4.9). Quantum yields of only ~1-2% were achieved with UV-irradiation, and these decreased throughout the visible range, becoming negligible between 660 and 700 nm. This photocurrent onset wavelength corresponds to a photon energy of about 1.8 eV, in good agreement with the optical absorption threshold observed when total transmittance and reflectance were accounted for. This apparent band gap value is somewhat larger than the reported band gap of 1.4 to 1.5 eV, although as noted previously, only one optical absorption spectrum has ever been published for CuBi₂O₄.¹⁸ When the IPCE values were integrated over the standard AM1.5G spectrum,²² whole spectrum photocurrents of 44 and 55 $\mu\text{A}/\text{cm}^2$ for front and backside illumination, respectively, were calculated for these conditions (0.64 V vs RHE). Visible light (wavelengths of 420 nm and above) contributed 66% and 61%

of these photocurrent values, respectively, which is very consistent with the change in photocurrent observed when the Xe lamp was blocked by a 420 nm cut-on filter. These calculated photocurrents are much lower than what one would expect from a material with a band gap of 1.8 eV, but are consistent with the fact that the full-spectrum steady-state photocurrents measured for these films at this potential were generally in the 25 to 35 $\mu\text{A}/\text{cm}^2$ range when illuminated by a Xe lamp with a light intensity of nearly 0.75 suns. Prior to long-term steady-state photocurrent passage, IPCE's were nearly three times higher, resulting in integrated front-side illumination photocurrents of 110 – 120 $\mu\text{A}/\text{cm}^2$ (see Appendix C, Figure C.4). This larger initial photocurrent could be due to the presence of reducible impurities on the surfaces of the films as well as the initial reduction of the films themselves.

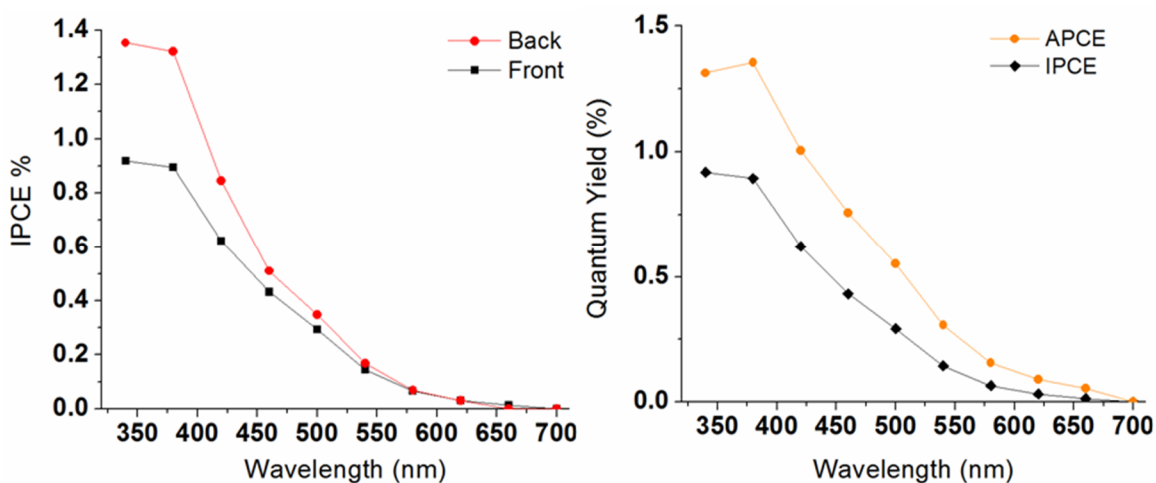


Figure 4.9. Left: IPCE plots for front and backside illumination of a typical CuBi_2O_4 film held at -0.2 V vs Ag/AgCl in pH 10.8 Na_2SO_4 after 1 h steady photocurrent passage. Right: Comparison of IPCE and APCE for a typical film after 1 h steady photocurrent passage at -0.2 V vs Ag/AgCl in pH 10.8 Na_2SO_4 .

The reasons for the poor photo-conversion efficiency of these electrodes may be manifold. To study the effects of poor light absorption in the visible range, absorbed photon-to-current conversion efficiencies (APCE), also known as internal quantum yields, were calculated by dividing the IPCE values by the absorptance of the films at the same wavelengths (Figure 4.9). The absorptance spectrum of the film shown in figure 4.9b was employed as a first order approximation – APCE values will be slightly underestimated due to absorption by the FTO. Although this spectrum showed a less dramatic decrease in the visible range than the IPCE spectrum, the internal quantum yield of the film was still quite low. As discussed earlier the particulate morphology may not be ideal for high photo-conversion efficiency due to the difficulty of transporting photo-generated holes to the substrate across particle boundaries. For example, when the films were illuminated from the backside the quantum yields improved by 50% in the UV-range, indicating that holes were more efficiently collected when they were generated in the underside rather than in the top layer of the particulate film. This illustrates that majority carrier transport is hindered in these films, as has been observed for other metal oxide films such as α -Fe₂O₃ and BiVO₄.^{23,24,25,26} Also, the poor mechanical adhesion of the films to the substrate indicates that the particles were only weakly attached to the FTO, which may play a role in hindering hole transfer from the film to the substrate.

The presence of native defects in the CuBi₂O₄ material on the surface or in the bulk could greatly increase recombination rates. Previous studies on CuBi₂O₄ films prepared by metal-organic decomposition^{9,10} also showed low photocurrents in the μ A

range, revealing that CuBi_2O_4 may possess inherently poor electronic properties due to such defects. The optical absorbance spectra indicate that a significant amount of light absorption occurs for wavelengths far greater than the photocurrent onset threshold of 680 nm (and even beyond 1000 nm). This absorption could be a result of a large number of trap states within the mid-gap of CuBi_2O_4 , either on the surface or in the bulk.²⁷ A common test to probe for the effects of surface traps lying within the band gap is the addition of species to the electrolyte that are thermodynamically easier to either reduce or oxidize depending on whether cathodic or anodic behavior is being studied.²⁸ In this case molecules with more positive reduction potentials could be reduced by electrons trapped in surface states below the conduction band edge. Attempts to probe this behavior by the addition of formaldehyde ($E^0 = 0.23 \text{ V vs. RHE}$) or methanol ($E^0 = 0.59 \text{ V vs. RHE}$) to the electrolyte showed almost no effect, revealing that surface mid-gap trap states may not be the rate-limiting factor for the conversion efficiency of these films. Non-stoichiometric regions of the nominally CuBi_2O_4 particles or small domains of binary oxide phases of Cu_xO or Bi_xO_y could instead be responsible for higher recombination rates.

Several attempts were made to improve the morphology of the films through the addition of common Bi^{3+} chelating agents such as triethylamine (TEA) or EDTA or by employing pulsed electrodeposition techniques to increase nucleation density. Chelating agents such as EDTA and TEA are sometimes employed to improve the uniformity of electrodeposited films of Bi on conductive oxide substrates.^{14,16} However, in the present work the addition of EDTA or TEA in various amounts did not significantly improve the

nucleation density or the photocurrent. Although these additives are known to have a positive effect on Bi deposition, these effects may be mitigated in the current experiments in which Cu and Bi are deposited simultaneously. Another technique commonly employed to increase nucleation density is pulsed electrodeposition (PED). This technique calls for short deposition periods separated by quiescent periods, which are needed to avoid diffusion limitations that can become significant as the solution near the electrode becomes depleted of metal cations.²⁹ Various pulse times (with equivalent rest times) ranging from 0.25 to 10 s were investigated with total deposition times of 1 or 2 min, but significant improvements in neither the surface coverage nor photocurrent were observed. It may be reasonable to conclude that the mild potential of -0.5 V vs Ag/AgCl fixed in this work for Cu and Bi co-deposition did not generate large enough deposition current densities relative to precursor concentration for PED to have a noticeable effect. Typical steady-state deposition current densities observed were only on the order of 1 mA/cm².

Since in general the nucleation density of electrodeposited films increases as the overpotential increases (is made more negative in this case), attempts were made to deposit films at more negative potentials than -0.5 V using a higher ratio of Bi:Cu in the bath in order to maintain the correct stoichiometry of the deposit, which varies with potential. SEM images of films deposited from a bath of 3:1 Bi:Cu at -0.7 and -0.9 V did not reveal significant improvement in film coverage or uniformity (see Appendix C, Figure C.5) and no improvements in PEC performance were observed. Increasing the ratio of Bi:Cu in the bath did succeed in achieving a 2.1:1 ratio in the film at -0.9 V,

however. These as well as preliminary experiments appear to indicate that the composition of the depositing films has a strong effect on the deposition coverage and uniformity with more Bi-rich films exhibiting poorer such characteristics.

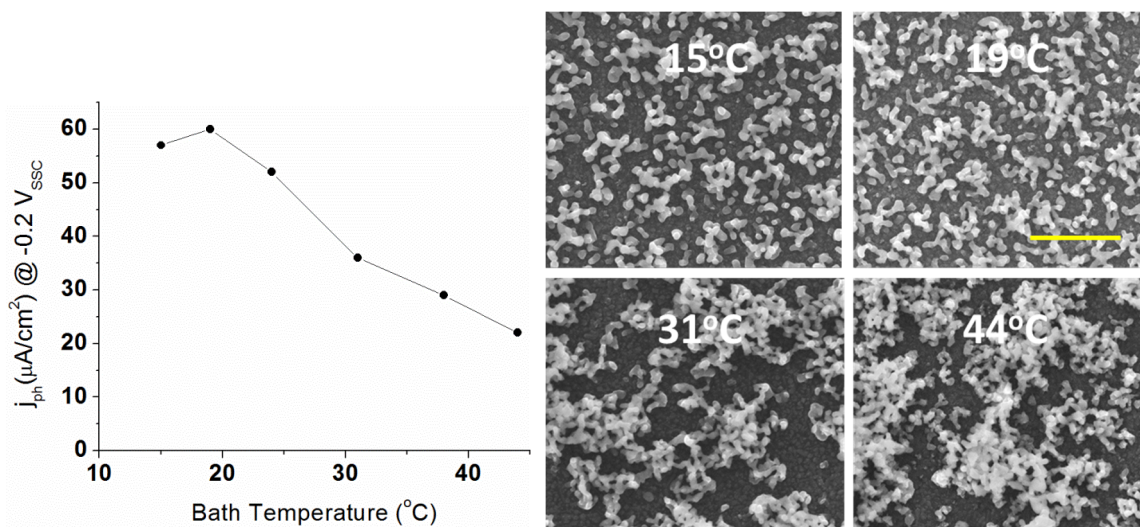


Figure 4.10. Left: Measured photocurrents during LSV scans (25 mV/s) at -0.2 V *vs.* Ag/AgCl in N₂ bubbled 0.1M Na₂SO₄ (pH 10.8) for various deposition bath temperatures. Right: SEM images of CuBi₂O₄ films deposited from baths at different temperatures at -0.5 V *vs.* Ag/AgCl for 5 min. with a cation concentration of 6 mM. The scale bar is 2 μm and applies to all images.

The effects of changing the deposition bath temperature between 15 and 45°C on the film coverage and PEC performance were also explored. Temperatures greater than room temperature resulted in worse coverage and lower photocurrent, but lower temperatures resulted in a slight improvement in both characteristics. The measured photocurrents of these films at -0.2 V *vs.* Ag/AgCl and representative SEM images can be found in figure 4.10. Overall, the most successful means of achieving improved film coverage and uniformity was reducing the concentration of cations in the deposition bath, although improvements in PEC performance were limited.

Ballistically deposited CuBi_2O_4 films

Since a likely reason for the poor PEC performance of electrodeposited CuBi_2O_4 films is their poor coverage and uniformity, a second film deposition method capable of depositing much more uniform films was employed for the sake of comparison. Films of Cu and Bi having the desired 1:2 ratio were deposited by co-evaporation at normal incidence and annealed at 600°C for two hours in air. Large polycrystalline grains were observed by SEM both before and after annealing, and the films exhibited low porosity as expected (Figure 4.11). Film thicknesses were between 200 and 300 nm after annealing, and XRD confirmed that the films were well crystallized as CuBi_2O_4 .

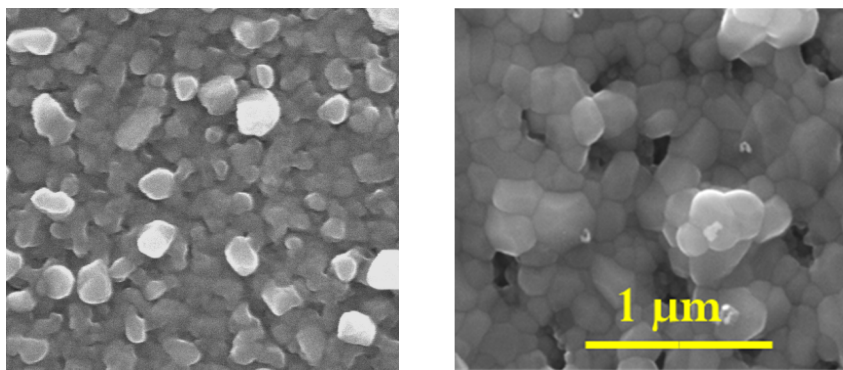


Figure 4.11. SEM images of a film synthesized using ballistic deposition. Left: before annealing. Right: after annealing at 600°C . The scale bar applies to both images.

The PEC performance of these ballistically deposited films was significantly better than those deposited by electrodeposition, often possessing higher photocurrents over the entire range of potentials tested. The j - E behavior was more ideal for the dense films in that the photocurrent rose quickly at relatively anodic potentials, indicating more efficient separation and extraction of electrons and holes under conditions of mild band bending (Figure 4.12). These films also exhibited lower dark currents due to their

improved coverage of the FTO substrates. When the IPCE spectra of films deposited by the two methods were compared, clear qualitative and quantitative differences in behavior were observed. Most noticeably, the UV-activity of the dense, ballistically deposited films greatly exceeded that of the electrodeposited films, despite the fact that their long wavelength (> 550 nm) response was essentially identical (Figure 4.12). The relatively high UV-efficiency of the dense films likely resulted from more efficient transport of holes to the substrate combined with the short transport distance of UV-generated electrons to the electrolyte interface. However, conduction band electrons generated by longer wavelength photons (which were absorbed farther from the electrolyte interface) were not efficiently transported to the electrolyte, leading to comparable performance to the electrodeposited films. These results suggest that ballistically deposited, dense CuBi_2O_4 films are more limited by electron transport to the electrolyte, whereas particulate CuBi_2O_4 films are more limited by hole transport to the substrate.

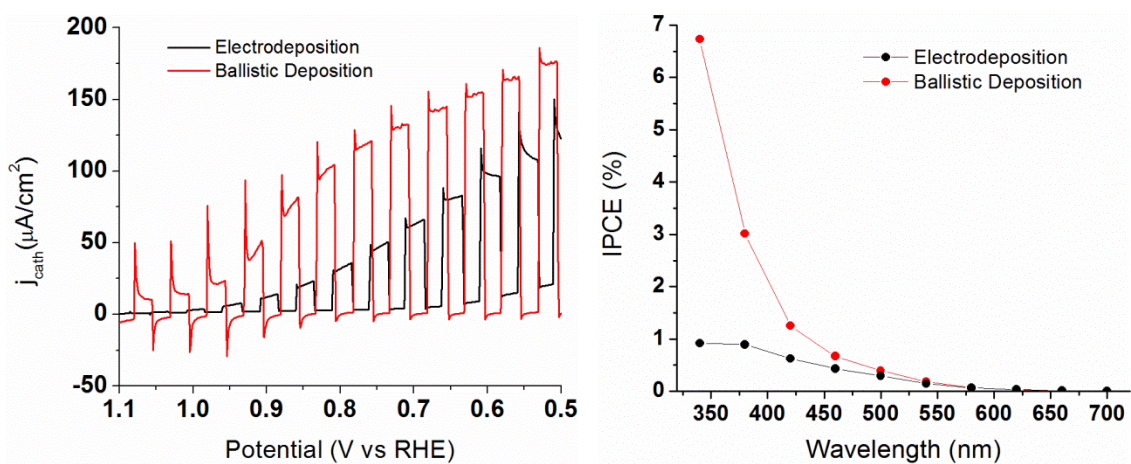


Figure 4.12. Comparison of the PEC performance CuBi_2O_4 films in N_2 bubbled aqueous Na_2SO_4 (pH 10.8). Left: LSV behavior under chopped illumination. Right: IPCE spectra taken at 0.64 V vs. RHE.

CONCLUSIONS

CuBi₂O₄ photocathodes were successfully synthesized by the electrodeposition of particles containing both Cu and Bi followed by their oxidation and crystallization at 600°C in air. The particulate films possessed a light brown color when viewed normally, and optical and PEC tests indicated that the films absorb light throughout the visible range with both an absorption and photocurrent onset threshold near 680 nm. This appears to reveal that the true band gap of CuBi₂O₄ relevant for PEC applications is 1.8 eV. Based on PEC testing, a flat-band potential of 1.05 V vs. RHE is estimated from the onset of cathodic photocurrent in pH 10.8 electrolyte, indicating that the band edge positions of CuBi₂O₄ are quite suitable for generating H₂ from water, provided a moderate bias could be supplied by a photo-anode in a tandem configuration. Although the photocurrent decayed significantly upon initial illumination, stable values of 25 to 35 μA/cm² were achieved after several minutes and persisted for more than 1 h. These low photocurrents were consistent with the measured IPCE spectra, which possessed maxima in the UV-range of 1 - 2% and decreased throughout the visible range, reaching 0.0% at 700 nm. Calculated AM1.5G photocurrents for a typical film were 44 and 55 μA/cm² for front and backside illumination, respectively. Dense films deposited by evaporation showed better performance due to the improved transport of holes to the substrate. Clearly, significant improvements in the electronic properties of p-CuBi₂O₄ thin films *via* improved thin film synthesis techniques and/or doping are required in order to make it a viable photo-cathode material for PEC H₂ generation from water.

REFERENCES

1. Bard, A. J.; Fox, M. A. *Accounts Chem. Res.* 1995, 28, 141-145.
2. Nozik, A. J.; *Appl. Phys. Lett.* 1977, 30, 567-569.
3. Khaselev, O.; Turner, J. A. *Science* 1998, 280, 425-427.
4. Miller, E. L.; Paluselli, D.; Marsen, B.; Rocheleau, R. E. *Sol. Energ. Mat. Sol. Cells* 2005, 88, 131-144.
5. Weber, F. W.; Dignam, M. J. *J. Electrochem. Soc.* 1984, 131, 1258-1265.
6. Boettcher, S. W.; Warren, E. L.; Putnam, M. C.; Santori, E. A.; Turner-Evans, D.; Kelzenberg, M. D.; Walter, M. G.; McKone, J. R.; Brunschwig, B. S.; Atwater, H. A.; Lewis, N. S. *J. Am. Chem. Soc.* 2011, 133, 1216-1219.
7. Marsen, B.; Cole, B.; Miller, E. L. *Sol. Energ. Mat. Sol. Cells* 2008, 92, 1054-1058.
8. Yokoyama, D.; Minegishi, T.; Maeda, K.; Katayama, M.; Kubota, J.; Yamada, A.; Konagai, M.; Domen, K. *Electrochem. Comm.* 2010, 12, 851-853.
9. Arai, T.; Konishi, Y.; Iwasaki, Y.; Sugihara, H.; Sayama, K. *J. Comb. Chem.* 2007, 9, 574-581.
10. Arai, T.; Konishi, Y.; Iwasaki, Y.; Sugihara, H.; Sayama, K. *J. Phys. Chem. C Lett.* 2007, 111, 7574-7577.
11. Kwak, W.C.; Han, S.H.; Kim, T. G.; Sung, Y.M. *Cryst. Growth Des.* 2010, 10, 5297-5301.
12. Kleiman-Shwarsctein, A.; Huda, M. N.; Walsh, A.; Yan, Y.; Stucky, G. D.; Hu, Y.; Al-Jassim, M. M.; McFarland, E. W. *Chem. Mater.* 2010, 22, 510-517.
13. McShane, C. M.; Choi, K.S.; *J. Am. Chem. Soc.* 2009, 131, 2561-2569.
14. Jiang, S.; Huang, Y.H.; Luo, F.; Du, N.; Yan, C.H. *Inorg. Chem. Commun.* 2003, 6, 781-785.
15. Khelladi, M.R.; Mentar, L.; Azizi, A.; Sahari, A.; Kahoul, A. *Mater. Chem. Phys.* 2009, 115, 385-390.

16. Sadale, S.B.; Patil, P.S. *Solid State Ionics* 2004, 167, 273–283.
17. Liu, W.; Chen, S.; Zhang, S.; Zhao, W.; Zhang, H.; Yu, X. *J. Nanopart. Res.* 2010, 12, 1355–1366.
18. Abdulkarem, A.M.; Li, J.; Aref, A.A.; Ren, L.; Elssfah, E.M.; Wang, H.; Ge, Y.; Yu, Y. *Mater. Res. Bull.* 2011, 46, 1443-1450.
19. Paracchino, A.; Laporte, V.; Sivula, K.; Grätzel, M.; Thimsen, E. *Nat. Mater.* 2011, 10, 456-461.
20. Zhang, Y.C.; Tang, J.Y.; Wang, G.L.; Zhang, M.; Hu, X.Y. *J. Cryst. Growth* 2006, 294, 278–282.
21. Wu, Z.; Huang, F.; Shen, Y.; Xie, A.; Song, X. *J. Nanopar. Res.* 2011, DOI: 10.1007/s11051-011-0417-9
22. NREL AM 1.5 Gobal solar spectrum derived from SMARTS v.2.9.2; <http://rredc.nrel.gov/solar/spectra/aml.5/>.
23. Hahn, N. T.; Ye, H.; Flaherty, D. W.; Bard, A. J.; Mullins, C. B. *ACS Nano* 2010, 4, 1977-1986.
24. Hahn, N.T.; Mullins, C.B. *Chem. Mater.* 2010, 22, 6474-6482.
25. Liang, Y.; Tsubota, T.; Mooij, L.P.A.; van de Krol, R. *J. Phys. Chem. C* 2011, 115, 17594–17598.
26. Berglund, S.P.; Flaherty, D.W.; Hahn, N.T.; Bard, A.J.; Mullins, C.B. *J. Phys. Chem. C* 2011, 115, 3794–3802.
27. Enache, C.S.; Lloyd, D.; Damen, M.R.; Schoonman, J.; van de Krol, R. *J. Phys. Chem. C* 2009, 113, 19351–19360.
28. Nakamura, R.; Tanaka, T.; Nakato, Y. *J. Phys. Chem. B* 2004, 108, 10617-10620.
29. Kim, M.J.; Cho, S.K.; Koo, H.C.; Lim, T.; Park, K.J.; Kim, J.J. *J. Electrochem. Soc.* 2010, 157, D564-D569.

Chapter 5: Spray Pyrolysis Deposition and Photoelectrochemical Properties of n-type BiOI Nano-Platelet Thin Films

INTRODUCTION

Photocatalysis is an active area of research due to its application in renewable and sustainable efforts such as artificial photosynthesis and hazardous pollutant removal.^{1,2} Classically, wide band gap materials such as TiO₂ (3.0 - 3.2 eV) have been employed extensively for these purposes at the laboratory scale,³ but in order to achieve commercial viability materials capable of absorbing and utilizing visible light ($420 < \lambda < 700$ nm), comprising nearly half of the terrestrial solar spectrum, must be developed. A particularly ambitious goal of photocatalyst research is the development of materials capable of acting as photo-electrodes for water splitting, the generation of molecular hydrogen and oxygen from water.⁴ Although a great deal of work has been performed in this area, further research of promising candidate materials is needed if reasonable solar conversion efficiencies are to be realized in such a photoelectrochemical (PEC) system.

One such material that has seen a recent surge of interest in the field of photocatalysis is BiOI.^{5,6,7,8,9} This layered oxy-halide compound is typically synthesized in solution by precipitation or solvothermal methods, leading to powders having a bright red color indicative of its excellent band gap for solar energy utilization (1.8 – 1.9 eV).^{5,6} Several such studies have found BiOI powders to be superior photocatalysts for the degradation of water-borne organic contaminants compared to other bismuth oxy-halides or doped TiO₂.^{7,8,9} The high photocatalytic activity of bismuth oxyhalides has been attributed to their superior charge separation and transfer as a result of their open, layered

crystal structure and more dispersive band characteristics compared to those present in transition metal oxides such as TiO_2 .¹⁰ Heterojunction photocatalysts such as BiOI-TiO_2 , BiOI-ZnO , and BiOI-AgI have also been studied for photocatalytic applications.^{11,12,13} Thin films of BiOI have recently been synthesized by successive ionic layer adsorption and reaction (SILAR) for characterization in photoelectrochemical solar cells, although the observed photocurrent (0.24 mA/cm^2) and efficiency (0.09%) were somewhat low.¹⁴

One characteristic of such layered semiconductors is that they possess covalently bonded slabs that are joined together by van der Waals interactions. As a result, their single-crystal surfaces (formed at this so-called van der Waals face) do not have dangling bonds and are expected to be self-passivating, minimizing the influence of surface states and photocorrosion, making them particularly interesting for PEC applications.¹⁵ Additionally, the positions of the band edges of BiOI appear to be favorable for photo-oxidizing a variety of possible solution species.¹⁶ These characteristics provide significant motivation for the further study of BiOI thin film photo-electrodes. Although the earliest PEC studies on BiOI thin films exhibited p-type behavior and poor PEC performance,¹⁷ we have found that nanostructured films of *n-type* BiOI exhibiting strong PEC performance can be synthesized by a spray-pyrolysis technique from a solution containing dissolved $\text{Bi}(\text{NO}_3)_3$ and NH_4I precursors in ethylene glycol. PEC studies of these films revealed promising photo-conversion characteristics for the oxidation of facile electron donors such as I^- , although stability concerns must be addressed if such films are to be utilized as photoelectrodes in aqueous solutions. A deposition temperature of 260°C is found to be ideal for PEC performance, with photocurrents under AM1.5G

illumination reaching nearly 1 mA/cm^2 at $0.4 \text{ V vs. Ag/AgCl}$ in $0.25\text{M NaI/acetonitrile}$ for optimized conditions. When a 420 nm cut-on filter was applied the photocurrent remained nearly 80% of this value, demonstrating the high visible-light activity of these films.

EXPERIMENTAL SECTION

Precursor solutions containing bismuth and iodine were prepared by dissolving $\text{Bi}(\text{NO}_3)_3 \cdot 5\text{H}_2\text{O}$ (Alfa) and NH_4I (Acros) in ethylene glycol ($99+\%$, Acros). Ethylene glycol was employed as the solvent in order to dissolve bismuth nitrate and prevent its premature reaction with NH_4I . This precursor solution was loaded into a syringe and pumped through an ultrasonic spray nozzle (130 kHz , Sonotech) positioned above a hotplate in a ventilated enclosure. The spray parameters were controlled by a syringe pump (New Era), which was programmed to spray intermittently (a spray pulse, followed by a rest period) for a set number of deposition cycles. Various nozzle heights and spray parameters were investigated, and those selected for further study were a nozzle height of 12 cm , flow rates between 1.0 and 1.5 ml/min , a pulse volume of 0.3 ml , and a rest time of 25 s . The FTO substrates were mounted on a hotplate using a stainless steel mask, which allowed for a controllable deposition area. Prior to mounting, the substrates were ultrasonically cleaned with ethanol, rinsed with water and dried in air. The substrate surface temperature was calibrated for various hot plate settings using an infrared pyrometer (Micro-epsilon).

Scanning electron microscopy (SEM) and energy dispersive X-ray spectroscopy (EDX) were performed using a Quanta FEG 650 electron microscope (FEI). High-resolution transmission electron microscopy (HRTEM) was performed using a JEOL 2010F microscope with an accelerating voltage of 200 kV. X-ray diffraction (XRD) experiments utilized a Bruker D8 diffractometer. Mean grain size was calculated using the Scherrer equation:

$$D = \frac{K\lambda}{\beta \cos \theta} \quad (1)$$

Here D is the mean crystallite size, λ is the X-ray wavelength employed (0.154 nm), β is the full-width at half-max of the diffraction peak of interest. K is a shape factor, typically approximated as 0.9.³¹ X-ray photoelectron spectroscopy (XPS) was performed using a Kratos AXIS X-ray photoelectron spectrometer. The XPS spectra were calibrated to the adventitious carbon peak at 284.5 eV. Total transmittance and diffuse reflectance spectra were measured with a Cary 500 UV-vis-NIR spectrophotometer attached to a Labsphere DRA-CA-5500 integrating sphere. A bare FTO substrate was employed as a baseline standard, and corrected values of transmittance (T) were used to calculate the absorbance (A) using:

$$A = -\log_{10}(T) \quad (2)$$

The electrochemical and photoelectrochemical properties of each sample were tested using a 3-electrode electrochemical cell with a Ag/AgCl reference electrode and Pt wire counter electrode. All potentials are given relative to Ag/AgCl unless otherwise stated. The working electrode (the photoanode consisting of the BiOI film) with

illuminated area 0.21 cm^2 was immersed in the desired electrolyte (typically 0.25M NaI in acetonitrile) and illuminated by a 150 W solar simulator with an AM1.5G filter (Newport), the overall power density of which was calibrated to 100 mW/cm^2 at the sample surface using a thermopile (Newport). A 420 nm cut-on filter was employed at times to remove UV light. Anodic currents were plotted on the negative axis of the I-V plots. A monochromator (Newport) was employed to study spectral response and was used in conjunction with a monochromatic power meter and photodiode (Newport) to calculate the incident photon conversion efficiency (IPCE) from the measured photocurrent density (J_{ph}) and photon flux (I) at a given wavelength (λ) according to:

$$IPCE = \frac{J_{ph}(\lambda)}{I(\lambda)} \times 100\% \quad (3)$$

For each IPCE test, the monochromatic light power incident on the film was calibrated to $100 \text{ }\mu\text{W}$ ($476 \text{ }\mu\text{W/cm}^2$) at 460 nm , which was the wavelength of highest intensity. Monochromatic intensities ranged from this value down to $190 \text{ }\mu\text{W/cm}^2$, depending on the wavelength selected (see Appendix D, Figure D.1). A potentiostat (CH Instruments – CHI660D) was operated by a desktop computer to perform electrochemical measurements.

RESULTS AND DISCUSSION

Deposition parameters such as temperature, concentration, and number of cycles were varied in order to manipulate the PEC performance and discover the optimum conditions for the spray pyrolysis of BiOI thin films. Of these parameters, deposition temperature had the most influence on film properties. A precursor concentration of

0.06M (0.02M $\text{Bi}(\text{NO}_3)_3$ and 0.04M NH_4I) in ethylene glycol was sprayed onto the heated substrates held at various temperatures. The spray rate was adjusted accordingly to produce uniform films of similar thicknesses. Ethylene glycol was required as the solvent in order to prevent the premature reaction of Bi^{3+} with I^- and water to produce BiOI precipitate. Since the autoignition temperature of ethylene glycol (410°C) is much higher than the substrate temperatures studied, it is unlikely that there would be any effects of ethylene glycol combustion during deposition. Both potassium iodide and elemental iodine were tried as iodide sources in the precursor solution, but the former resulted in a large potassium contamination in the films and the latter did not react to form BiOI under any of the attempted conditions (only Bi_2O_3 was formed).

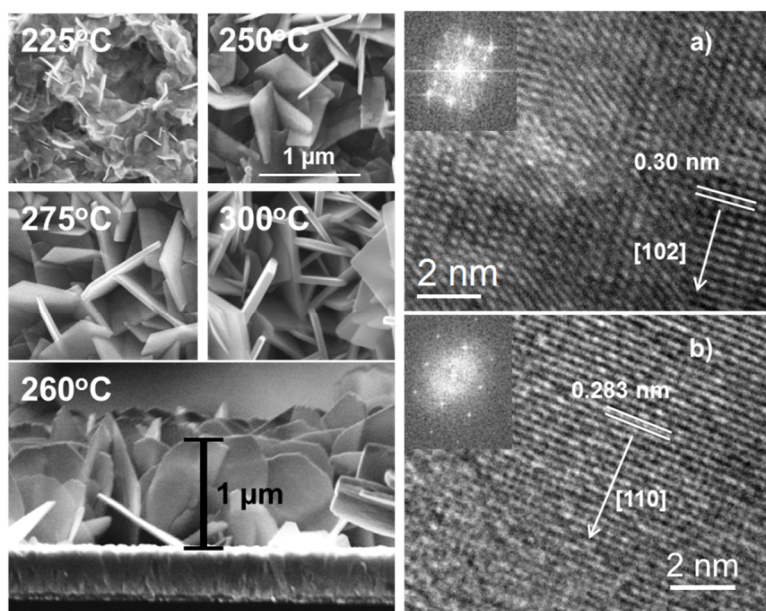


Figure 5.1. Left: SEM images of BiOI films deposited at the indicated temperatures on FTO-coated glass substrates. Right: (a) HRTEM image and discrete-fourier-transform (DFT) of a BiOI platelet deposited at 260°C , and (b) HRTEM image and DFT of a platelet deposited at 275°C along with the measured d-spacing.

SEM images of films deposited between 225 and 300°C revealed a clear trend in size and shape with increasing deposition temperature (Figure 5.1). In all cases nanoplatelets were observed, and these platelets grew larger and more square-shaped with increasing deposition temperature. At 225°C uniform platelet coverage was not observed over the entire sample suggesting that higher temperatures were necessary to consistently form platelets across the entire substrate. Profile SEM images indicated that the thicknesses of typical BiOI films were approximately 1 μm (Figure 5.1). Nearly all previous studies on BiOI show platelet-type structures as well, although the platelets are typically aggregated into larger (1-5 μm diameter) particles rather than remaining stable as a uniformly distributed thin film.^{5,18,19,20} These earlier studies have also demonstrated that BiOI platelets typically grow within the (001) plane, meaning that the c-axis is normal to the platelet faces.^{10,16,20} This results from the layered crystal structure of BiOI, which consists of non-bonding layers of [I-Bi-O-Bi-I] slabs stacked along the c-axis.^{20,21} This structure suggests that the platelet faces would normally be terminated by iodine, although vacancies and/or substitution by other species appears to occur in some cases. Another major implication of this layered structure is that the electronic properties of BiOI are anisotropic, with better electronic conductivity within the (001) plane compared to along the [001] direction.

HRTEM analyses of films deposited at 260 and 275°C indicated that the platelets did not consistently form as single-crystals until 275°C. The nano-platelets deposited at 260°C were not single-crystalline in all cases, but tended to show a preferred in-plane (010) orientation (perpendicular to the b-axis), whereas platelets deposited at 275°C

showed an in-plane (001) orientation (perpendicular to the c-axis) (Figure 5.1). Due to the layered structure of BiOI, one would expect the (001) orientation to be the preferred structure. Estimates of average platelet thicknesses measured from SEM images increased from 24 to 43 nm as the deposition temperature increased from 225 and 300°C, respectively, although the standard deviations of the thicknesses measured in each film are 8 – 10 nm (Figure 5.2). XRD patterns of films deposited over this temperature range also showed an increase in peak sharpness as the deposition temperature increased, signifying the growth of larger crystals (Figure 5.2). All films showed polycrystalline patterns corresponding to tetragonal BiOI (powder diffraction file # 01-075-5209), and in each case the preferred orientation overall was (102) followed by (110).

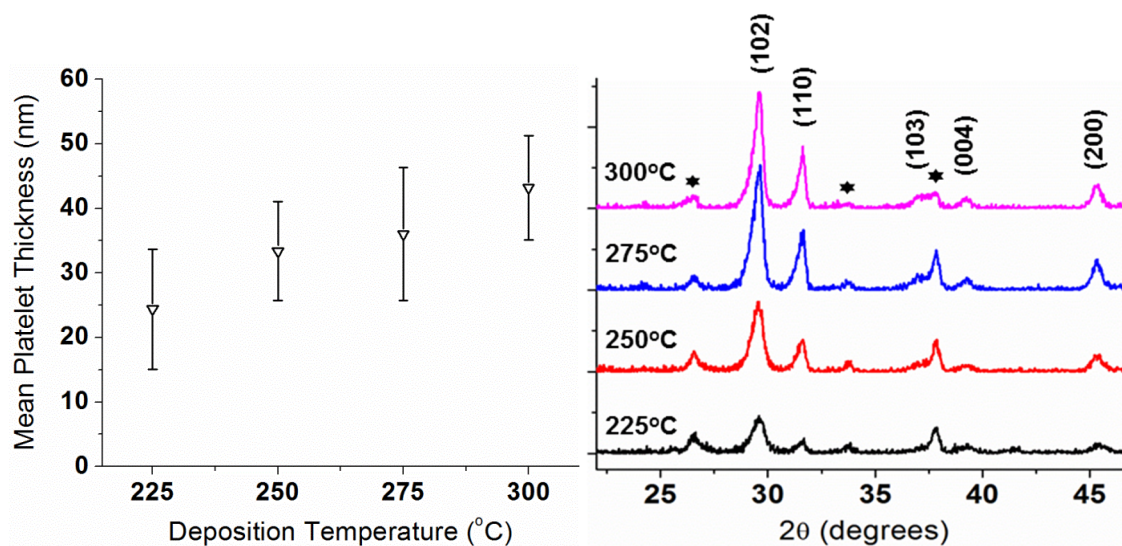
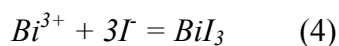


Figure 5.2. Left: Trend in mean platelet thicknesses measured from SEM images for various deposition temperatures. Right: XRD patterns for films deposited at the indicated temperatures. The indices of the peaks corresponding to BiOI are labeled, and the peaks from the FTO substrate are indicated by *.

Preliminary EDX results indicated that a stoichiometric (1:1) ratio of iodine to bismuth in the precursor solution resulted in very I-deficient films. However, a 2:1 ratio of iodine to bismuth achieved only slight iodine deficiencies in films deposited between 225 and 300°C (Figure 5.3). Only at 325°C was significant bulk iodine lost, presumably due to further oxidation of the films toward Bi₄O₅I₂, which we observed by XRD when BiOI powders were annealed to 350°C. EDX analyses also showed that the films were deficient in oxygen, although the accuracy of this technique for the detection of such light elements is poor. BiOI powders produced by a low temperature precipitation method also showed both oxygen and iodine deficiencies, indicating that anion vacancies may not be isolated to films deposited by spray pyrolysis alone and may occur in other BiOI materials also. To better understand the formation mechanism of BiOI, samples were deposited onto substrates held at lower temperatures and analyzed by XRD (see Appendix D, Figure D.2). At a substrate temperature of 150°C no crystalline phases were observed, but at 190°C XRD peaks corresponding to BiI₃ were observed, indicating that the reaction of the dissolved precursor compounds to form BiOI likely proceeds via two steps:



From XPS analyses the average surface ratio of I:Bi was determined to be 0.74 ± 0.03 for the samples deposited between 250 and 300°C, suggesting that surface iodine loss under exposure to the atmosphere at these temperatures may be unavoidable. A possible reason for this is the substitution of OH⁻ species for I⁻ on the surface of the films,

based on the enhanced ratio of O:Bi measured by XPS (0.8 to 1.1) relative to the bulk values measured by EDX (~ 0.7). The O 1s spectrum measured by XPS for a film deposited at 260°C is displayed in figure 5.3 along with fitted component peaks located at 529.9, 531.4, and 532.9 eV. The lowest binding energy peak is typical of that observed for metal oxides, indicating that it should be assigned to lattice O in BiOI.^{9,22} The other two fitted peaks are more difficult to assign, but likely represent surface bound O-containing species such as OH and/or organic impurities.⁹ The ratio of the lattice O peak area relative to the adsorbate peak areas increased monotonically with deposition temperature from 54% at 250°C to 65% at 300°C, indicating that some of these impurities may have been left behind by solution residue that does not completely decompose during deposition. However, part of this impurity signal is likely from the substitution of OH groups for I, resulting in the observed surface I-deficiency. The Bi 4f and I 3d core level spectra for the BiOI films showed peak positions corresponding to those expected for Bi³⁺ and I⁻ (see Appendix D, Figure D.3).^{9,22}

Optical characterization of films deposited at temperatures between 225 and 300°C was performed using UV-vis diffuse reflectance measurements. Measured transmittance (transmittance + reflectance) values of both the films and a reference FTO substrate were used to calculate absorbance values for each BiOI film (Figure 5.4). Qualitatively, the films' light absorption properties changed somewhat with deposition temperature. In particular, a noticeable shoulder was observed at about 640 nm in the spectrum of the film deposited at 225°C, but this feature diminished as deposition temperature increased, indicating that it is probably an impurity signal from the

incomplete decomposition and/or reaction of the precursors. Aside from this feature, the films' qualitative optical properties are similar, although the low coverage of the 300°C film resulted in significantly lower absorbance values across all wavelengths. When Tauc plots of $(\alpha h\nu)^{1/2}$ vs. photon energy were generated from the absorbance spectra, the films' indirect band gaps were seen to increase from about 1.7 to 1.8 eV over the given deposition temperature range (Figure 5.4). This increase in the apparent band gap probably originates from the removal of impurity states near the band edges. The indirect band gap reported for BiOI typically lies between 1.7 and 1.9 eV,^{5,7,8,16} and the ability of BiOI to absorb a large fraction of the visible spectrum is clearly one of its most interesting features as a prospective photocatalyst.

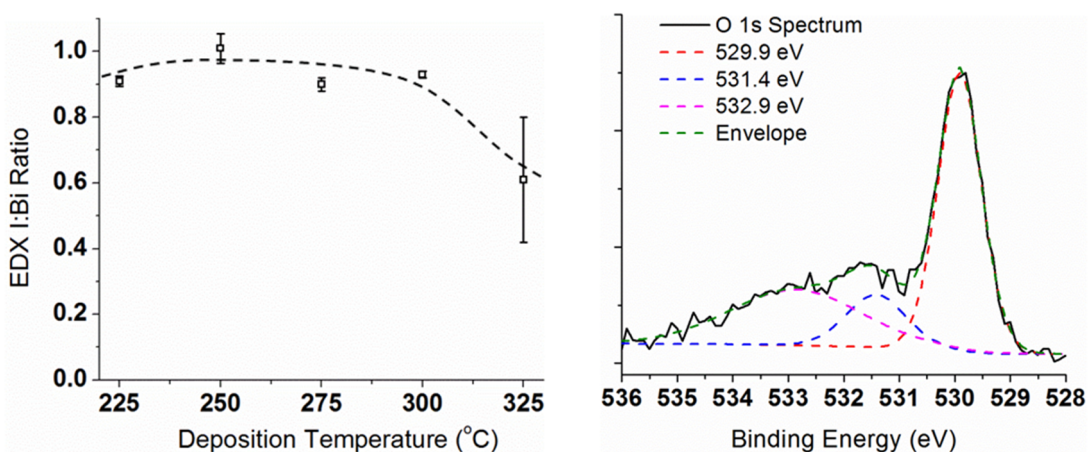


Figure 5.3. Left: EDX composition of films deposited at various temperatures. The dashed line is added to guide the eye. Right: Deconvoluted O 1s core-level spectrum obtained for a BiOI film deposited at 260°C. The position of each fitted peak is indicated in the legend.

The PEC performances of films deposited at different temperatures were tested in 0.25M NaI/acetonitrile. In these experiments I⁻ acted as a hole scavenger, minimizing the

influence of slow charge transfer kinetics to the solution and allowing the bulk charge separation and transport within the films to be analyzed more directly. PEC performance was assessed using both IPCE calculations under monochromatic illumination as well as linear sweep voltammetry (LSV) under 100 mW/cm^2 illumination from a solar simulator. In all cases clear cathodic shifts in open circuit potential under illumination and anodic photocurrents were observed indicating that these films were n-type, which is surprising given the fact that BiOI formed by the anodization of bismuth films in KI electrolyte were reported to be p-type in the earliest study of the PEC properties of BiOI.¹⁷ We observed n-type behavior in both aqueous and non-aqueous solutions and for a number of different electrolyte species indicating this is not an artifact of solution choice.

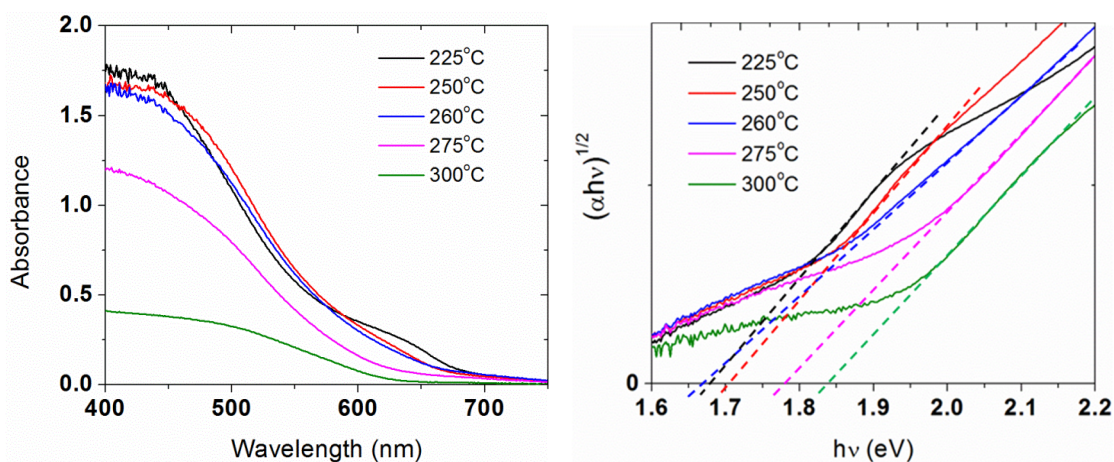


Figure 5.4. Left: Absorbance spectra of films deposited at various temperatures calculated from UV-vis transmittance measurements in an integrating sphere. Right: Tauc plots created for the absorbance values above, with linear extrapolations to $(\alpha h\nu)^{1/2} = 0$.

To our knowledge, this is the first claim of n-type conductivity put forth for BiOI in the literature. All recent studies employing particulate BiOI photocatalysts appear to have assumed, based on the original thin film study, that BiOI particles are p-type, despite the fact that a few of these recent studies show anodic photocurrents generated by films consisting of BiOI particles.^{11,12} Clearly, the common assumption of p-type conductivity in BiOI is not necessarily correct in light of the present results, which suggests that synthesis method may affect the majority carrier type of BiOI. The origin of n-type conductivity in the present films most likely arises from the formation of anion (I⁻ or O²⁻) vacancies, which are probably formed due to the elevated synthesis temperatures relative to those employed for the anodic synthesis of p-BiOI.¹⁷ EDX analyses indicated that the films were deficient in both oxygen and iodine, and this is the most logical explanation for the n-type nature of the films. Typical LSV's in NaI/acetonitrile under intermittent illumination for films deposited at various temperatures are displayed in figure 5.5. In general, films deposited at higher temperatures (275 – 300°C) showed smaller dark currents and larger photocurrents. Further experimentation revealed that intermediate temperatures between 250 and 275°C (*e.g.* 260°C) performed the best, reaching 0.9 mA/cm² at 0.4 V *vs.* Ag/AgCl, which is over 20 times higher than the photocurrent density observed for p-BiOI films deposited by anodization (Figure 5.5).¹⁷ Films deposited in this temperature range also showed a photocurrent onset at approximately -0.35 V *vs.* Ag/AgCl, whereas the onset of significant dark current occurred near 0.5 V. For lower deposition temperatures, the films exhibited relatively high dark currents over a wide potential range, which may be caused

by the higher impurity concentration suggested by the optical absorbance spectra. Although the removal of impurities and the improvement in crystallinity would be expected to improve PEC performance at even higher temperatures, these properties may be offset by the decreased light absorption and higher anion vacancy concentrations.

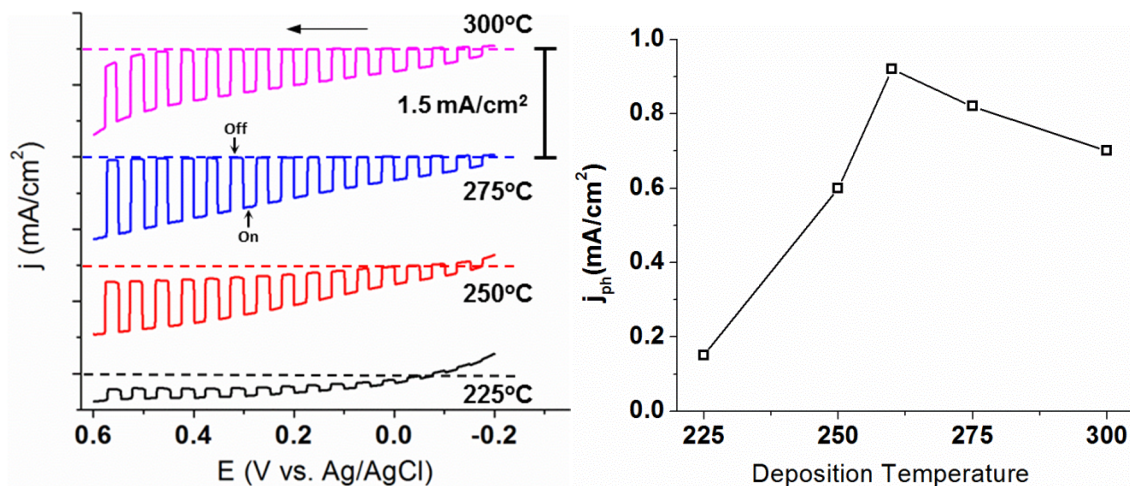


Figure 5.5. Left: LSV behavior in NaI/Acetonitrile for BiOI films deposited at the indicated temperatures. The anodic scan rate employed was 25 mV/s. Right: Photocurrent values measured at 0.4 V vs. Ag/AgCl for these films as well as a film deposited at 260°C.

When a filter was employed to remove UV light ($\lambda < 420$ nm) the photocurrents remained roughly 75% of those measured under full spectrum illumination for all the films, revealing their excellent PEC activity in the visible range (Figure 5.6). The ability of a photocatalyst or photoelectrode to respond to visible light effectively is very important for solar utilization. In this respect these n-BiOI films outperformed other nanostructured photoanodes, such as those composed of TaON or α -Fe₂O₃ nanotubes, which yielded visible-light photocurrent fractions of 47% and 50%, respectively, in an earlier work.²³ IPCE data measured at 0.4 V vs. Ag/AgCl in NaI/acetonitrile confirmed

the strong spectral response of these films for wavelengths greater than 420 nm. IPCE's for a typical film deposited at 260°C are displayed in figure 5.6, showing reasonably high conversion efficiencies of up to 25% at 360 nm. The IPCE values decreased significantly above 500 nm and became negligible (< 1%) above 620 nm. When the IPCE values were integrated over the AM1.5G solar spectrum²⁴ an overall photocurrent of 1.45 mA/cm² was calculated. However, the measured photocurrents for these films under simulated AM1.5G illumination was approximately 1 mA/cm², suggesting that the photoconversion efficiency was light intensity dependent.

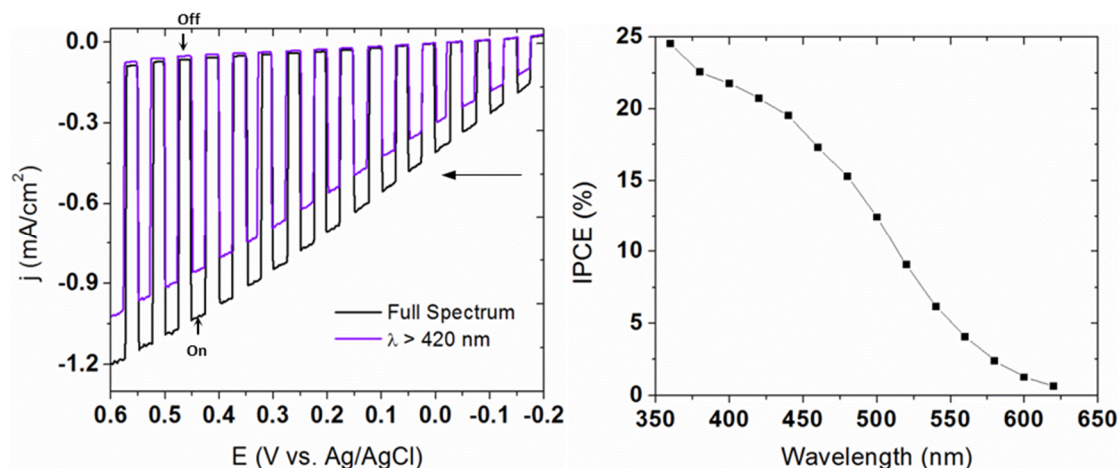


Figure 5.6. Left: LSV plot using a 3-electrode configuration in I⁻/acetonitrile both with and without a 420 nm cut-on filter for an optimized film deposited at 260°C. The anodic scan rate was 25 mV/s. Right: IPCE spectrum recorded at 0.4 V vs Ag/AgCl for a typical film deposited at 260°C with a peak light intensity of 476 μW/cm².

Indeed, when the light intensity was decreased from 100 mW/cm² to 67 and then 50 mW/cm², a sub-linear power law dependence between the photocurrent and light intensity ($J \propto I^{0.59}$) became apparent, in contrast with the linear dependence observed

under low intensity monochromatic ($\lambda = 460$ nm) illumination (Figure 5.7). Deviation from linear photocurrent vs. intensity behavior could be caused by several factors such as the direct recombination of conduction band electrons with valence band holes in the space charge region (Langevin recombination) or by surface defects.^{25,26} As an example of the latter case, Parkinson, *et al.* observed a pronounced sub-linear dependence for single-crystals of the layered compounds n-WS₂ and n-MoS₂ containing many surface steps. Crystals with well-cleaved surfaces, on the other hand, showed linear photocurrent vs. intensity response even at high intensities, suggesting that surface states can play a significant role.²⁶ White, *et al.* also observed an influence of unpassivated surface states on the light intensity dependence of another layered compound, n-WSe₂.²⁷ Their results suggested that exposed non-van der Waals faces (surface states) could facilitate the transfer of conduction band electrons to oxidation reaction products such as I₃⁻, which are present at higher concentrations when high light intensities are employed. This is a very reasonable explanation for the observations in the present study since these films expose many such non-van der Waals surfaces.

I-V behavior was also measured using a 2-electrode configuration and the I⁻/I₃⁻ redox couple (see Appendix D, Figure D.4). Short circuit current densities of ~0.48 mA/cm² were attained under AM1.5G illumination, which are twice as high as those measured in a previous study on BiOI nano-flake solar cells.¹⁴ However, the open circuit voltage we observed is lower than that reported in the previous study (0.45 vs. 0.62 V). Further optimization of PEC cell geometry and electrolyte may afford further improvements in these properties.

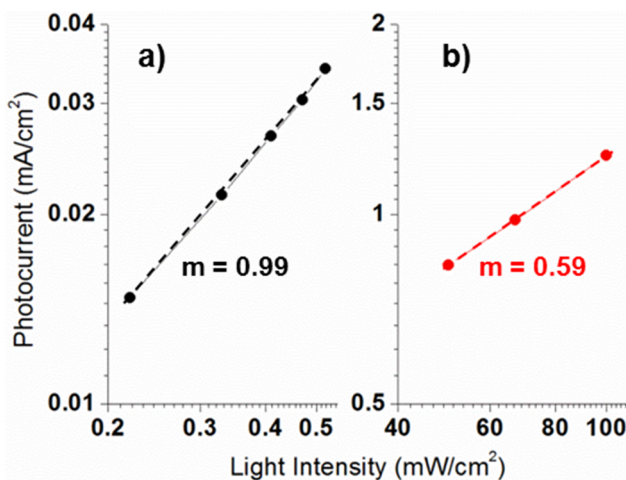


Figure 5.7. Log-log plots of photocurrent vs. light intensity at 0.4 V vs. Ag/AgCl for a film deposited at 260°C in the low (a) and high (b) light intensity regimes. The slopes of the resulting plots are indicated.

Further investigation of films deposited at various temperatures was accomplished using electrochemical impedance spectroscopy (EIS) in a solution of 0.5M NaI and 0.05M I₂ in acetonitrile. Impedance data was collected over a range of potentials between -0.2 and 0.5 V vs. Ag/AgCl, and the results for frequencies between 0.5 and 5 kHz were fitted by an RC circuit to generate Mott-Schottky plots of C_{sc}^{-2} vs. potential, where C_{sc}^{-2} is the space charge capacitance of the semiconductor electrode. The slopes and x-intercepts of such plots are often used to estimate the donor density (N_d) and flat-band potential (E_{fb}) of semiconductor films. Although these particular films are not ideal for Mott-Schottky analysis due to their nanostructured, polycrystalline nature, restricting the frequencies of measurement to moderately high values allowed for consistent results to be obtained. Representative Mott-Schottky plots using different frequencies for a film deposited at 260°C are shown in figure 5.8, indicating their linear character as well as

their frequency dependence caused by the non-ideality of the film-solution interface. The flat-band potentials derived from Mott-Schottky plots (frequency = 1 kHz) for films deposited at various temperatures are also shown in figure 5.8 and range from -0.23 to -0.39 V vs. Ag/AgCl, which are similar to the photocurrent onset potentials observed during LSV scans. Films deposited at 300°C did not yield reliable EIS results due to their lack of coverage of the FTO substrate, however.

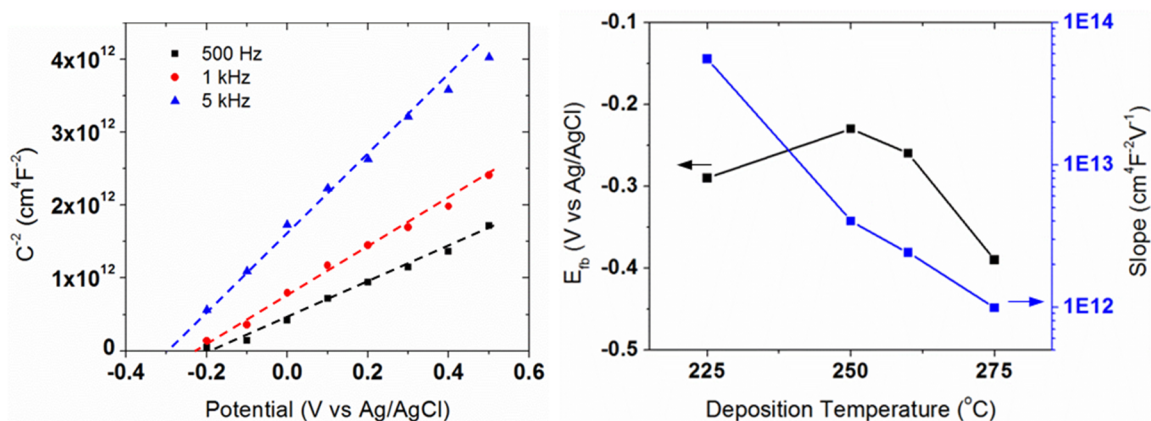


Figure 5.8. Left: Mott-Schottky plots measured in 0.5M NaI/0.05M I_2 in acetonitrile for a film deposited at 260°C. Right: Derived Mott-Schottky plot parameters at a frequency of 1 kHz displayed as a function of deposition temperature.

To further corroborate the flat-band potential measurements, open circuit potentials measured under high intensity (400 mW/cm^2) illumination were measured. Values of approximately -0.3 V vs. Ag/AgCl were observed for all deposition temperatures (Figure 5.9), similar to the results of the Mott-Schottky analyses in this solution, and these results indicate that the flat-band potential does not change significantly with deposition temperature. Another observation that could be made regarding the Mott-Schottky plots is that their slopes decreased consistently as the

deposition temperature increased. This implies that the donor concentration in the films depends on deposition temperature, which would be expected if the electron donors in these films are indeed anion vacancies, the concentration of which was likely elevated by the higher temperature conditions. The removal of charge-compensating impurities may also result the apparent increase in donor density, especially between 225 and 250°C. Differences in electrochemically active surface area could also partly explain some of the differences in the Mott-Schottky slopes, although the growth of larger features at high temperatures should have the opposite effect compared to the observed trend.

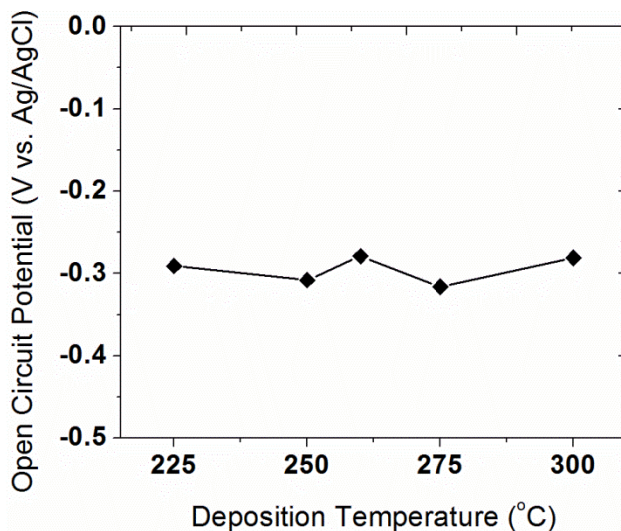


Figure 5.9. Open circuit potential measurements performed in 0.5M NaI in acetonitrile under 400 mW/cm² illumination for films deposited at various temperatures.

The PEC activity and stability of BiOI in aqueous solutions are of particular interest for practical application. To assess these, BiOI films were tested at various pH's and, at times, with the addition a hole scavenger, SO₃²⁻. In general, photocurrents measured in aqueous solutions were somewhat lower than those measured in acetonitrile,

which seems to have been caused by the reaction of water with the films, particularly at high pH, as discussed below. Markedly different behavior was observed between aqueous 1M Na₂SO₃ and 1M NaSO₄ solutions at neutral pH (Figure 5.10). Adding hole scavenger species clearly resulted in much higher photocurrents, particularly at more cathodic potentials, and greatly diminished the transient photocurrent behavior, indicating that charge transfer kinetics were improved. The oxidation of SO₃²⁻ to either SO₄²⁻ or S₂O₆²⁻ is known to be quite thermodynamically favorable, with an initial hole-transfer potential of 0.63 V vs. NHE.²⁸ Without SO₃²⁻ in the electrolyte the only possible fates of valence band holes in n-BiOI are trapping and recombination with electrons (evidenced by the transient photocurrents), the oxidation of water, or the surface oxidation of BiOI with water (photocorrosion).

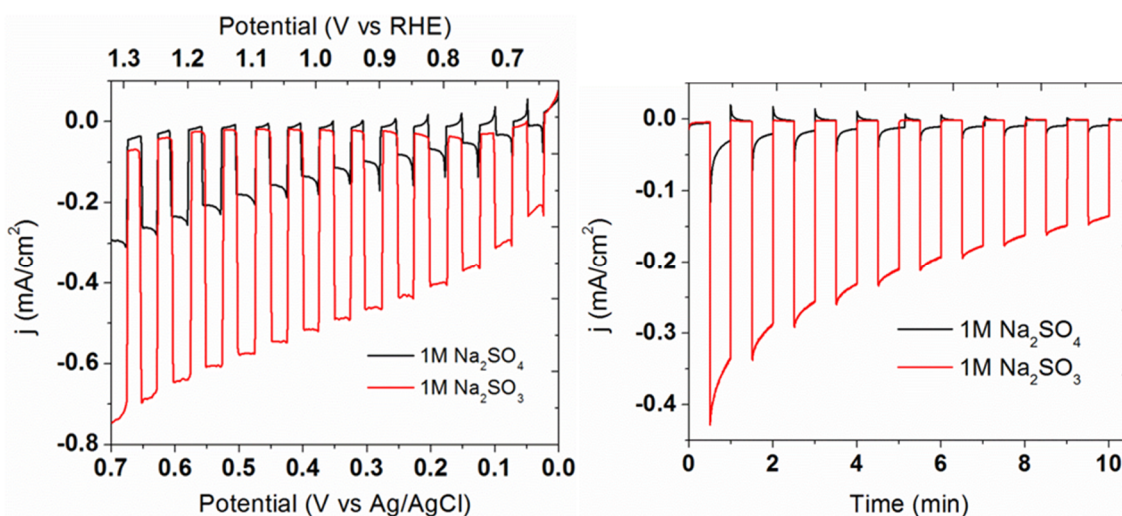


Figure 5.10. Left: LSV's recorded under intermittent illumination both with and without hole scavenger species at pH 7. Right: Photocurrent vs. time plots at a constant potential of 0.5 V vs. Ag/AgCl in the same solutions.

Comparing the photocurrent *vs.* time behavior of these films in the two solutions revealed that photocorrosion is a major factor in aqueous solutions, especially without a hole scavenger (Figure 5.10). This indicates that the kinetics of film photocorrosion are more facile than those of water oxidation, which probably results from a lack of overpotential available for water oxidation in the absence of a multi-electron transfer catalyst on the surface of BiOI.²⁹ Without such a catalyst water oxidation probably proceeds *via* the single hole oxidation of H₂O to OH•, which requires an electrochemical potential of 2.73 V *vs.* NHE, which is a full 1.5 V more positive than the potential for the four-hole oxidation of H₂O to O₂.²⁸ The predicted valence band edge of BiOI (roughly 2.4 V *vs.* NHE)^{11,30} is insufficiently positive to drive this initial charge transfer step efficiently using photogenerated holes. Indeed, a number of studies have suggested that OH• species are not produced on BiOI by valence band holes under illumination in aqueous solutions,^{13,16} consistent with these results.

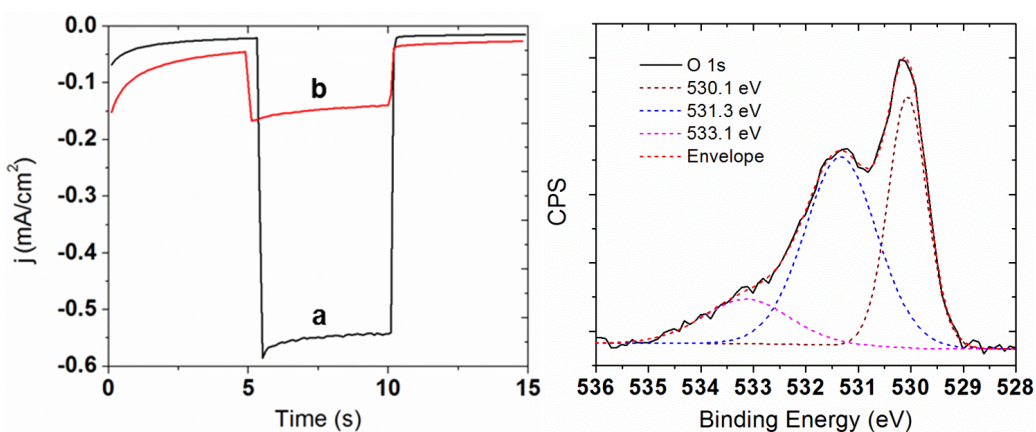


Figure 5.11. Left: Photocurrent performance at 0.4 V *vs.* Ag/AgCl in 1M Na₂SO₃ of a film deposited at 260°C measured (a) before and (b) after 20 min. soaking in the dark at pH 7. Right: XPS O 1s spectrum recorded after soaking a film (deposited at 260°C) in water for several hours.

Although the addition of SO_3^{2-} to aqueous solutions impeded photocorrosion to a large extent, it clearly did not fully suppress the degradation of the PEC activity of n-BiOI, in contrast to the stable behavior observed in acetonitrile solutions containing I⁻ (see Appendix D, Figure D.5). Upon further testing it became clear that even simply immersing the BiOI films in water for an extended period of time led to their deactivation. For example, the photocurrent of a film was measured briefly in 1M Na_2SO_3 after which it was allowed to soak in this solution in the dark for 20 min. Following this soaking period, the same test was performed, yet the photocurrent was roughly 25% of the initial value (Figure 5.11). Similar results were obtained for films soaked in pure water as well. XPS analyses performed on a film before and after immersion in water for an extended period of time showed substantial differences in the O 1s spectra, particularly in the pronounced growth of the OH peak at 531.3 eV compared to that observed in figure 5.2. However, no differences existed between XRD patterns for the films before and after soaking. This suggests that only a surface layer of bismuth hydroxide may form on these films upon their exposure to water, which would act as an insulating layer, inhibiting charge transfer. This reaction appeared to be more favorable at higher pH's, as the photocurrents measured in basic solution (pH > 12) were very low. The films appeared to be more stable in acidic electrolytes (pH 1 – 3) by comparison, but more concentrated acid solutions (pH < 1) led to their fast dissolution. Unfortunately, the chemical instability of BiOI appears to inhibit its use as a photoelectrode in aqueous solutions, despite many reports of its utilization for aqueous photocatalysis. It may be that the surface changes inhibiting the PEC activity in this case

have a less drastic effect on the photocatalytic mechanisms typically studied. The coating of a co-catalyst layer, however, may improve both stability and activity in aqueous environments.

CONCLUSIONS

N-type BiOI nanoplatelet films have been synthesized by spray pyrolysis for the first time, and their properties have been studied for various deposition conditions. Deposition temperature affected the platelets' size and crystallographic properties in addition to modifying their chemical composition and optical properties. PEC testing revealed that 260°C was the optimum substrate temperature during deposition for achieving high anodic photocurrents from the oxidation of I^- to I_3^- in acetonitrile (0.9 mA/cm² at 0.4 V vs. Ag/AgCl under AM1.5G). The films responded well to visible light (~75% photocurrent contribution), and possessed indirect band gaps ranging from 1.7 to 1.8 eV. The films showed poor stability in aqueous solutions due to the formation of a surface hydroxide layer that hindered hole transfer to electrolyte species. However, the protection of n-BiOI films with a catalyst layer or employing them as a bottom layer in a buried heterojunction scheme may allow their stable use for aqueous photoelectrochemistry.

REFERENCES

1. Bard, A. J.; Fox, M. A. *Accounts Chem. Res.* 1995, 28, 141-145.
2. Kabra, K.; Chaudhary, R.; Sawhney, R. L. *Ind. Eng. Chem. Res.* 2004, 43, 7683-7696.
3. Hashimoto, K.; Irie, H.; Fujishima, A. *Jpn. J. Appl. Phys.* 2005, 44, 8269–8285
4. Walter, M. G.; Warren, E. L.; McKone, J. R.; Boettcher, S. W.; Mi, Q.; Santori, E. A.; Lewis, N. S. *Chem. Rev.* 2010, 110, 6446–6473.
5. Lei, Y.; Wang, G.; Song, S.; Fan, W.; Pang, M.; Tang, J.; Zhang, H. *Dalton Trans.* 2010, 39, 3273–3278.
6. Zhang, X.; Zhang, L. *J. Phys. Chem. C* 2010, 114, 18198–18206.
7. Zhang, X.; Ai, Z.; Jia, F.; Zhang, L. *J. Phys. Chem. C* 2008, 112, 747-753.
8. Chang, X.; Huang, J.; Cheng, C.; Sui, Q.; Sha, W.; Ji, G.; Deng, S.; Yu, G. *Catal. Commun.* 2010, 11, 460–464.
9. Wang, Y.; Deng, K.; Zhang, L. *J. Phys. Chem. C* 2011, 115, 14300–14308.
10. Zhang, K. L.; Liu, C. M.; Huang, F. Q.; Zheng, C.; Wang, W. D. *Appl. Catal. B- Environ.* 2006, 68, 125–129.
11. Dai, G.; Yu, Liu, G. *J. Phys. Chem. C* 2011, 115, 7339–7346.
12. Jiang, J.; Zhang, X.; Sun, P.; Zhang, L. *J. Phys. Chem. C* 2011, 115, 20555–20564.
13. Cheng, H.; Huang, B.; Dai, Y.; Qin, X.; Zhang, X. *Langmuir* 2010, 26, 6618–6624.
14. Wang, K.; Jia, F.; Zhi, Z.; Zhang, L. *Electrochem. Comm.* 2010, 12, 1764–1767.
15. Tributsch, H. Electronic Structure, Coordination Photoelectrochemical Pathways and Quantum Energy Conversion by Layered Transition Metal Dichalcogenides. In *Photoelectrochemistry and Photovoltaics of Layered Semiconductors*, Aruchamy, A., Ed.; Kluwer: Dordrecht, 1992; pp. 83-116.

16. Li, Y.; Wang, J.; Yao, H.; Dang, L.; Li, Z. *J. Mol. Catal. A-Chem.* 2011, *334*, 116–122.
17. Poznyak, S. K.; Kulak, A. I. Photoelectrochemical properties of bismuth oxyhalide films. *Electrochimica Acta* 1990, *35*, 1941-1947.
18. Liu, H.; Cao, W.; Sua, Y.; Wanga, Y.; Wang, X. *Appl. Catal. B-Environ.* 2012, *111*, 271–279.
19. Xia, J.; Yina, S.; Li, H.; Xu, H.; Xu, L.; Zhang, Q. *Colloid Surface A* 2011, *387*, 23–28.
20. Ye, L.; Tian, L.; Peng, T.; Zan, L. *J. Mater. Chem.* 2011, *21*, 12479-12484.
21. Huang, W. L. *J. Comput. Chem.* 2009, *30*, 1882–1891.
22. Zhao, Z.; Liu, F.; Zhao, L.; Yan, S. *Appl. Phys. A* 2011, *103*, 1059–1065.
23. Banerjee, S.; Mohapatra, S. K.; Misra, M. *Chem. Commun.* 2009, 7137–7139.
24. NREL AM 1.5 Goba solar spectrum derived from SMARTS v.2.9.2;
<http://rredc.nrel.gov/solar/spectra/am1.5/>.
25. Chandra, S. Theoretical Models. In Photoelectrochemical Solar Cells; OPA: Amsterdam, 1985; pp. 193-236.
26. Kline, G.; Kam, K.; Ziegler, R.; Parkinson, B. A. *Sol. Energ. Mater.* 1982, *6*, 337-350.
27. White, H. S.; Abruna, H. D.; Bard, A. J. *J. Electrochem. Soc.* 1982, *129*, 265-271.
28. Wardman, P. *J. Phys. Chem. Ref. Data* 1989, *18*, 1637-1755.
29. Cowan, A. J.; Barnett, C. J.; Pendlebury, S. R.; Barroso, M.; Sivula, K.; Graetzel, M.; Durrant, J. R.; Klug, D. R. *J. Am. Chem. Soc.* 2011, *133*, 10134–10140.
29. Wang, W.; Huang, F.; Lin, X.; Yang, J. *Catal. Commun.* 2008, *9*, 8–12.
30. Holzwarth, U.; Gibson, N. *Nat. Nanotechnol.* 2011, *6*, 534.

Chapter 6: BiSI Micro-Rod Thin Films: Efficient Solar Absorber Electrodes?

INTRODUCTION

Recent interest in alternative thin film photovoltaic (PV) absorber materials has been motivated by problems related to the low absorption coefficient and therefore large required thicknesses of the silicon layers in crystalline-silicon (c-Si) solar cells, leading to excessive material costs. Direct bandgap materials such as $\text{CuIn}_{1-x}\text{Ga}_x\text{Se}_2$ (CIGS) or CdTe, which possess large absorption coefficients near their absorption threshold, afford an advantage over c-Si by allowing for the utilization of much thinner absorber layers, typically orders of magnitude thinner than those of c-Si cells.¹ However, these compounds include a substantial amount of indium and tellurium, respectively, (global reserve bases for In and Te are roughly 16 and 47 kton, respectively, as of 2008),² limiting their future viability as a widespread PV solution. Because of this, research is spreading to alternative materials such as $\text{Cu}_2\text{ZnSnS}_4$ (CZTS) that contain more earth-abundant elements.³⁻⁵ Such materials have shown quite promising photoelectrochemical (PEC) properties, even producing H_2 from the reduction of water at reasonable rates when employed as a photocathode.⁶

Bismuth would not generally be considered “earth-abundant” (reserve base ~ 680 kton) but is many times more abundant than indium, and for this reason bismuth based compounds such as Cu_3BiS_3 and $\text{Cu}_4\text{Bi}_4\text{S}_9$ have received interest as indium-free thin film absorber materials.⁷⁻¹¹ BiSI in particular, however, has received little study in the past, although a few of its properties, such as ferroelectricity (Curie temperature of -160°C)

and photoconductivity have been explored.¹²⁻¹⁴ Nitsche et al. measured photoconductivities for various V-VI-VII compounds, noting their wavelength of maximum photo-response (785 nm in the case of BiSI, as also noted by Sasaki).^{12,14} Horak et al. studied the photoelectric properties of BiSI in particular, observing anisotropic photovoltaic effects and n-type conductivity.¹³ These studies were performed on single crystals grown by various methods. More recently, polycrystalline BiSI has been synthesized by both hydrothermal reaction and spray pyrolysis from solution phase precursors, although only physiochemical characterization was performed in each case.^{15,16} To date there have not been any studies exploring the electrochemical or PEC behavior of BiSI.

EXPERIMENTAL SECTION

Synthesis

Precursor solutions containing bismuth, sulfur, and iodine were prepared by dissolving $\text{Bi}(\text{NO}_3)_3 \cdot 5\text{H}_2\text{O}$ (Alfa), Thiourea (Fisher), and NH_4I (Acros) in ethylene glycol (99+%, Acros). All three precursors remained stably dissolved in ethylene glycol. This precursor solution was loaded into a syringe and pumped through an ultrasonic spray nozzle (130 kHz, Sonotech) positioned above a hotplate in a ventilated enclosure under normal atmospheric conditions. The spray parameters were controlled by a syringe pump (New Era), which was programmed to spray intermittently (a spray pulse, followed by a rest period) for a set number of deposition cycles or layers. Various nozzle heights and spray parameters were investigated, and those selected for further study were a

nozzle height of 12 cm, pulse volume of 0.3 ml, and rest times of 25 s. Prior to deposition, the substrates were ultrasonically cleaned with ethanol, rinsed with water, and dried in air. The substrate surface temperature was calibrated for different hot plate settings using an infrared pyrometer (Micro-epsilon).

Characterization

SEM and EDX were performed using a Quanta FEG 650 electron microscope (FEI). Additional SEM was performed using a Hitachi S-5500 electron microscope. XRD experiments utilized a Bruker D8 diffractometer. Mean grain size was calculated using the Scherrer equation:

$$D = \frac{K\lambda}{\beta \cos(\theta)} \quad (1)$$

Here D is the mean crystallite size, λ is the X-ray wavelength employed (0.154 nm), β is the full-width at half-max of the diffraction peak of interest. K is a shape factor, typically approximated as 0.9.²⁷ XPS was performed using a Kratos AXIS X-ray photoelectron spectrometer. The XPS spectra were calibrated to the adventitious carbon peak at 284.5 eV. UV-vis-NIR transmittance spectra were measured with a Cary 500 spectrophotometer attached to a Labsphere DRA-CA-5500 integrating sphere. The true value of transmittance (T) was calculated by correcting for substrate and film scattering effects, and this was used to calculate film absorbance (A) using:

$$A = -\log_{10}(T) \quad (2)$$

The electrochemical and photoelectrochemical properties of each sample were tested using a 3-electrode electrochemical cell with a Ag/AgCl reference electrode and Pt

wire counter electrode. All potentials are given relative to Ag/AgCl unless otherwise stated. The working electrode (the photoanode consisting of the BiSI film) with illuminated area 0.21 cm^2 was immersed in the desired electrolyte (typically 0.25M NaI in acetonitrile) and illuminated by a 150 W solar simulator with an AM1.5G filter (Newport), the overall power density of which was calibrated to 100 mW/cm^2 at the sample surface using a thermopile (Newport). A 420 nm cut-on filter was employed at times to remove UV light. A monochromator (Newport) was employed to study spectral response and was used in conjunction with a monochromatic power meter and photodiode (Newport) to calculate the IPCE from the measured photocurrent density (J_{ph}) and photon flux (I) at a given wavelength (λ) according to:

$$IPCE = \frac{J_{ph}(\lambda)}{I(\lambda)} \times 100\% \quad (3)$$

For each IPCE test, the monochromatic light power incident on the film was adjusted to $100 \text{ }\mu\text{W}$ ($476 \text{ }\mu\text{W/cm}^2$) at 460 nm, which was the most intense wavelength. Monochromatic intensities ranged from this value down to $190 \text{ }\mu\text{W/cm}^2$ depending on the wavelength selected. A potentiostat (CH Instruments – CHI660D) was operated by a desktop computer to perform electrochemical measurements.

RESULTS AND DISCUSSION

X-ray diffraction (XRD) results for the as-deposited dark gray films indicated that all consisted of polycrystalline BiSI (PDF# 01-073-1171), although at 300°C there were several new peaks that could be indexed to a second, sulfur-rich Bi-S-I phase (PDF# 01-073-1157) (Figure 6.1). The mean size of the (210) crystallites calculated by the Scherrer

equation increased when deposition temperature was increased from 225 to 250°C, but remained relatively constant thereafter at approximately 26 nm (see Appendix E, Figure E.1). A previous study by Wang et al. suggested that the formation of BiSI by spray pyrolysis can occur *via* the reaction of BiI₃ and Bi₂S₃, which may form initially upon precursor decomposition on the substrate surface.¹⁰ Energy dispersive X-ray spectroscopy (EDX) analyses of films deposited at each temperature showed ratios of I:Bi and S:Bi somewhat below 1:1, indicating that the films are likely “doped” with many anion vacancies (Figure 6.1). Impurities from the precursor solution (C, N, O) could also be envisioned as possible dopants in these films. EDX gave no evidence of N, but did show about 1-3 at.% of O and C, although the influence of the substrate could not be ruled out completely.

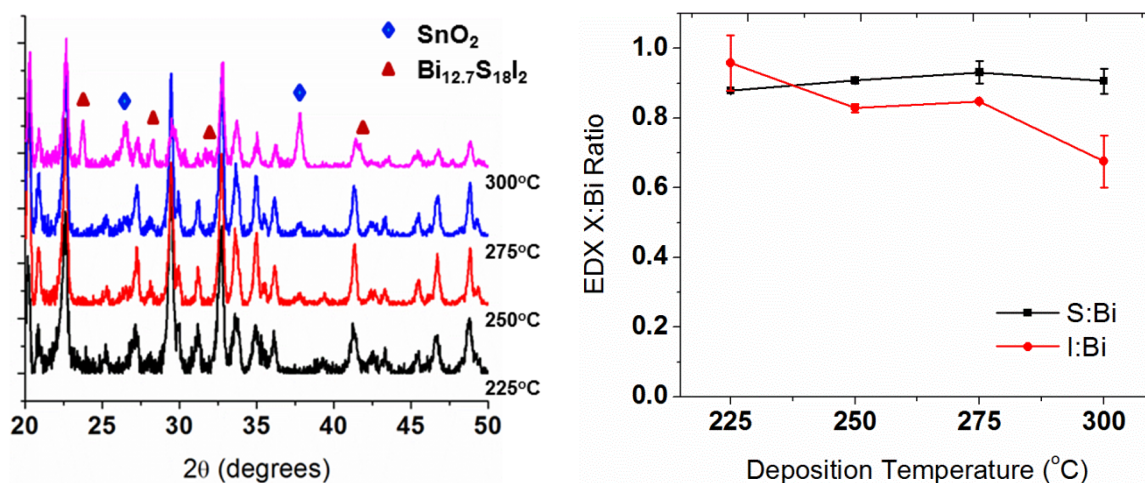


Figure 6.1. Bulk analyses of BiSI films sprayed at various temperatures. Left: XRD diffraction patterns with the non-BiSI peaks indicated. Right: EDX atomic % ratios of sulfur and iodine to bismuth.

Scanning electron microscopy (SEM) images show that the BiSI films consisted of rod-like crystals measuring roughly 0.5 to 1 μm across as deposited (Figure 6.2). Similar morphologies were observed in a previous study.¹⁰ Further electron microscopy of broken rod segments revealed that the large crystalline rods consisted of many smaller rod-shaped crystallites (Figure 6.2). The evolution of this bundled rod morphology is consistent with the crystal structure of BiSI, which features covalently bonded chains of atoms that are attached to other chains *via* weaker van der Waals forces.¹⁷ This information suggests that the micro-rods are oriented along the BiSI c-axis. Morphologically, films deposited between 250 and 275°C were quite similar, but the rod-like bundles deposited at 225°C appeared less uniform and more individual grains were visible near the ends of the rods, probably due to the fact that at 225°C there was insufficient thermal energy to completely merge these grains into the larger micron-sized structures. At 300°C the rod-like morphology was largely maintained, but some regions of the film showed patches of nano-platelets, most likely due to the formation of BiOI, which possesses such a morphology.¹⁸

X-ray photoelectron spectroscopy (XPS) was employed to further study the surface chemical differences between films deposited between 250 and 300°C. The ratios of I:Bi, S:Bi, and O:Bi are plotted in figure 6.3. Immediately surprising were the amounts of oxygen present on the surfaces of the films. When the O 1s spectra were examined further, a clear evolution in the chemical state of oxygen on the surface could be observed (Figure 6.4). In each case the peaks present in the O 1s spectra were best fit by a trio of Gaussian components located at binding energies of approximately 530,

531.3, and 533.2 eV. The peak at 530 eV most likely arises from O incorporated into the lattice, as was observed for BiOI.¹⁹ The peaks at 531.3 and 533.2 eV are typically assigned to surface adsorbates such as hydroxyl or carbonate species.^{19,20} At 250°C the O 1s spectrum was dominated by these higher binding energy components, indicating that the oxygen species are primarily surface impurities. A quantitative analysis of the fitted peak areas revealed a 5% contribution of the lattice-oxygen peak (530 eV). At 275°C the contribution of this peak increased to 16%, and at 300°C its contribution rose dramatically to 44% of the O 1s spectrum. This reveals that more and more oxygen was incorporated into the surface of the BiSI films as deposition temperature was increased. Although BiOI peaks could not be deconvoluted from the strong BiSI peaks present in the XRD patterns for these films, SEM images did reveal that nano-platelets formed on certain regions of the films deposited at 300°C. These nano-platelets were reminiscent of those found in BiOI films previously deposited in our group by spraying a sulfur-free, but otherwise identical, precursor solution. SEM images, combined with the O 1s XPS spectra, suggest that surface BiOI formation occurred readily at 300°C. This was further corroborated by the Bi 4f XPS spectra, which also evolved with deposition temperature (Figure 6.3). At 250°C, the Bi 4f spectrum displays relatively narrow peaks at 158.5 and 163.8 eV along with two smaller S 2p peaks at 161.3 and 162.6 eV, consistent with an XPS study of BiSI by Grigas et al.¹⁷ At 300°C the bismuth peaks broadened and shifted to higher binding energies. The Bi 4f spectrum for the intermediate temperature, 275°C, reveals shoulders on the higher binding energy sides of these primary peaks, indicating that a second pair of bismuth peak components “grows into” the spectrum as the

temperature is increased. The binding energies of this pair (159.3 and 164.6 eV) are quite similar to those observed for Bi^{3+} in BiOI films deposited in the absence of thiourea and are thus consistent with the suspected formation of surface BiOI at elevated deposition temperatures.

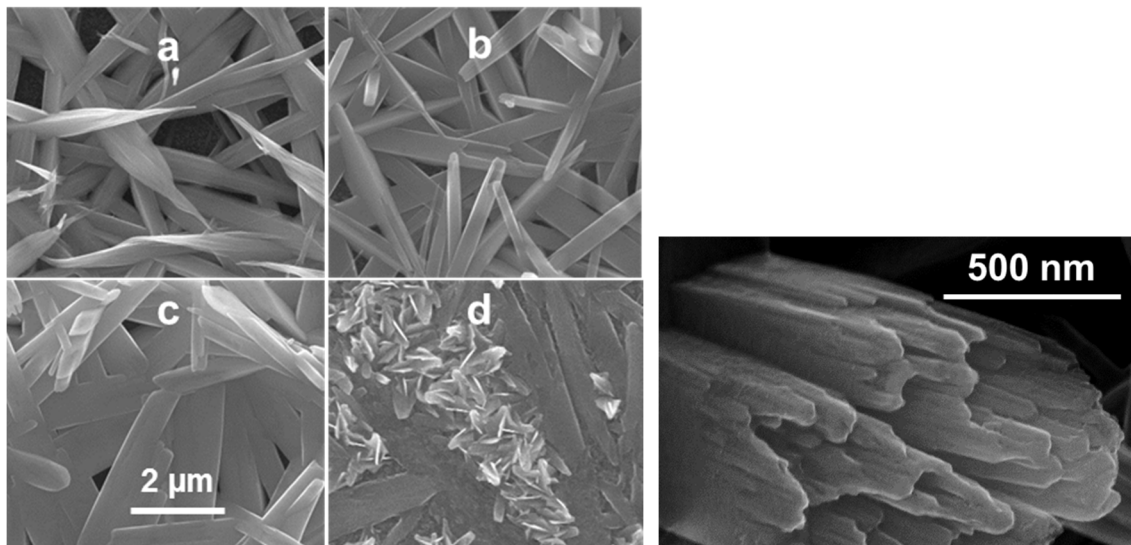


Figure 6.2. Electron microscopy images of the micro-rod morphology of the BiSI films. Left: SEM images of films deposited at a) 225, b) 250, c) 275, and d) 300°C. Right: STEM image of a broken micro-rod from a film deposited at 275°C, exposing the internal structure.

PEC testing was performed in a three-electrode cell in 0.25M NaI dissolved in acetonitrile. The films displayed anodic photocurrents (from the oxidation of I^- to I_3^-) with an onset of approximately -0.25 V vs. Ag/AgCl (see Appendix E, Figure E.2). Since the electrolyte contained a high hole scavenger concentration to minimize the effects of electron transfer kinetics, the onset of anodic photocurrents should provide a reasonable estimation of the flat-band potential (E_{fb}) in this solution. The oxidation of I^- in the dark was observed at potentials positive of 0.5 V. The photocurrent vs. deposition temperature

trend for the BiSI electrodes is shown in figure 6.5. Films deposited at temperatures between 250 and 275°C were the best performing, yielding photocurrents of nearly 5 mA/cm² at 0.4 V vs. Ag/AgCl. At 225°C the BiSI rods do not appear as well-formed when observed by SEM and likely possess a greater number of defects promoting recombination, leading to lower PEC performance. At 300°C the samples exhibited lower coverages and their partial conversion to BiOI could also cause them to exhibit lower photocurrent. Maximum open circuit voltages observed using a two-electrode configuration with I⁻/I₃⁻ as the redox couple (in acetonitrile) for films deposited at 275°C were approximately 0.37 V. Further optimization of redox couple and solvent should allow this value to be increased closer to the band gap value.

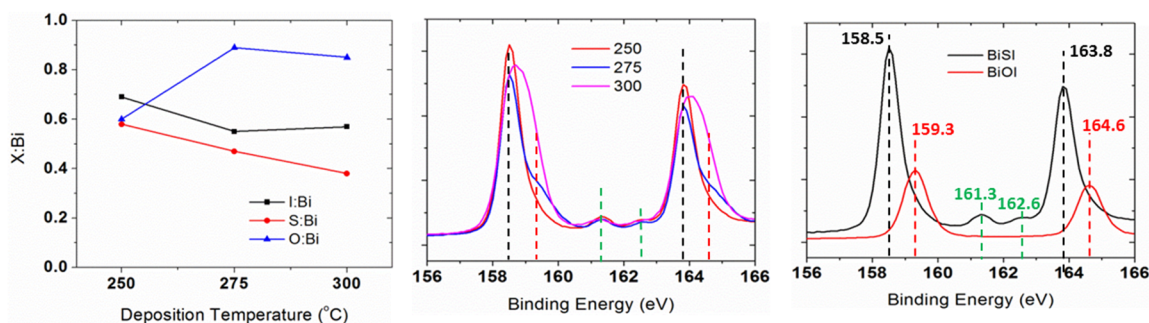


Figure 6.3. XPS analyses of BiSI films deposited at various temperatures. Left: Surface atomic % ratios of iodine, sulfur, and oxygen to bismuth. Middle: Core level Bi 4f spectra indicating the designations of the observed peaks. Right: Core level Bi 4f spectra comparing a BiSI and BiOI film deposited at 250°C, with the indicated binding energies of the observed peaks.

Linear sweep voltammetry (LSV) scans performed with and without a 420 nm cut-on filter in acetonitrile for a film deposited at 275°C are shown in figure 6.5, revealing that visible and infrared light contribute nearly all of the photocurrent observed under AM1.5G illumination. This is a very valuable property for terrestrial application

since the bulk of the available solar energy at the earth's surface lies in these spectral ranges. Although high photocurrents were achieved at relatively anodic potentials (e.g. 0.65 V vs. E_{fb}), one major performance limitation observed for these films was their relatively poor performance at potentials near E_{fb} . Instead of rising sharply beginning at E_{fb} and quickly reaching a light-intensity limited plateau (ideal semiconductor photoelectrode behavior), the photocurrent increases slowly and steadily beginning at E_{fb} and never reaches a true plateau current, i.e. the fill factor is low. This may be caused by a combination of high resistivity, short minority carrier (hole) diffusion length and/or small depletion layer widths at the tested potentials.²¹ Sasaki measured a room temperature resistivity on the order of $10^{10} \Omega\cdot\text{cm}$ and an electron drift mobility of $1 \text{ cm}^2/\text{s}\cdot\text{V}$ along the c-axis for BiSI single crystals.¹⁴ One may assume that the hole mobility is even smaller than the electron mobility in BiSI due to the larger hole effective mass, which can be inferred from band structure calculations in the literature.²²

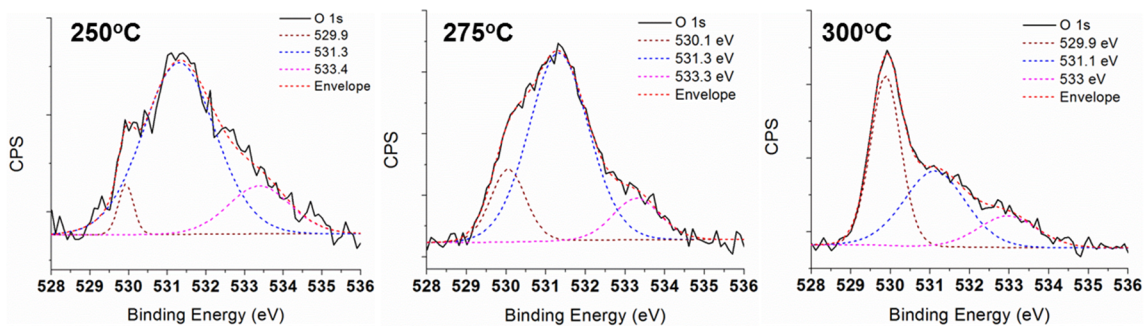


Figure 6.4. Core level O 1s spectra including the fitted component peak positions for BiSI films deposited at various temperatures.

Rough estimates of the hole diffusion lengths in n-BiSI films deposited at 275°C were calculated by plotting $\ln(1-\phi)$ vs. $(E-E_{fb})^{1/2}$ under monochromatic illumination

where ϕ is the quantum yield (see Appendix E, Figure E.3). It has been shown that the y-intercept of such plots, assuming negligible effects of charge transfer kinetics and space charge region recombination, can be used to estimate the hole diffusion length.^{23,24} These assumptions should be reasonable for large anodic biases and low photon fluxes in the presence of an electrolyte hole scavenger. The aforementioned plots, constructed using monochromated light with 420, 460, and 500 nm wavelengths (light intensity < 0.25 mW/cm²), yielded a mean hole diffusion length of approximately 5×10^{-6} cm. This value is lower than those found in more common solar cell absorbers and may be a result of their polycrystalline nature and relatively high defect concentration. Further improvements in film quality, then, could have a significant effect on photoconversion efficiency. LSV scans were also performed on films deposited on metal foil substrates (titanium and stainless steel) to assess whether film properties were substrate dependent. The photocurrent responses of BiSI films deposited at 275°C on both titanium and stainless steel were quite similar to those measured on FTO (see Appendix E, Figure E.4). This is an interesting result since it implies that this spray pyrolysis technique can be used to deposit V-VI-VII films with good PEC properties on a variety of substrates, which may be more desirable for practical applications.

Studies of the spectral response of films deposited at 275°C on FTO were performed employing monochromatic illumination to calculate IPCE spectra at 0 and 0.4 V vs. Ag/AgCl in acetonitrile (Figure 6.6). At 0.4 V the conversion efficiency rose quickly beginning at 800 nm, reaching a maximum of about 40% between 460 and 560 nm. Incident photon conversion efficiency (IPCE) spectra recorded at 0 V were

qualitatively similar, but the conversion efficiencies were much lower due to the inefficient separation of electrons and holes in the bulk of the film. UV-vis-NIR absorbance data collected by measuring the total transmittance (transmittance + diffuse reflectance) were quite consistent with the IPCE data, showing an absorption onset at about 800 nm and an absorption shoulder near 700 nm that qualitatively matches that observed in the IPCE spectra. Tauc plots of $(\alpha h\nu)^{1/2}$ and $(\alpha h\nu)^2$ vs. photon energy were used to calculate the indirect (1.57 eV) and direct (1.63 eV) bandgaps, respectively, which were very similar to literature values.²⁵ Absorption coefficients (α) calculated using the film thickness measured by profilometry (325 nm) exceeded $5 \times 10^4 \text{ cm}^{-1}$ for wavelengths of 600 nm and below (Figure 6.6). These values approach those of other popular thin film absorber materials.²⁶ The favorable optical properties of BiSI clearly contribute to their strong photo-response under AM1.5G illumination.

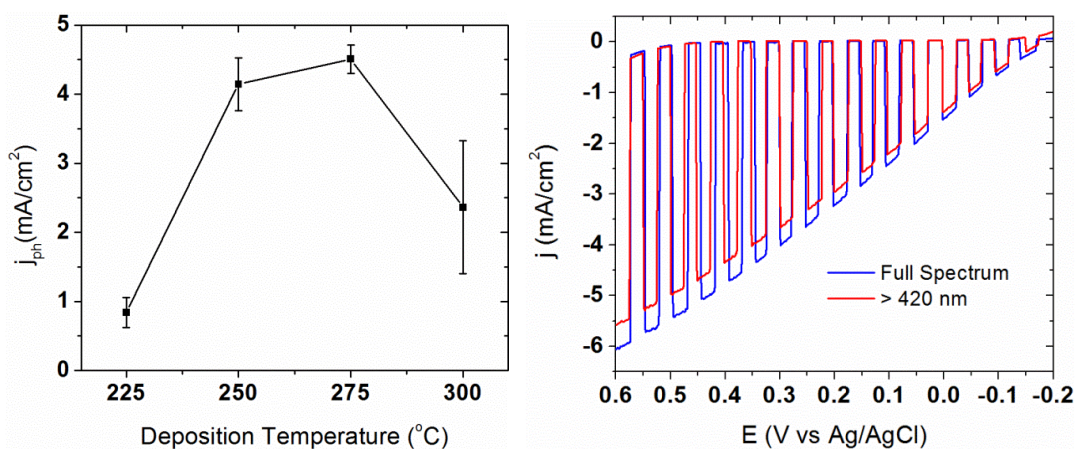


Figure 6.5. Left: Photocurrents recorded at 0.4 V vs. Ag/AgCl for films deposited at various temperatures. Right: LSV behavior (with and without a UV cut-off filter) of a film deposited at 275°C.

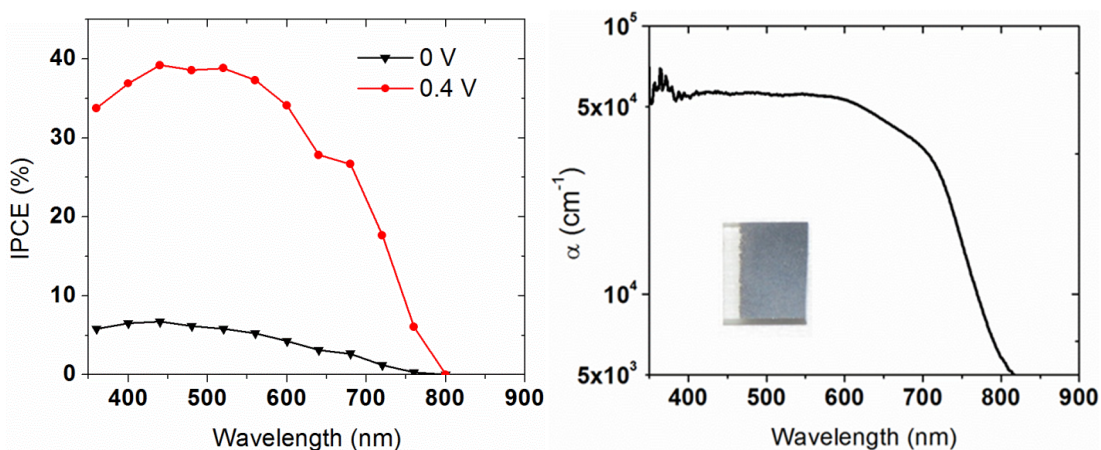


Figure 6.6. Left: IPCE spectra of a film deposited at 275°C. Right: Optical absorption coefficients calculated for a film deposited at 275°C from transmittance measurements along with a photograph of the film.

The PEC stability of typical n-BiSI films deposited at 275°C was assessed by applying a constant potential of 0.4 V vs. Ag/AgCl for 10 min (Figure 6.7). During these experiments, illumination was accomplished through the back of the substrate to avoid solution absorption effects due to the oxidation of I^- to I_3^- . Although the high initial photocurrents persisted for the first 1 to 3 min, they decayed continuously after this initial plateau, reaching currents only one third of the initial values after 10 min. To better understand the mechanism of deactivation, several films were deposited and tested for times ranging from 30 s to 5 min, after which they were examined by SEM and XPS. This provided “snapshots” of the film morphology and chemistry over the course of the stability test. SEM images revealed that film dissolution occurred throughout the testing period, meaning that the initial increase in photocurrent was likely caused by an increase in surface area due to PEC etching (Figure 6.7). XPS measurements did not reveal a trend in composition, indicating that the preferential dissolution of one or more

components was unlikely. A possible electrochemical mechanism, then, for the oxidative dissolution of the film involving photogenerated valence band holes (h^+) could be:



This reaction must proceed quite rapidly in order to effectively compete with the scavenging of holes via the oxidation of solution I^- to I_3^- . Another possibility is that highly reactive I_3^- generated at the surface of the film could decompose the film chemically. To investigate this, other electrolyte species such as SCN^- were employed as hole scavengers, but qualitatively identical behavior was observed. This points to a photocorrosion reaction as the reason for film deactivation. The fact that this photocorrosion reaction occurs even in acetonitrile indicates that n-BiSI films are probably not suitable for PEC applications without extensive modification. They may, however, prove useful for solid-state thin film solar cell applications.

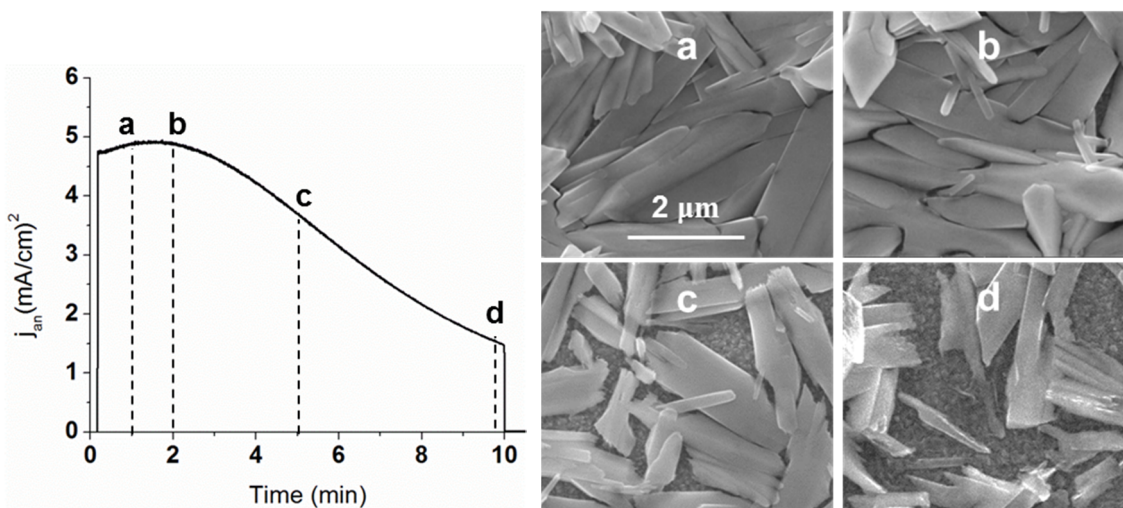


Figure 6.7. Left: Photocurrent vs. time behavior at 0.4 V vs. Ag/AgCl in 0.25M NaI in acetonitrile for a film deposited at 275°C. Right: SEM images of films tested under the same conditions for the indicated times: a) 1m, b) 2m, c) 5m, d) 10m.

CONCLUSIONS

The spray pyrolysis deposition and characterization of n-type BiSI thin films have been accomplished for a range of deposition temperatures, and the films displayed micro-rod morphologies consistent with the microscopic crystal structure of BiSI. PEC testing of these films in NaI/acetonitrile revealed strong photoconversion efficiencies throughout the visible range of 25 to 40% and photocurrents of up to 5 mA/cm² under AM1.5G illumination. These results demonstrate that n-BiSI can efficiently absorb light and transport photogenerated holes and electrons to the film surface and back contact, respectively. Deposition temperatures between 250 and 275°C appeared to optimize the films' performance due to their formation of well crystallized micro-rods without their subsequent surface conversion to BiOI. The convenience and scalability of this synthesis approach give it promising potential for depositing solar cell absorber layers composed of V-VI-VII materials.

REFERENCES

1. Shah, A.; Torres, P.; Tscharnner, R.; Wyrsh, N.; Keppner, H. *Science* 2012, 285, 692-698.
2. USGS Commodity Statistics and Information.
<http://minerals.usgs.gov/minerals/pubs/commodity/> (accessed April, 2012)
3. Katagiri, H.; Jimbo, K.; Maw, W.S.; Oishi, K.; Yamazaki, M.; Araki, H.; Takeuchi, A. *Thin Solid Films*, 2009, 517, 2455-2460.
4. Scragg, J.J.; Dale, P.J.; Peter, L.M. *Electrochem. Commun.* 2008, 10, 639-642.
5. Riha, S.C.; Fredrick, S.J.; Sambur, J.B.; Liu, Y.; Prieto, A.L.; Parkinson, B.A. *Appl. Mater. Inter.* 2011, 3, 58-66.
6. Yokoyama, D.; Minegishi, T.; Jimbo, K.; Hisatomi, T.; Ma, G.; Katayama, M.; Kubota, J.; Katagiri, H.; Domen, K. *Appl. Phys. Express* 2010, 3, 101202.
7. Gerein, N.J.; Haber, J.A. *Chem. Mater.* 2006, 18, 6297-6302.
8. Dale, P.J.; Loken, A.; Peter, L.M.; Scragg, J.J. *ECS Trans.* 2009, 19, 179-187.
9. Mesa, F.; Gordillo, G.; Dittrich, T.; Ellmer, K.; Baier, R.; Sadewasser, S. *Appl. Phys. Lett.* 2010, 96, 082113.
10. Li, H.; Zhang, Q.; Pan, A.; Wang, Y.; Zou, B.; Fan, H.J. *Chem. Mater.* 2011, 23, 1299-1305.
11. Temple, D.J.; Kehoe, A.B.; Allen, J.P.; Watson, G.W.; Scanlon, D.O. *J. Phys. Chem. C* 2012, 116, 7334-7340.
12. Nitsche, R.; Merz, W.J. *J. Phys. Chem. Solids* 1960, 13, 154-155.
13. Horak, J.; Cermak, K. *Czech. J. Phys. B* 1965, 15, 536-538.
14. Sasaki, Y. *Japan J. Appl. Phys.* 1965, 4, 614-615.
15. Su, X.; Zhang, G.; Liu, T.; Liu, Y.; Qin, J.; Chen, C. *Russ. J. Inorg. Chem.* 2006, 51, 1864-1868.
16. Wang, W.; Wang, S.Y.; Liu, M. *Mater. Res. Bull.* 2005, 40, 1781-1786.

17. Grigas J.; Talik, E.; Adamiec, M.; Lazauskas, V.; Nelkinas, V. *J. Electron Spectrosc.* 2006, *153*, 22-29.
18. Wang, K.; Jia, F.; Zhi, Z.; Zhang, L. *Electrochem. Comm.* 2010, *12*, 1764-1767.
19. Wang, Y.; Deng, K.; Zhang, L. *J. Phys. Chem. C* 2011, *115*, 14300-14308.
20. Zhao, Z.; Liu, F.; Zhao, L.; Yan, S. *Appl. Phys. A* 2011, *103*, 1059-1065.
21. Butler, M.A. *J. Appl. Phys.* 1977, *48*, 1914-1920.
22. Audzijonis, A.; Zaltauskas, R.; Sereika, R.; Zigas, L.; Reza, A. *J. Phys. Chem. Sol.* 2010, *71*, 884-891.
23. Kennedy, J.H.; Frese, K.W. *J. Electrochem. Soc.* 1976, *123*, 1683-1686.
24. Kennedy, J.H.; Frese, K.W. *J. Electrochem. Soc.* 1978, *125*, 709-714.
25. Park, S.A.; Kim, M.Y.; Lim, J.Y.; Park, B.S.; Koh, J.D.; Kim, W.T. *Phys. Stat. Sol. B* 1995, *187*, 253-260.
26. Stanbery, B.J. *Crit. Rev. Solid State* 2002, *27*, 73-117.
27. Holzwarth, U.; Gibson, N. *Nat. Nanotechnol.* 2011, *6*, 534.

Chapter 7: Concluding Remarks and Future Research

OVERVIEW OF COMPLETED WORK

In the previous chapters, we have discussed the deposition and characterization of a number of candidate materials for photoelectrochemical (PEC) applications. We have shown that techniques such as ballistic deposition, electrodeposition, and spray pyrolysis can be used to prepare and manipulate the properties of a number of novel photo-active materials by controlling composition and structure to varying degrees. Each material was characterized by its own combination of positive and negative traits. Factors such as light absorption, electron/hole transport, and electrochemical stability varied widely across the different materials studied, and each requires a unique approach to optimization. In the same way, we found that each film deposition technique possessed its own strengths and weaknesses. For example, although well-controlled ballistic deposition can be used to finely tune composition and morphology independently for some materials, it is quite costly in terms of both time and money and is poorly suited for some materials. The techniques of electrodeposition and spray pyrolysis, while more amenable to larger-scale application, provide less control over film growth and in the case of electrodeposition, is even more restrictive in terms of both film and substrate material selection. In studying such a range of materials and film growth techniques, further insight was gained into the underlying principles and application of semiconductor thin film photoelectrochemistry.

In chapters 2 and 3 we employed reactive ballistic deposition (RBD) to control the feature size and porosity of nanostructured $\alpha\text{-Fe}_2\text{O}_3$ photoanodes for water oxidation. As expected, higher deposition angles led to increased porosity, and film morphologies ranged from dense to nanocolumnar.¹ Although nanocolumnar films would generally be expected to outperform those possessing a more continuous structure due to differences

in minority carrier transport lengths to the film-electrolyte interface, we found that films possessing only modest porosity (deposited at 55°) resulted in the highest photocurrents. The reasons for this appear to be related to poor electron transport in thick hematite films (the more porous the film, the thicker the film must be to absorb many photons), as well as surface recombination, which becomes more problematic as a greater number of surface trap states are exposed on the films deposited at higher angles. Utilizing co-evaporation to deposit hematite films doped with titanium or tin showed much different behavior (higher deposition angles were more optimal), and the problems of electron transport and surface recombination were apparently reduced, leading to photoconversion efficiencies approximately twice as high (IPCE up to $\sim 30\%$ for titanium-doped) as in the undoped case.² The precise mechanisms of these improvements are still somewhat mysterious, although the results suggest that a combination of electronic doping and reduction of surface recombination play the largest roles. Despite these improvements, the overall performance of hematite photoanodes for water oxidation remains insufficient for practical application due to its relatively low efficiency for converting visible-light photons, despite its 2.1 eV band gap, and the large band bending (*i.e.* applied bias) required to achieve high charge separation and low surface recombination rates.

In chapter 4 an entirely different technique, electrodeposition, was used to synthesize the spinel p-type ternary oxide CuBi_2O_4 .³ Whereas hematite has received extensive study in the past, CuBi_2O_4 is a newly discovered photocathode material that showed promise for water splitting applications in a recent combinatorial study.⁴ In order to conduct a more rigorous study of its PEC properties, we selected electrodeposition as a fast, low cost deposition technique. Deposition potential and bath concentration were found to have the greatest effects on composition and morphology. Well crystallized films of p- CuBi_2O_4 consisting of interconnected particles roughly 200 nm in diameter

were achieved after annealing the as-deposited metallic films. PEC results indicated that the band edge positions of CuBi_2O_4 make it nearly ideal as a photocathode for hydrogen evolution, with a flat-band potential near 1.1 V vs. RHE. Although the reported band gap of CuBi_2O_4 is 1.5 eV,⁴ our optical spectra suggested that light absorption was essentially negligible for photon energies lower than 1.8 eV. Photoconversion vs. wavelength experiments gave similar spectral results, and also indicated that the films had poor conversion efficiencies, on the order of 1 - 2% maximum. Front vs. back-side illumination experiments as well as comparison with films deposited by ballistic deposition indicated that charge transport is very poor in CuBi_2O_4 . Photocorrosion *via* the reduction of Cu^{2+} to Cu^+ was confirmed by XPS and is a concern for future application of this material for aqueous photoelectrochemistry.

In chapters 5 and 6 we investigated two other bismuth containing compounds, BiOI and BiSI. BiOI, like CuBi_2O_4 , is a material that has received extensive study and has shown promising photocatalytic properties, particularly under visible light, due to its 1.8 eV band gap.⁵ The lack of available PEC characterization, however, motivated us to study photoelectrodes composed of this material with the hope that BiOI thin films could be used as photoanodes for water oxidation, based on expected band edge positions. Spray pyrolysis, another scalable synthesis technique employed for its flexibility, was used to deposit BiOI films in a single step.⁶ Although the films showed interesting nanoscale features, good crystallinity, and good optical properties, their surprising surface chemical instability in water prevented their study for water oxidation, and the films' PEC properties were instead investigated in acetonitrile, employing the oxidation of I^- as a model system. The films exhibited n-type conductivity, contrary to the p-type character mentioned extensively in the literature. N-type conductivity could be expected due to the formation of anion vacancies, the number of which appeared to increase with

deposition temperature. Indeed, deposition temperature had significant influence on the films' properties and performance, and 260°C was found to be optimum. Photoconversion efficiencies up to 20% in the visible range were observed, indicating that, aside from their aqueous instability, n-BiOI films possess promising PEC conversion characteristics.

As an extension of the BiOI study, the formation of BiSI was attempted due to its presumably narrower band gap leading to greater solar absorption potential. We discovered that simply adding thiourea as a sulfur source to the BiOI precursor solution resulted in the formation of well-crystallized BiSI when deposited under the same conditions. The PEC performance of n-BiSI greatly exceeded that of BiOI due to improvements in both light absorption and photoconversion efficiency, which remained strong until wavelengths of nearly 800 nm (1.6 eV).⁷ This led to photocurrents of roughly 5 mA/cm² for the oxidation of I⁻ in acetonitrile under AM1.5G illumination. This represents the first evaluation of BiSI's PEC performance and provides motivation for its further study as a solar absorber material along with other under-studied V-VI-VII compounds. Unfortunately, these films were unstable even in this non-aqueous system meaning n-BiSI films are more interesting for solid-state photovoltaic applications, rather than for photoelectrochemistry.

ONGOING AND FUTURE WORK

We are continuing studies of novel photoelectrode materials for both PEC water splitting and thin film solar cell applications. In particular, combinatorial studies are being undertaken to identify promising dopants to improve the photoconversion efficiency of CuBi₂O₄. CuBi₂O₄ remains an interesting photo-active material due to its combination of band gap and band edge positions, provided its stability and

photoconversion efficiency can be improved. Preliminary combinatorial results in our group have indicated that the incorporation of silver may improve both properties and further scaled-up bulk film experiments are currently being undertaken. Although new photocathode materials are certainly important, for overall PEC water splitting, the most room for improvement seems to lie in the water oxidizing material or photoanode, since the best available thin film photoanodes show neither the necessary photocurrents or photovoltages to approach practical implementation.^{8,9} To achieve this, stable photoanodes with band gaps of 2.0 eV or less and flat-band positions close to or even negative of 0 V *vs.* RHE will probably be required. The best oxide materials currently studied, α -Fe₂O₃ and BiVO₄, possess band gaps of 2.1 and 2.4 eV and flat-band potentials of roughly 0.4 and 0 V *vs.* RHE, respectively (Figure 7.1).

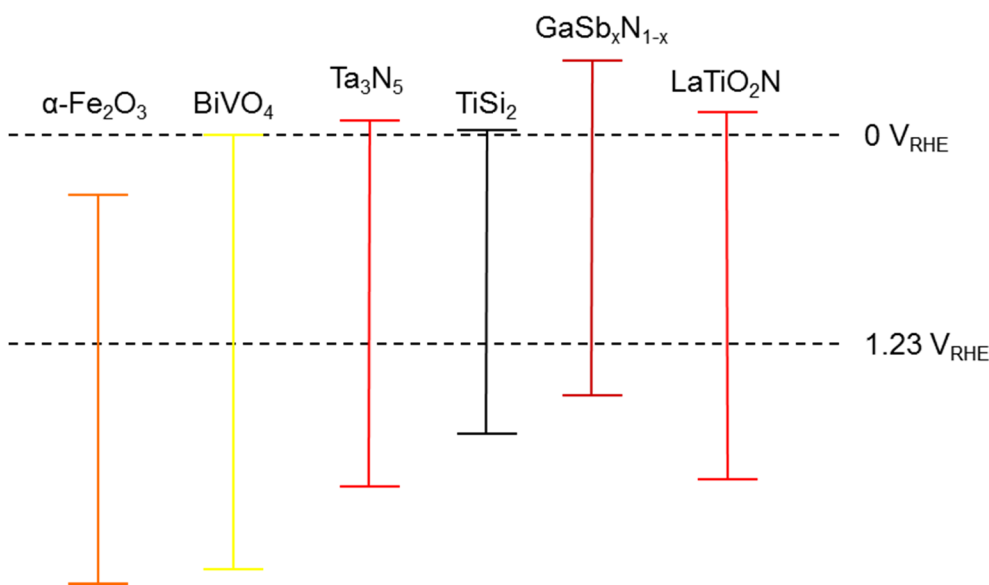


Figure 7.1. Band edge energetics of promising semiconductors for PEC water splitting compared to those of hematite and BiVO₄. The band edge positions relative to the water splitting redox potentials are estimated from data in the literature. The line color corresponds to the material band gap.

Two materials receiving some study as promising water splitting materials are Ta_3N_5 and TiSi_2 , although their stability with respect to oxidation is a concern.^{10,11} Theoretical studies have indicated that another non-oxide material, $\text{GaSb}_x\text{N}_{1-x}$, may also possess near-ideal band edge energetics for water splitting (as a photocathode, presumably), and pristine GaN is known to be stable for this application.¹² Although these materials are interesting objects of PEC research, preparing them as photoelectrodes is quite difficult compared to those of the more often studied metal oxides. In fact, $\text{GaSb}_x\text{N}_{1-x}$ has never been studied experimentally, but the formation of Sb-doped Ga_2O_3 followed by its ammonolysis may be a promising starting point. TiSi_2 has primarily been studied in the form of a commercial powder meaning that nanostructured film preparation has not been thoroughly investigated. Ballistic deposition may be a promising route to preparing films in order to facilitate a better understanding TiSi_2 's somewhat mysterious photocatalytic properties.

Another class of semiconductors receiving recent interest for PEC water splitting is the perovskite oxy-nitride group (*e.g.* LaTiO_2N).¹³ These materials show excellent visible light absorption and some have demonstrated the ability to generate hydrogen and/or oxygen from water under illumination.¹⁴ Some PEC data also exists for select members of this group, although the photocurrents demonstrated so far are relatively low.¹⁵ As with the previously mentioned nitride compounds, these materials are difficult to synthesize since they require high temperature ammonolysis conditions which are fatal to most substrates. Their preparation on tantalum foils may be possible, however, *via* the deposition of a parent perovskite oxide by spray pyrolysis or ballistic deposition, followed by ammonolysis.

Another important consideration for novel photoanode materials is the application of appropriate film coatings acting as either water oxidation catalysts capable of

facilitating multi-electron transfer steps or as hole-scavenging layers preventing surface recombination. Such strategies are critical for narrow band-gap photoanodes, which do not possess deep valence band edges providing high built-in overpotential for water oxidation *via* single electron transfer mechanisms. An appropriate coating material would enhance both the performance and stability of the photoanode material by minimizing the buildup of holes at the semiconductor-electrolyte interface.^{16,17} Studies of relatively abundant (*e.g.* cobalt based) water oxidation catalysts as applied to these new, narrower band gap semiconductor photoanodes would be very important to achieving necessary performance.

Regarding the chalco-halide work, we are conducting further investigation of BiSI-based photoanodes for thin film solar cells rather than for photoelectrochemistry due to their PEC instability. In particular, we are curious as to whether the substitution of selenium for sulfur enhances photovoltaic performance by increasing light absorption and/or improving the electronic properties by altering the structure of BiSI. Preliminary PEC results have confirmed that the absorption and conversion of NIR photons is improved, but the overall photoconversion efficiency is reduced slightly (Figure 7.2). Further understanding and manipulation of n-BiSI films and related compounds could lead to excellent novel thin film absorber materials for solar cells.

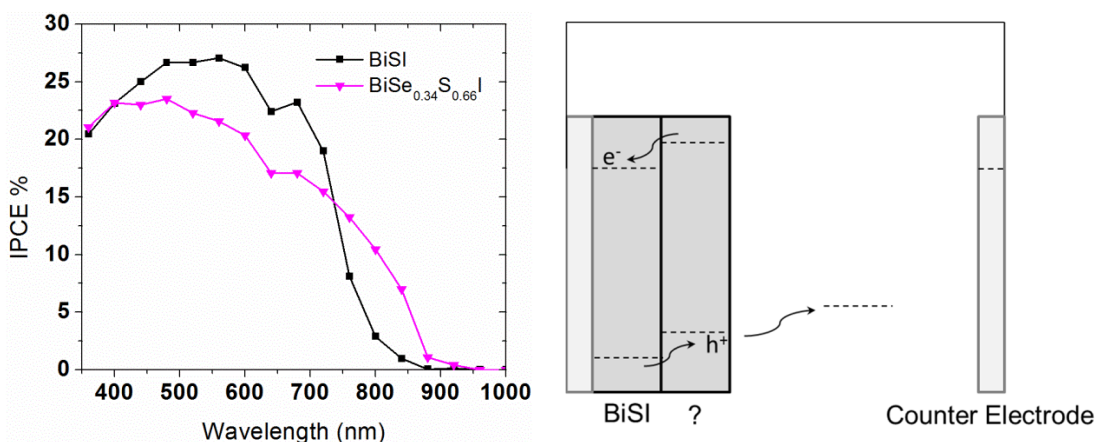


Figure 7.2. Left: Photoconversion spectra for pristine and Se-doped BiSI films under the short circuit condition (2-electrode configuration, 0 V vs. Pt) employing I^-/I_3^- in acetonitrile as the electrolyte. Illumination was accomplished through the backside of the photoanodes. Right: Proposed layered heterojunction scheme for a PEC cell employing a n-BiSI film and an optimized overlayer material.

We are also attempting to implement these films in actual solar cell devices using a solid-state hole conductor.¹⁸ Our hope is that these devices will exhibit high stability compared to the PEC solar cells we have studied with these films previously. A different approach that could also prove quite interesting for stabilizing n-BiSI films for PEC applications is to form a buried heterojunction with a n-BiSI film underlayer and a more stable overlayer semiconductor (Figure 7.2). However, proper matching of the band edge energetics appears difficult since there are almost no photoelectrochemically stable materials with valence band edges more negative than that of n-BiSI. In any case, there are a number of potentially exciting directions to pursue further research on these and other novel materials for solar energy conversion applications.

REFERENCES

1. Hahn, N. T.; Ye, H.; Flaherty, D. W.; Bard, A. J.; Mullins, C. B. *ACS Nano* 2010, 4, 1977-1986.
2. Hahn, N.T.; Mullins, C.B. *Chem. Mater.* 2010, 22, 6474-6482.
3. Hahn, N.T.; Holmberg, V.C.; Korgel, B.A.; Mullins, C.B. *J. Phys. Chem. C* 2012, 116, 6459–6466.
4. Arai, T.; Konishi, Y.; Iwasaki, Y.; Sugihara, H.; Sayama, K. *J. Comb. Chem.* 2007, 9, 574-581.
5. Dai, G.; Yu, Liu, G. *J. Phys. Chem. C* 2011, 115, 7339–7346.
6. Hahn, N.T.; Hoang, S.; Self, J.L.; Mullins, C.B. *ACS Nano* 2012, submitted
7. Hahn, N.T.; Self, J.L.; Mullins, C.B. *J. Phys. Chem. Lett.* 2012, 3, 1571-1576.
8. Tilley, S.D.; Cornuz, M.; Sivula, K.; Grätzel, M. *Angew. Chem. Int. Ed.* 2010, 49, 1–5.
9. Seabold, J.A.; Choi, K.S. *J. Am. Chem. Soc.* 2012, 134, 2186-2192.
10. Ishikawa, A.; Takata, T.; Kondo, J.N.; Hara, M.; Domen, K. *J. Phys. Chem. B* 2004, 108, 11049-11053.
11. Ritterskamp, P.; Kuklya, A.; Wustkamp, M.A.; Kerpen, K.; Weidenthaler, C.; Demuth, M. *Angew. Chem. Int. Ed.* 2007, 46, 7770 –7774.
12. Sheetz, R.M.; Richter, E.; Andriotis, A.N.; Lisenkov, S.; Pendyala, C.; Sunkara, M.K.; Menon, M. *Phys. Rev. B* 2011, 84, 075304.
13. Maeda, K.; Domen, K. *J. Phys. Chem. C* 2007, 111, 7851-7861.
14. Siritanaratkul, B.; Maeda, K.; Hisatomi, T.; Domen, K. *Chem. Sus. Chem.* 2011, 4, 74–78.
15. Paven-Thivet, C.L.; Ishikawa, A.; Ziani, A.; Gendre, L.L.; Yoshida, M.; Kubota, J.; Tessier, F.; Domen, K. *J. Phys. Chem. C* 2009, 113, 6156-6162.
16. Barroso, M.; Cowan, A.J. Pendlebury, S.R.; Grätzel, M.; Klug, D.R.; Durrant, J.R. *J. Am. Chem. Soc.* 2011, 133, 14868–14871.

17. Higashi, M.; Domen, K.; Abe, R. *J. Am. Chem. Soc.* 2012, *134*, 6968–6971.
18. Chung, I.; Lee, B.; He, J.; Chang, R.P.H.; Kanatzidis, M.G. *Nature* 2012, *485*, 486-489.

**Appendix A: Supplemental Information for Reactive Ballistic
Deposition of α -Fe₂O₃ Thin Films for Photoelectrochemical Water
Oxidation**

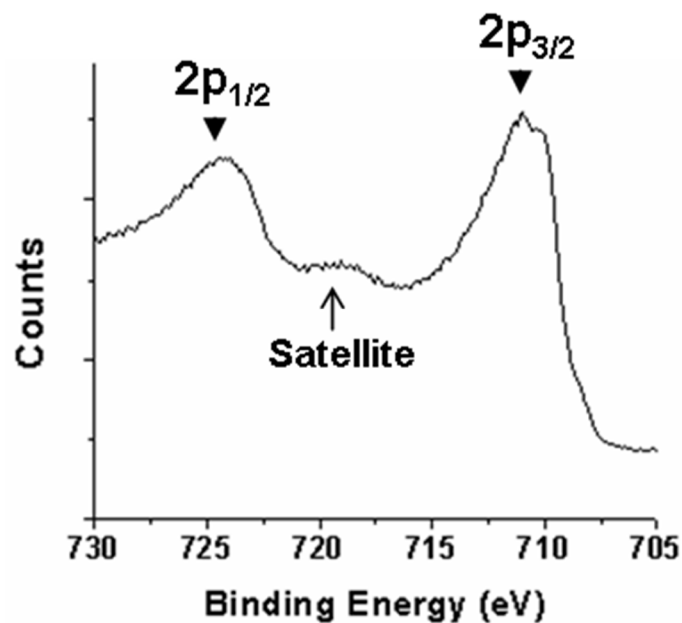


Figure A.1. XPS Fe 2p spectrum of a film deposited at 80° incidence and annealed at 450°C for 2 h. The core level designations of the primary peaks and the position of the visible satellite peak are indicated.

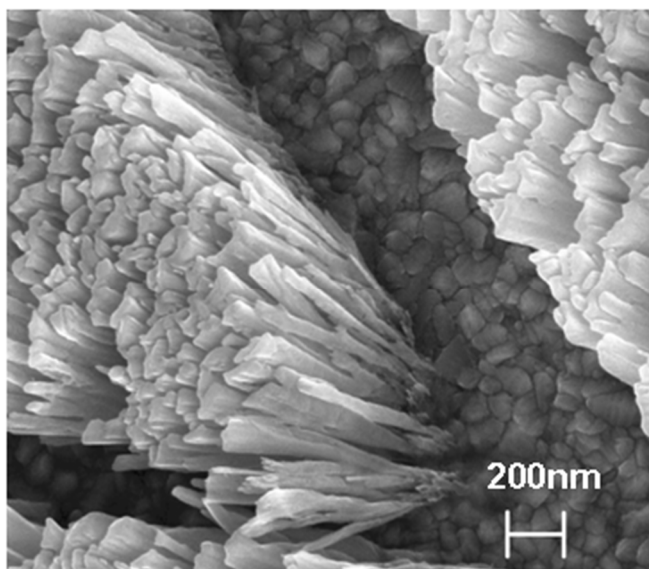


Figure A.2. SEM image of a 1 μm thick $\alpha\text{-Fe}_2\text{O}_3$ film deposited at 80°C . The film was scratched to provide a clearer view of the nanocolumnar structure.

Appendix B: Supplemental Information for Photoelectrochemical Performance of Nanostructured Ti- and Sn-doped α -Fe₂O₃ Photoanodes

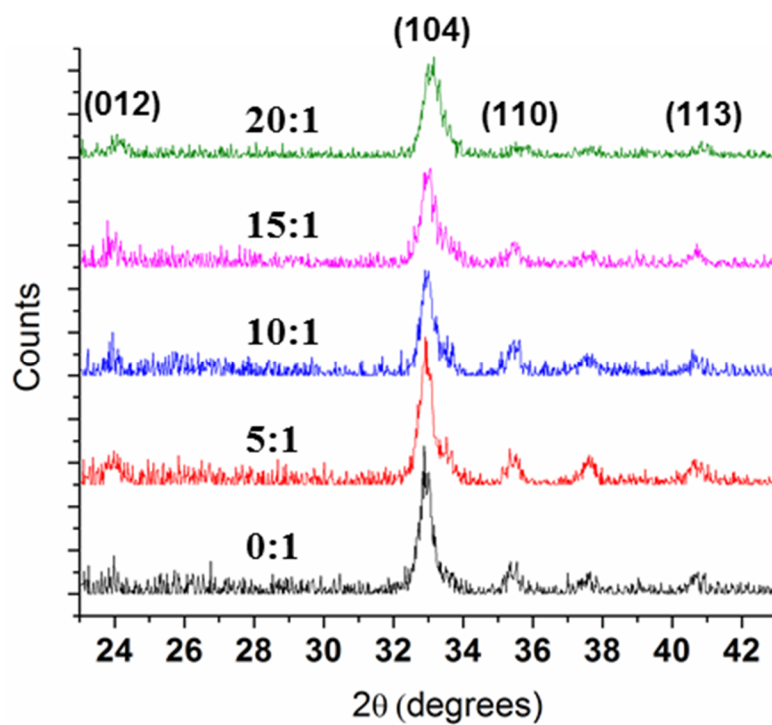


Figure B.1. Grazing incidence X-ray diffraction patterns for Ti-doped films deposited at 75° incidence with various flux ratios of O₂:Fe. The un-indexed peak at 37.5° belongs to cassiterite (SnO₂).

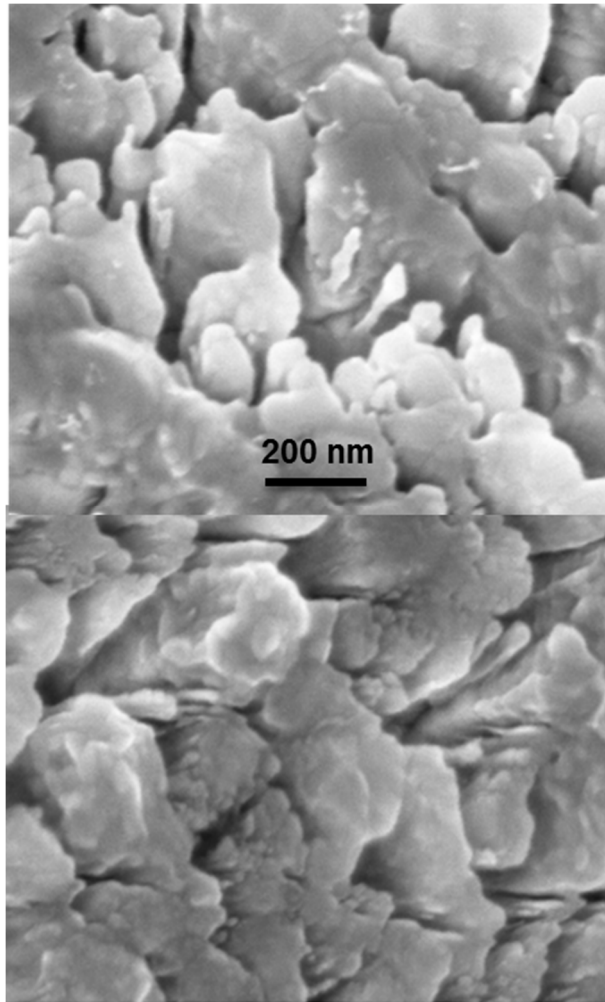


Figure B.2. SEM images of 5% Ti-doped samples deposited at 75° incidence and annealed to either 400°C (bottom) or 550°C (top) for 2 h.

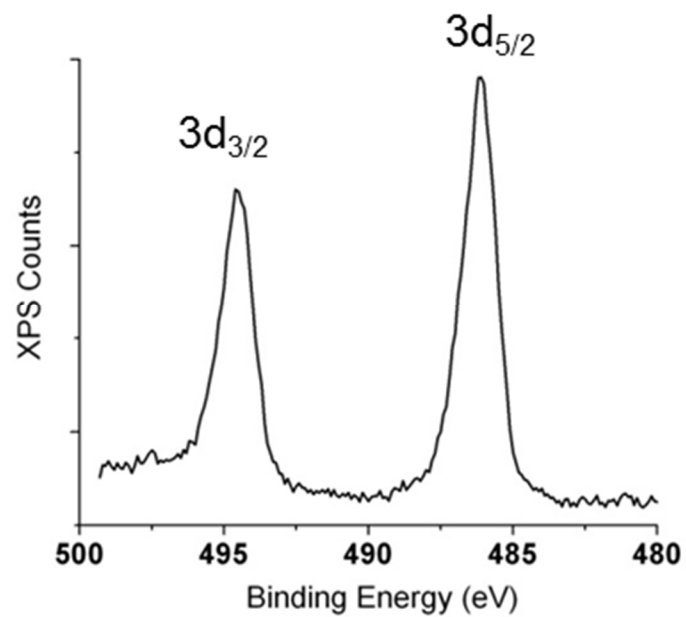


Figure B.3. XPS Sn 2p spectrum for a 4% Sn-doped α -Fe₂O₃ film, with the indicated core level peak designations.

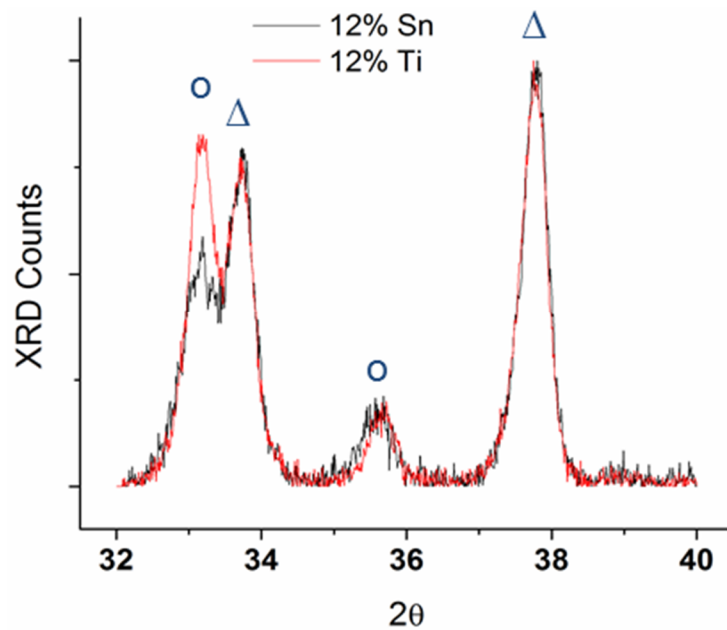


Figure B.4. XRD profiles of 12% Ti or Sn-doped α -Fe₂O₃ films deposited at 75°C incidence and annealed to 550°C for 2 h. Two-theta peak positions for hematite (PDF #97-002-4004) (o) and cassiterite (PDF #97-000-9163) (Δ) are indicated.

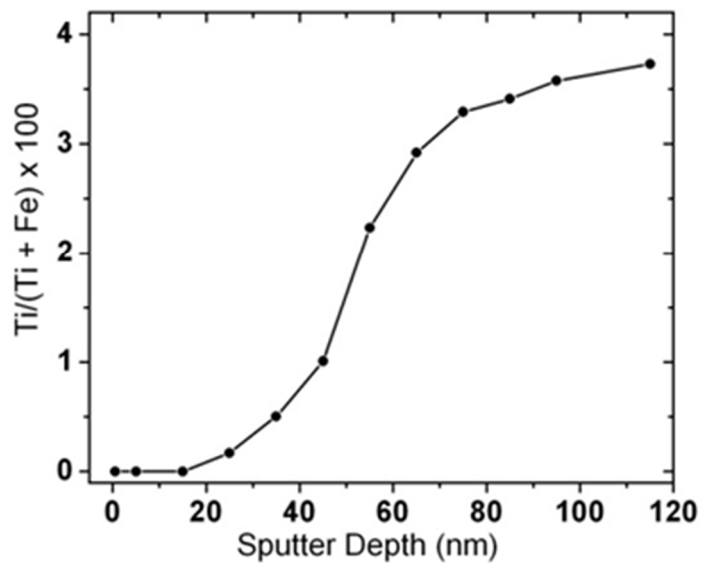


Figure B.5. XPS depth profile of a 4% Ti-doped α -Fe₂O₃ film deposited at 0° incidence and annealed to 450°C for 2 h. Ar⁺ sputter depth was determined using profilometry.

Appendix C: Supplemental Information for Electrochemical Synthesis and Characterization of p-CuBi₂O₄ Thin Film Photocathodes

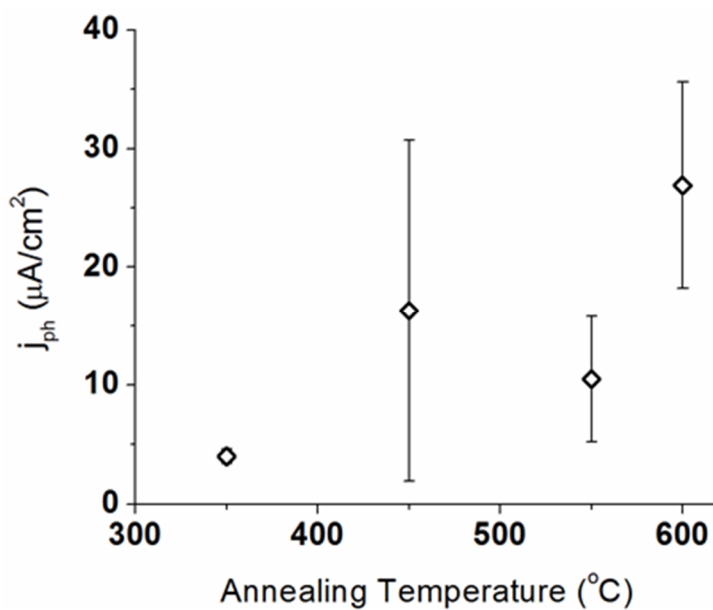


Figure C.1. Steady-state photocurrent density at -0.2 V vs. Ag/AgCl (in N₂ bubbled aqueous Na₂SO₄, pH ~6) for CuBi₂O₄ films deposited from a bath concentration of 12 mM and annealed to various temperatures.

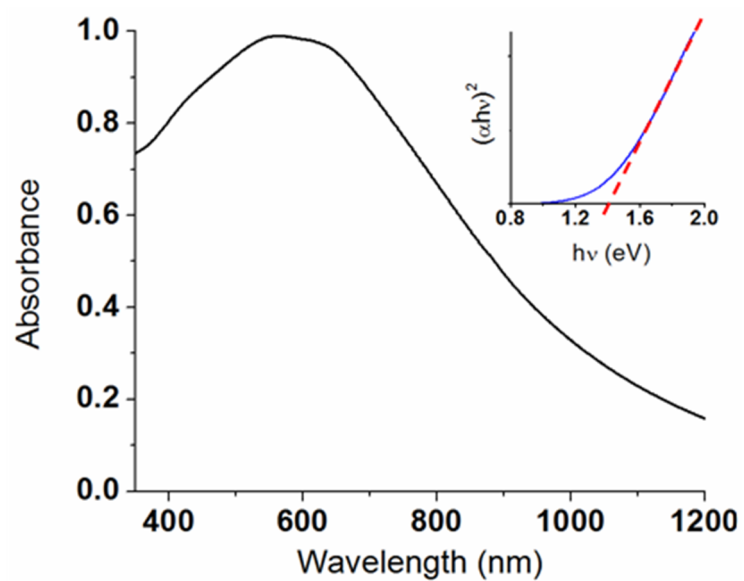


Figure C.2. UV-vis-NIR direct transmittance spectrum of a typical CuBi_2O_4 film deposited from a bath concentration of 6 mM. The inset shows the corresponding Tauc plot indicating an apparent 1.4 eV direct band gap.

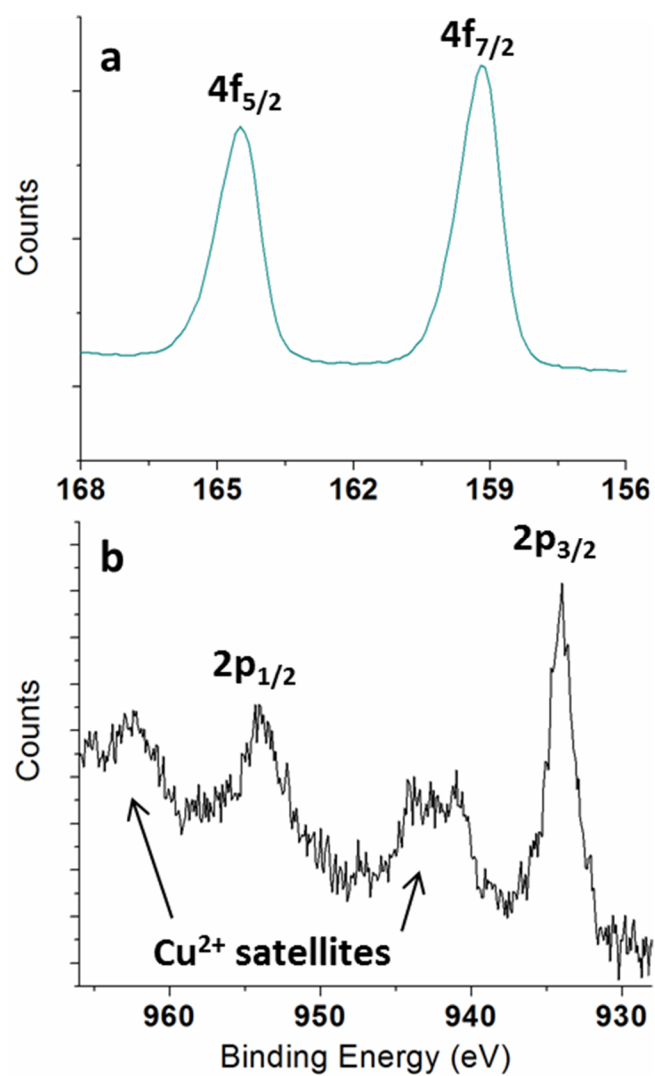


Figure C.3. XPS (a) Bi 4f and (b) Cu 2p spectra for a film prior to PEC testing. Core-level designations for the observed Bi^{3+} and Cu^{2+} peaks are indicated.

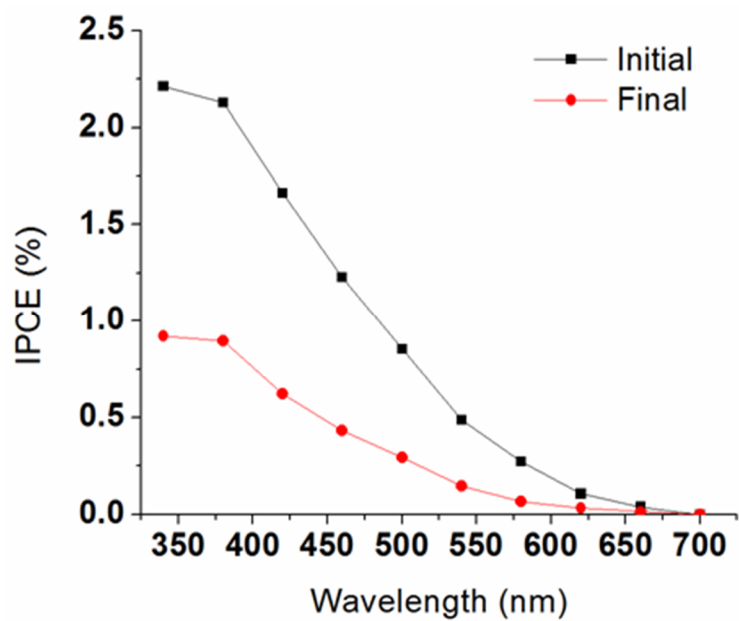


Figure C.4. IPCE values for a typical film before and after 1 h steady photocurrent passage at -0.2 V vs. Ag/AgCl in pH 10.8 aqueous Na₂SO₄.

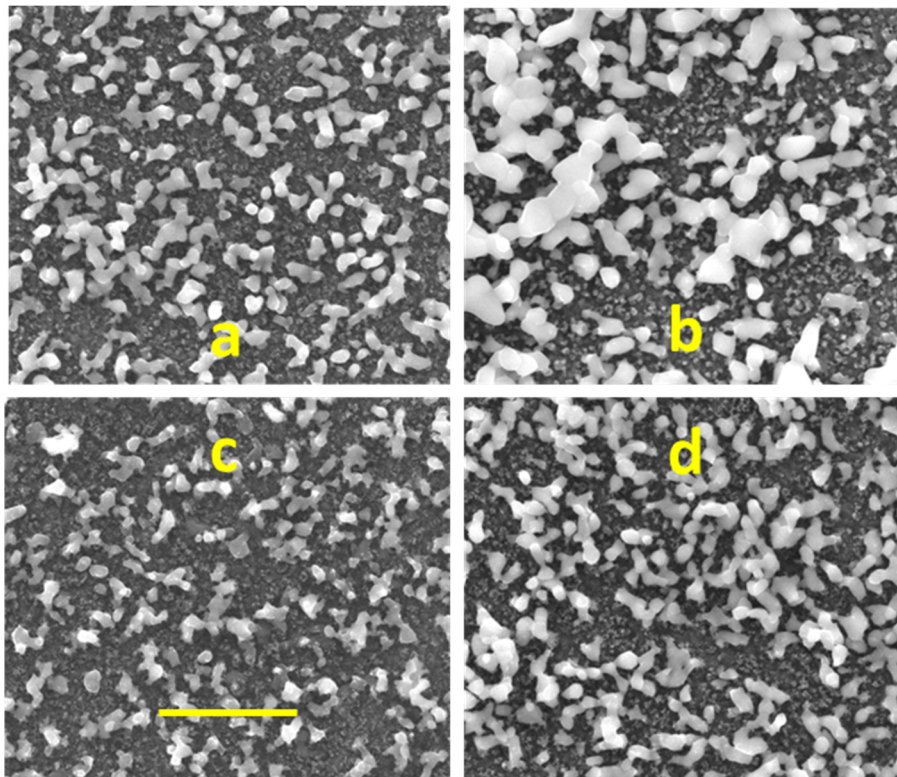


Figure C.5. SEM images of films deposited at -0.7 V for 3.5 min (a) and 7 min (b) as as -0.9 V for 2.5 min (c) and 5 min (d) from a bath containing a 3:1 ratio of Bi:Cu. The scale bar is $2\ \mu\text{m}$ and applies to all images.

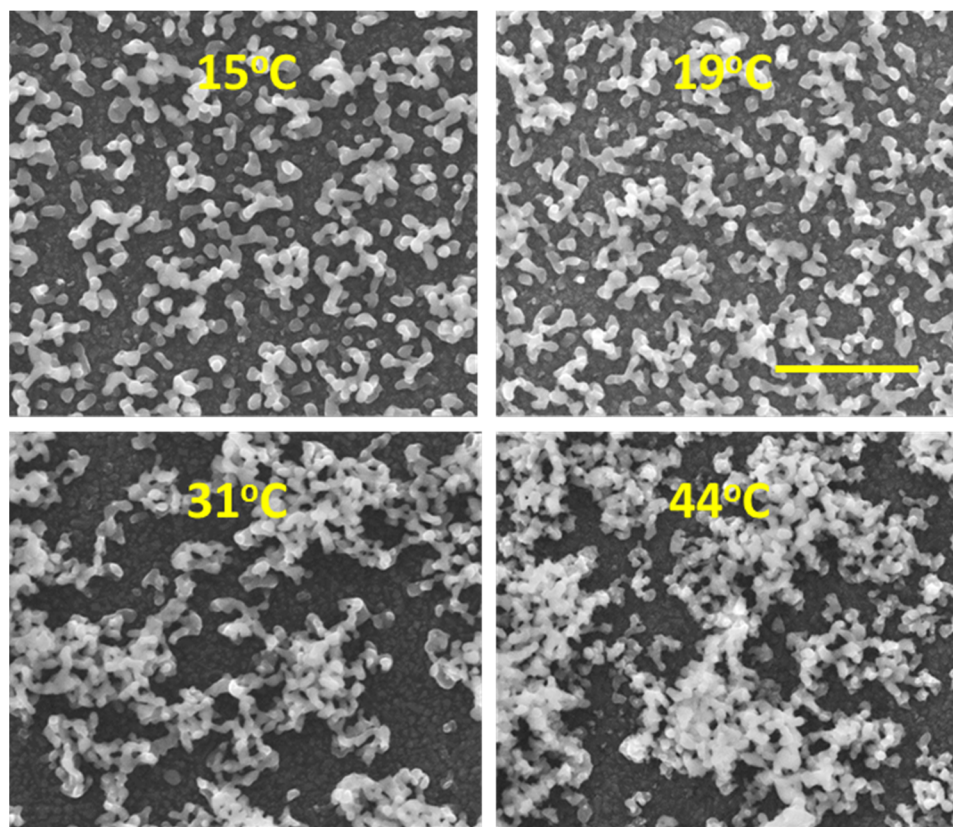


Figure C.6. SEM images of CuBi_2O_4 films deposited from baths at different temperatures at $-0.5\text{ V vs. Ag/AgCl}$ for 5 min. with a cation concentration of 6 mM. The scale bar is $2\ \mu\text{m}$ and applies to all images.

Appendix D: Supplemental Information for Spray Pyrolysis Deposition and Photoelectrochemical Properties of n-type BiOI Nano-platelet Thin Films

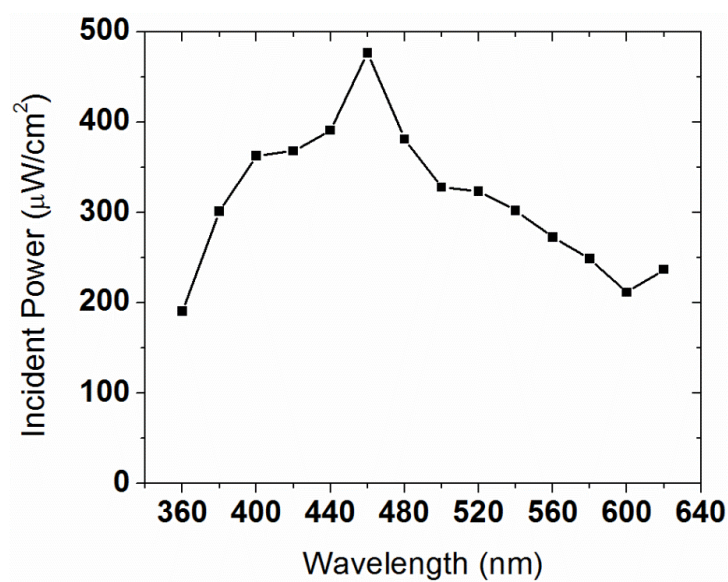


Figure D.1. Monochromatic light intensity at the surface of the film employed for IPCE testing.

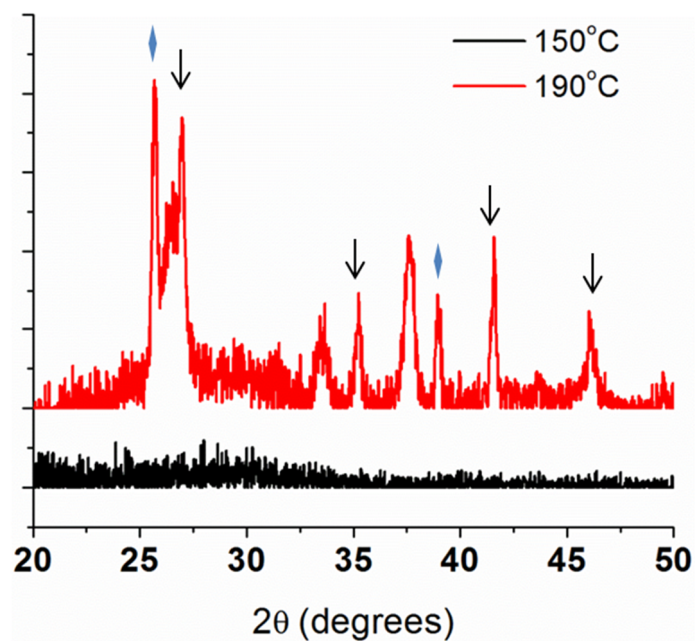


Figure D.2. XRD patterns of films created by spraying the BiOI precursor solution at low temperatures. The arrows indicate the peak positions of BiI_3 , diamonds indicate unidentified peaks, and all other peaks originate from SnO_2 in the substrate.

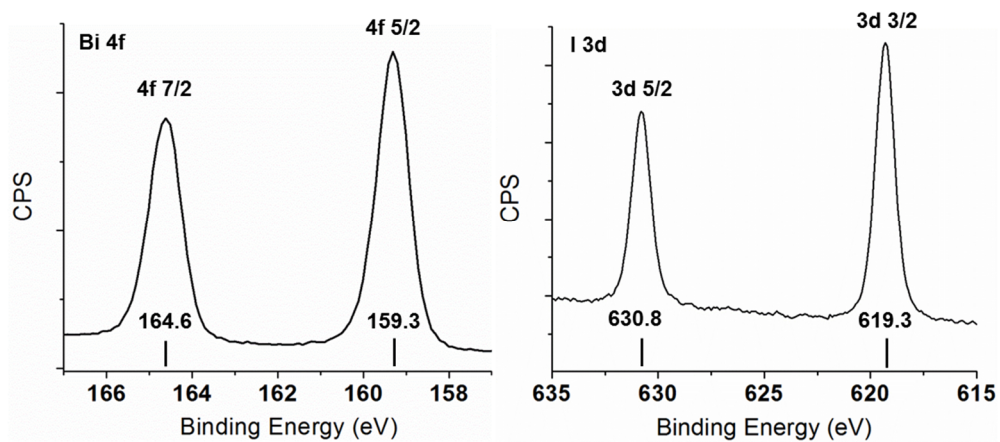


Figure D.3. XPS core-level spectra (Bi 4f and I 3d) for a BiOI film deposited at 260°C, indicating the positions of the Bi³⁺ and I peaks and their orbital designations.

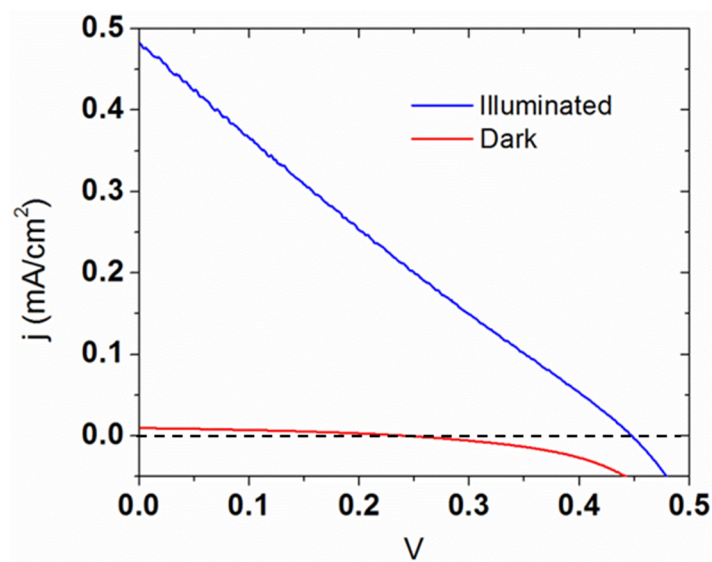


Figure D.4. I-V curves in the dark and under illumination for a BiOI film deposited at 260°C tested using a 2-electrode configuration in 0.5M NaI / 0.05M I₂ in acetonitrile. The working electrode was illuminated from the backside.

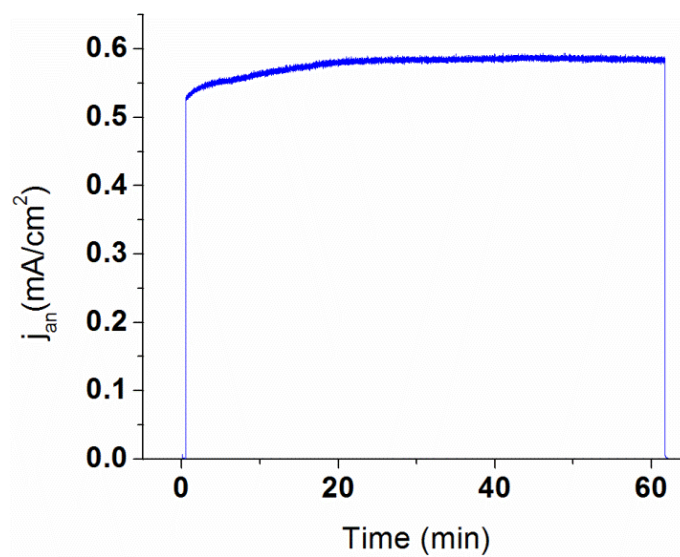


Figure D.5. Steady-state photocurrent test at 0.4 V vs. Ag/AgCl in 0.25M NaI in acetonitrile. The film was deposited at 260°C and illuminated from the backside.

Appendix E: Supplemental Information for BiSI Micro-Rod Thin Films: Efficient Solar Absorber Electrodes?

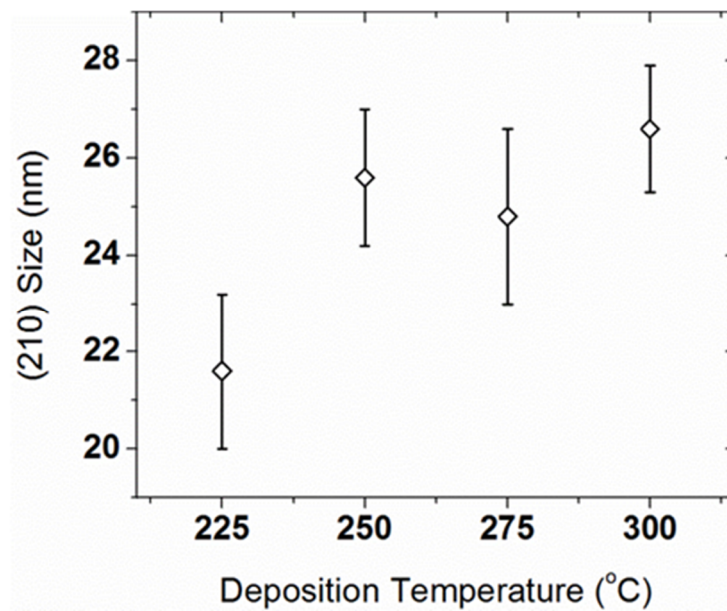


Figure E.1. Mean (210) crystallite sizes calculated from the XRD patterns of films deposited at various temperatures.

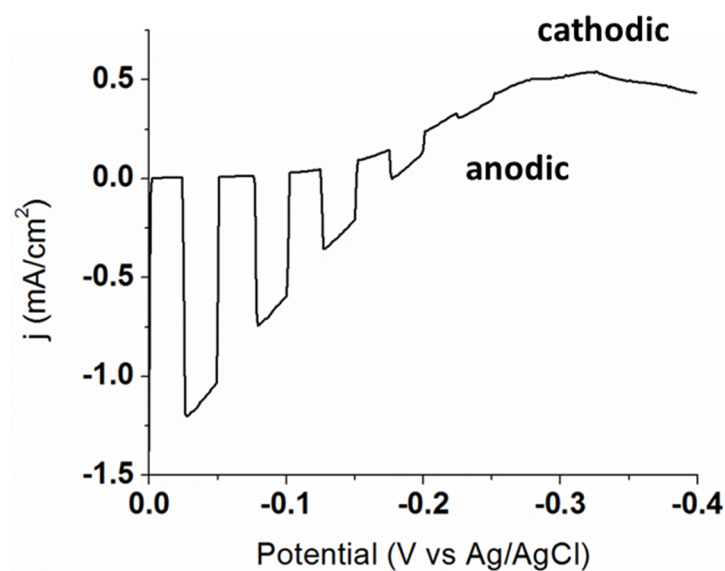


Figure E.2. Linear sweep voltammogram under chopped illumination at cathodic potentials with and without a 420 nm cut-on filter for a film deposited at 275°C. Anodic photocurrents are displayed in the negative direction. The solution was 0.25M NaI in acetonitrile, and the scan rate was 25 mV/s.

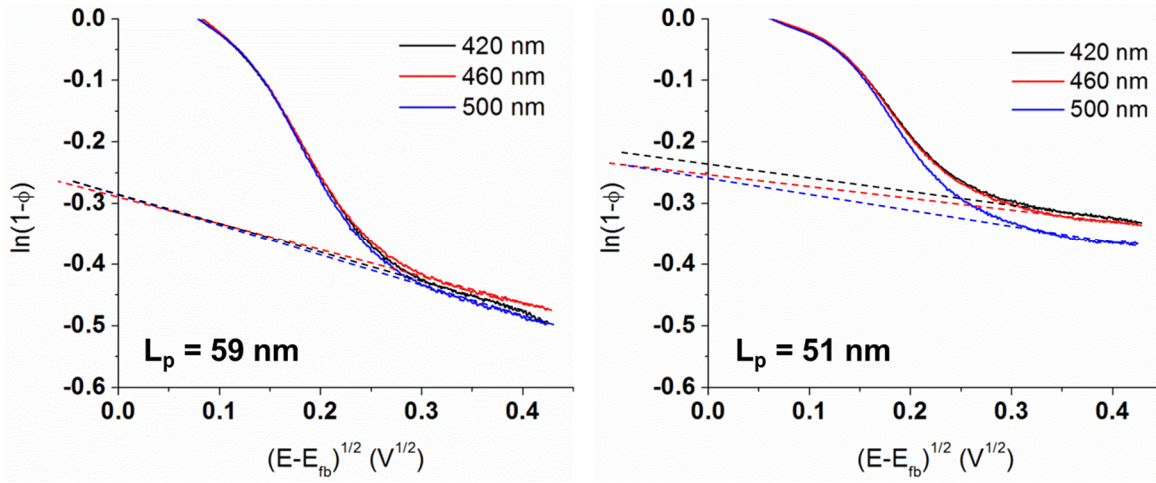


Figure E.3. Plots of $\ln(1-\phi)$ vs. $(E-E_{fb})^{1/2}$ under monochromatic illumination for two different BiSI films deposited at 275C. The average calculated hole diffusion length (L_p) for each set of three measurements is displayed.

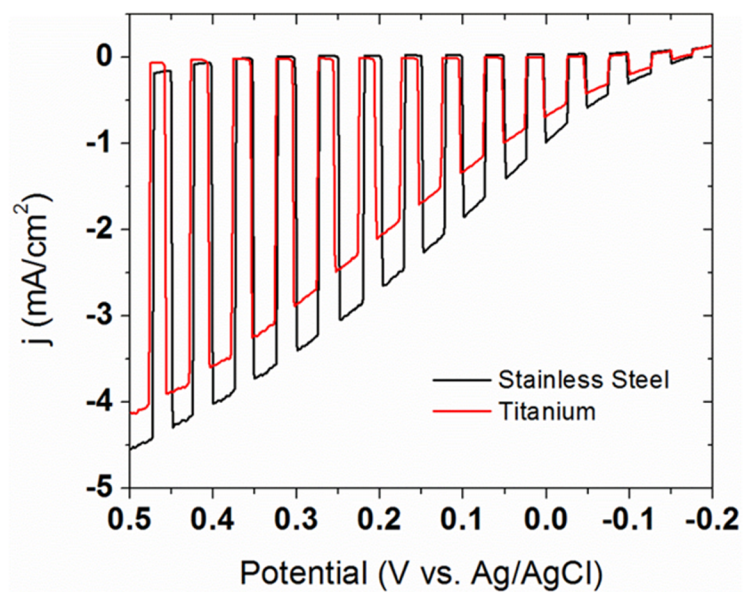


Figure E.4. Linear sweep voltammogram under chopped illumination for films deposited at 275°C on metal foil substrates. The solution was 0.25M NaI in acetonitrile, and the scan rate was 25 mV/s.

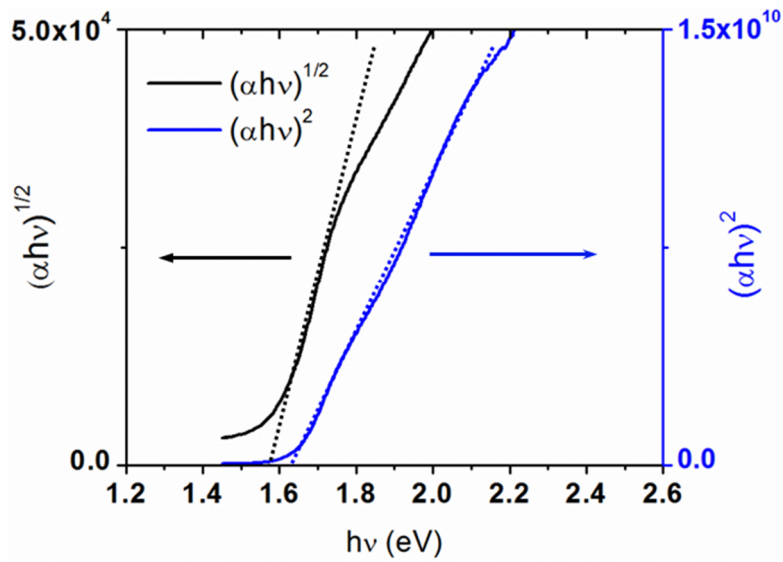


Figure E.5. Tauc plots constructed using total transmittance measurements for a film deposited at 275°C to determine the indirect (black) and direct (blue) bandgaps of BiSI (1.57 and 1.63 eV) from linear fits indicated by the dashed lines.

Bibliography

- Abdulkarem, A.M.; Li, J.; Aref, A.A.; Ren, L.; Elssfah, E.M.; Wang, H.; Ge, Y.; Yu, Y. *Mater. Res. Bull.* 2011, 46, 1443-1450.
- Abelmann, L.; Lodder, C. *Thin Solid Films* 1997, 305, 1-21.
- Anderman, M.; Kennedy, J. H. In *Semiconductor Electrodes*, Finklea, H. O., Ed.; Elsevier: Amsterdam, 1988; Chapter 3.
- Arai, T.; Konishi, Y.; Iwasaki, Y.; Sugihara, H.; Sayama, K. *J. Comb. Chem.* 2007, 9, 574-581.
- Arai, T.; Konishi, Y.; Iwasaki, Y.; Sugihara, H.; Sayama, K. *J. Phys. Chem. C Lett.* 2007, 111, 7574-7577.
- Audzijonis, A.; Zaltauskas, R.; Sereika, R.; Zigas, L.; Reza, A. *J. Phys. Chem. Sol.* 2010, 71, 884-891.
- Banerjee, S.; Mohapatra, S. K.; Misra, M. *Chem. Commun.* 2009, 7137-7139.
- Bard, A. J.; Fox, M. A. *Accounts Chem. Res.* 1995, 28, 141-145.
- Barroso, M.; Cowan, A.J. Pendlebury, S.R.; Grätzel, M.; Klug, D.R.; Durrant, J.R. *J. Am. Chem. Soc.* 2011, 133, 14868-14871.
- Berglund, S.P.; Flaherty, D.W.; Hahn, N.T.; Bard, A.J.; Mullins, C.B. *J. Phys. Chem. C* 2011, 115, 3794-3802.
- Berry, F. J.; Bohorquez, A.; Moore, E. A. *Solid State Commun.* 1999, 109, 207-211.
- Berry, F. J.; Greaves, C.; Helgason, O.; McManus, J.; Palmer, H. M.; Williams, R. T. J. *Solid State Chem.* 2000, 151, 157-162.
- Blankenship, R.E. et al. *Science* 2011, 332, 805-809.
- Boettcher, S. W.; Warren, E. L.; Putnam, M. C.; Santori, E. A.; Turner-Evans, D.; Kelzenberg, M. D.; Walter, M. G.; McKone, J. R.; Brunschwig, B. S.; Atwater, H. A.; Lewis, N. S. *J. Am. Chem. Soc.* 2011, 133, 1216-1219.
- Brillet, J.; Cornuz, M.; Le Formal, F.; Yum, J.H.; Grätzel, M.; Sivula, K. *J. Mater. Res.* 2010, 25, 17-24.

- British Petroleum. *Statistical Review of World Energy*, June 2011.
- Butler, M.A. *J. Appl. Phys.* 1977, *48*, 1914-1920.
- Cesar, I.; Sivula, K.; Kay, A.; Zboril, R.; Graetzel, M. *J. Phys. Chem. C* 2009, *113*, 772-782.
- Chandra, S. Theoretical Models. In *Photoelectrochemical Solar Cells*; OPA: Amsterdam, 1985; pp. 193-236.
- Chang, X.; Huang, J.; Cheng, C.; Sui, Q.; Sha, W.; Ji, G.; Deng, S.; Yu, G. *Catal. Commun.* 2010, *11*, 460-464.
- Chen, Z. et al. *J. Mater. Res.* 2010, *25*, 3-16.
- Cheng, H.; Huang, B.; Dai, Y.; Qin, X.; Zhang, X. *Langmuir* 2010, *26*, 6618-6624.
- Chung, I.; Lee, B.; He, J.; Chang, R.P.H.; Kanatzidis, M.G. *Nature* 2012, *485*, 486-489.
- Cowan, A. J.; Barnett, C. J.; Pendlebury, S. R.; Barroso, M.; Sivula, K.; Graetzel, M.; Durrant, J. R.; Klug, D. R. *J. Am. Chem. Soc.* 2011, *133*, 10134-10140.
- Dai, G.; Yu, Liu, G. *J. Phys. Chem. C* 2011, *115*, 7339-7346.
- Dale, P.J.; Loken, A.; Peter, L.M.; Scragg, J.J. *ECS Trans.* 2009, *19*, 179-187.
- Dohnalek, Z.; Kimmel, G. A.; McCready, D. E.; Young, J. S.; Dohnalkova, A.; Smith, R. S.; Kay, B. D. *J. Phys. Chem. B* 2002, *106*, 3526-3529.
- Duret, A.; Gratzel, M. *J. Phys. Chem. B* 2005, *109*, 17184-17191.
- Eggleston, C. M.; Shankle, A. J. A.; Moyer, A. J.; Cesar, I.; Gratzel, M. A. *Aquat. Sci.* 2009, *71*, 151-159.
- Enache, C.S.; Lloyd, D.; Damen, M.R.; Schoonman, J.; van de Krol, R. *J. Phys. Chem. C* 2009, *113*, 19351-19360.
- Flaherty, D. W.; Dohnalek, Z.; Dohnalkova, A.; Arey, B. W.; McCready, D. E.; Ponnusamy, N.; Mullins, C. B.; Kay, B. D. *J. Phys. Chem. C* 2007, *111*, 4765-4773.
- Flaherty, D. W.; Hahn, N. T.; Ferrer, D.; Engstrom, T. R.; Tanaka, P. L.; Mullins, C. B. *J. Phys. Chem. C* 2009, *113*, 12742-12752.

- Flaherty, D. W.; May, R. A.; Berglund, S. P.; Stevenson, K. J.; Mullins, C. B. *Chem. Mater.* 2010, 22, 319-329.
- Fujishima, A.; Honda, K. *Nature* 1972, 238, 37-38.
- Gerein, N.J.; Haber, J.A. *Chem. Mater.* 2006, 18, 6297-6302.
- Glasscock, J. A.; Barnes, P. R. F.; Plumb, I. C.; Savvides, N. *J. Phys. Chem. C* 2007, 111, 16477-16488.
- Grigas J.; Talik, E.; Adamiec, M.; Lazauskas, V.; Nelkinas, V. *J. Electron Spectrosc.* 2006, 153, 22-29.
- Hahn, N. T.; Ye, H.; Flaherty, D. W.; Bard, A. J.; Mullins, C. B. *ACS Nano* 2010, 4, 1977-1986.
- Hahn, N.T.; Hoang, S.; Self, J.L.; Mullins, C.B. *ACS Nano* 2012, submitted
- Hahn, N.T.; Holmberg, V.C.; Korgel, B.A.; Mullins, C.B. *J. Phys. Chem. C* 2012, 116, 6459-6466.
- Hahn, N.T.; Mullins, C.B. *Chem. Mater.* 2010, 22, 6474-6482.
- Hahn, N.T.; Self, J.L.; Mullins, C.B. *J. Phys. Chem. Lett.* 2012, 3, 1571-1576.
- Hardee, K. L.; Bard, A. J. *J. Electrochem. Soc.* 1976, 123 1024-1026.
- Hashimoto, K.; Irie, H.; Fujishima, A. *Jpn. J. Appl. Phys.* 2005, 44, 8269-8285
- Hawkeye, M.M.; Brett, M. J. *J. Vac. Sci. Technol. A* 2007, 25, 1317-1335.
- Higashi, M.; Domen, K.; Abe, R. *J. Am. Chem. Soc.* 2012, 134, 6968-6971.
- Holzwarth, U.; Gibson, N. *Nat. Nanotechnol.* 2011, 6, 534.
- Horak, J.; Cermak, K. *Czech. J. Phys. B* 1965, 15, 536-538.
- Hu, Y. S.; Kleiman-Shwarsstein, A.; Forman, A. J.; Hazen, D.; Park, J. N.; McFarland, E. W. *Chem. Mater.* 2008, 20, 3803-3805.
- Huang, W. L. *J. Comput. Chem.* 2009, 30, 1882-1891.
- International Energy Agency. *World Energy Outlook 2010*.
- Ishikawa, A.; Takata, T.; Kondo, J.N.; Hara, M.; Domen, K. *J. Phys. Chem. B* 2004, 108, 11049-11053.

- Itoh, K.; Bockris, J. O. J. *Electrochem. Soc.* 1984, 131, 1266-1271.
- Jang, J. S.; Lee, J.; Ye, H.; Fan, F. R. F.; Bard, A. J. *J. Phys. Chem. C* 2009, 113, 6719-6724.
- Jiang, J.; Zhang, X.; Sun, P.; Zhang, L. *J. Phys. Chem. C* 2011, 115, 20555–20564.
- Jiang, S.; Huang, Y.H.; Luo, F.; Du, N.; Yan, C.H. *Inorg. Chem. Commun.* 2003, 6, 781–785.
- Kabra, K.; Chaudhary, R.; Sawhney, R. L. *Ind. Eng. Chem. Res.* 2004, 43, 7683-7696.
- Katagiri, H.; Jimbo, K.; Maw, W.S.; Oishi, K.; Yamazaki, M.; Araki, H.; Takeuchi, A. *Thin Solid Films*, 2009, 517, 2455-2460.
- Katz, J. J.; Gingrich, T. R.; Santori, E. A.; Lewis, N. S. *Energy Environ. Sci.* 2009, 2, 103–112.
- Kay, A.; Cesar, I.; Gratzel, M. *J. Am. Chem. Soc.* 2006, 128, 15714-15721.
- Kelly, N.A.; Gibson, T.L. *Int. J. Hydrogen Energ.* 2006, 31, 1658–1673.
- Kennedy, J.H.; Frese, K.W. *J. Electrochem. Soc.* 1976, 123, 1683-1686.
- Kennedy, J.H.; Frese, K.W. *J. Electrochem. Soc.* 1978, 125, 709-714.
- Khan, S.U.M.; Akikusa, J. *J. Phys. Chem. B* 1999 103, 7184-7189.
- Khaselev, O.; Turner, J.A. *Science* 1998, 280, 425-427.
- Khelladi, M.R.; Mentar, L. ; Azizi, A.; Sahari, A.; Kahoul, A. *Mater. Chem. Phys.* 2009, 115, 385–390.
- Kiema, G. K.; Colgan M. J.; Brett M. J. *Sol. Energ. Mat. Sol. Cells* 2005, 85, 321-331.
- Kim, J. K.; Chhajed, S.; Schubert, M. F.; Schubert, E. F.; Fischer, A. J.; Crawford, M. H.; Cho, J.; Kim, H.; Sone, C. *Adv. Mater.* 2008, 20, 801-804.
- Kim, J.; Dohnalek, Z.; Kay, B. D. *Surf. Sci.* 2005, 586, 137-145.
- Kim, M.J.; Cho, S.K.; Koo, H.C.; Lim, T.; Park, K.J.; Kim, J.J. *J. Electrochem. Soc.* 2010, 157, D564-D569.
- Kleiman-Shwarsctein, A.; Huda, M. N.; Walsh, A.; Yan, Y.; Stucky, G. D.; Hu, Y.; Al-Jassim, M. M.; McFarland, E. W. *Chem. Mater.* 2010, 22, 510–517.

- Kleiman-Shwarscstein, A.; Hu, Y. S.; Forman, A. J.; Stucky, G. D.; McFarland, E. W. J. *Phys. Chem. C* 2008, *112*, 15900-15907.
- Kline, G.; Kam, K.; Ziegler, R.; Parkinson, B. A. *Sol. Energ. Mater.* 1982, *6*, 337-350.
- Kwak, W.C.; Han, S.H.; Kim, T. G.; Sung, Y.M. *Cryst. Growth Des.* 2010, *10*, 5297-5301.
- LaTempa, T. J.; Feng, X. J.; Paulose, M.; Grimes, C. A. *J. Phys. Chem. C* 2009, *113*, 16293-16298.
- Lei, Y.; Wang, G.; Song, S.; Fan, W.; Pang, M.; Tang, J.; Zhang, H. *Dalton Trans.* 2010, *39*, 3273-3278.
- Lewis, N.; Crabtree, G. *Basic Research Needs for Solar Energy Utilization*. 2005, U.S. Department of Energy.
- Li, H.; Zhang, Q.; Pan, A.; Wang, Y.; Zou, B.; Fan, H.J. *Chem. Mater.* 2011, *23*, 1299-1305.
- Li, Y.; Wang, J.; Yao, H.; Dang, L.; Li, Z. *J. Mol. Catal. A-Chem.* 2011, *334*, 116-122.
- Liang, Y.; Enache, C. S.; van de Krol, R. *Int. J. Photoenergy* 2008, Article ID 739864.
- Liang, Y.; Tsubota, T.; Mooij, L.P.A.; van de Krol, R. *J. Phys. Chem. C* 2011, *115*, 17594-17598.
- Lindgren, T.; Vayssieres, L.; Wang, H.; Lindquist, S. E. Photo-Oxidation of Water at Hematite Electrodes. In *Chemical Physics of Nanostructured Semiconductors*; Bahnemann, D.W., Ed.; VSP: Utrecht, 2003; 83-110.
- Liu, H.; Cao, W.; Sua, Y.; Wanga, Y.; Wang, X. *Appl. Catal. B-Environ.* 2012, *111*, 271-279.
- Liu, W.; Chen, S.; Zhang, S.; Zhao, W.; Zhang, H.; Yu, X. *J. Nanopart. Res.* 2010, *12*, 1355-1366.
- Maeda, K.; Domen, K. *J. Phys. Chem. C* 2007, *111*, 7851-7861.
- Marsen, B.; Cole, B.; Miller, E. L. *Sol. Energ. Mat. Sol. Cells* 2008, *92*, 1054-1058.
- May, R. A.; Flaherty, D. W.; Mullins, C. B.; Stevenson, K. J. *J. Phys. Chem. Lett.* 2010, *1*, 1264-1268.
- McShane, C. M.; Choi, K.S.; *J. Am. Chem. Soc.* 2009, *131*, 2561-2569.

- Mesa, F.; Gordillo, G.; Dittrich, T.; Ellmer, K.; Baier, R.; Sadewasser, S. *Appl. Phys. Lett.* 2010, *96*, 082113.
- Miller, E. L.; Paluselli, D.; Marsen, B.; Rocheleau, R. E. *Sol. Energ. Mat. Sol. Cells* 2005, *88*, 131–144.
- Miller, E. L.; Rocheleau, R. E.; Khan, S. *Int. J. Hydrogen Energ.* 2004, *29*, 907–914.
- Mohapatra, S. K.; John, S. E.; Banerjee, S.; Misra, M. *Chem. Mater.* 2009, *21*, 3048–3055.
- Murphy, A. B.; Barnes, P. R. F.; Randeniya, L. K.; Plumb, I. C.; Grey, I. E.; Horne, M. D.; Glasscock, J. A. *Int. J. Hydrogen Energ.* 2006, *31*, 1999–2017.
- Nakamura, R.; Tanaka, T.; Nakato, Y. *J. Phys. Chem. B* 2004, *108*, 10617–10620.
- National Academy of Engineering. *The Hydrogen Economy: Opportunities, Costs, Barriers, and R&D Needs.* 2004, Washington, D.C.: The National Academies Press. ISBN 0-309-53068-7. Retrieved 26 June 2012.
- National Aeronautics and Space Administration. *Global Climate Change – Key Indicators*; <http://climate.nasa.gov/keyIndicators/>, last accessed 6/26/2012.
- Nitsche, R.; Merz, W. J. *J. Phys. Chem. Solids* 1960, *13*, 154–155.
- Nozik, A. J.; *Appl. Phys. Lett.* 1977, *30*, 567–569.
- Nozik, A. J.; Memming, R. *J. Phys. Chem.* 1996, *100*, 13061–13078.
- NREL AM 1.5 Global solar spectrum derived from SMARTS v.2.9.2; <http://rredc.nrel.gov/solar/spectra/aml5/>.
- Paracchino, A.; Laporte, V.; Sivula, K.; Grätzel, M.; Thimsen, E. *Nat. Mater.* 2011, *10*, 456–461.
- Park, J. H.; Kim, S.; Bard, A. J. *Nano Letters* 2006, *6*, 24–28.
- Park, S. A.; Kim, M. Y.; Lim, J. Y.; Park, B. S.; Koh, J. D.; Kim, W. T. *Phys. Stat. Sol. B* 1995, *187*, 253–260.
- Paven-Thivet, C. L.; Ishikawa, A.; Ziani, A.; Gendre, L. L.; Yoshida, M.; Kubota, J.; Tessier, F.; Domen, K. *J. Phys. Chem. C* 2009, *113*, 6156–6162.
- Poxson, D. J.; Mont, F. W.; Schubert, M. F.; Kim, J. K.; Schubert, E. F. *Appl. Phys. Lett.* 2008, *93*, 101914.

- Poznyak, S. K.; Kulak, A. I. *Electrochimica Acta* 1990, 35, 1941-1947.
- Prakasam, H. E.; Varghese, O. K.; Paulose, M.; Mor, G. K.; Grimes, C. A. *Nanotechnology* 2006, 17, 4285-4291.
- Rao, M. V.; Rajeshwar, K.; Pal Verneker, V. R.; DuBow, J. *J. Phys. Chem.* 1980, 84, 1987-1991.
- Riha, S.C.; Fredrick, S.J.; Sambur, J.B.; Liu, Y.; Prieto, A.L.; Parkinson, B.A. *Appl. Mater. Inter.* 2011, 3, 58-66.
- Ritterskamp, P.; Kuklya, A.; Wustkamp, M.A.; Kerpen, K.; Weidenthaler, C.; Demuth, M. *Angew. Chem. Int. Ed.* 2007, 46, 7770-7774.
- Robbie, K.; Brett, M. J.; Lakhtakia, A. *Nature* 1996, 384, 616-616.
- Robbie, K.; Brett, M. J. *J. Vac. Sci. Technol. A* 1997, 15, 1460-1465.
- Robbie, K.; Sit, J. C.; Brett, M. J. *J. Vac. Sci. Technol. B* 1998, 16, 1115-1122.
- Sadale, S.B.; Patil, P.S. *Solid State Ionics* 2004, 167, 273-283.
- Santato, C.; Ulmann, M.; Augustynski, J. *J. Phys. Chem. B* 2001, 105, 936-940.
- Sartoretti, C. J.; Alexander, B. D.; Solaraska, R.; Rutkowska, W. A.; Augustynski, J.; Cerny, R. *J. Phys. Chem. B* 2005, 109, 13685-13692.
- Sasaki, Y. *Japan J. Appl. Phys.* 1965, 4, 614-615.
- Scragg, J.J.; Dale, P.J.; Peter, L.M. *Electrochem. Commun.* 2008, 10, 639-642.
- Seabold, J.A.; Choi, K.S. *J. Am. Chem. Soc.* 2012, 134, 2186-2192.
- Shah, A.; Torres, P.; Tscharnner, R.; Wyrsh, N.; Keppner, H. *Science* 2012, 285, 692-698.
- Shankar, K.; Basham, J. I.; Allam, N. K.; Varghese, O. K.; Mor, G. K.; Feng, X. J.; Paulose, M.; Seabold, J. A.; Choi, K. S.; Grimes, C. A. *J. Phys. Chem. C* 2009, 113, 6327-6359.
- Sheetz, R.M.; Richter, E.; Andriotis, A.N.; Lisenkov, S.; Pendyala, C.; Sunkara, M.K.; Menon, M. *Phys. Rev. B* 2011, 84, 075304.
- Siritanaratkul, B.; Maeda, K.; Hisatomi, T.; Domen, K. *Chem. Sus. Chem.* 2011, 4, 74-78.

- Smith, W.; Zhao, Y. P. *Catal. Commun.* 2009, 10, 1117–1121.
- Solar Radiation Spectrum, prepared by Robert A. Rohde, http://en.wikipedia.org/wiki/File:Solar_Spectrum.png, last accessed 07/25/2012.
- Souza, F. L.; Lopes, K. P.; Longo, E.; Leite, E. R. *Phys. Chem. Chem. Phys.* 2009, 11, 1215-1219.
- Spinolo, G.; Ardizzone, S.; Trasatti, S. *J. Electroanal. Chem.* 1997, 423, 49-57.
- Spray, R.L.; Choi, K. S. *Chem. Mater.* 2009, 21, 3701-3709.
- Stanbery, B.J. *Crit. Rev. Solid State* 2002, 27, 73-117.
- Su, X.; Zhang, G.; Liu, T.; Liu, Y.; Qin, J.; Chen, C. *Russ. J. Inorg. Chem.* 2006, 51, 1864-1868.
- Suzuki, M.; Ito, T.; and Taga, Y. *Appl. Phys. Lett.* 2001, 78, 3968-3970.
- Temple, D.J.; Kehoe, A.B.; Allen, J.P.; Watson, G.W.; Scanlon, D.O. *J. Phys. Chem. C* 2012, 116, 7334-7340.
- Tilley, S.D.; Cornuz, M.; Sivula, K.; Grätzel, M. *Angew. Chem. Int. Ed.* 2010, 49, 1–5.
- Tributsch, H. Electronic Structure, Coordination Photoelectrochemical Pathways and Quantum Energy Conversion by Layered Transition Metal Dichalcogenides. In *Photoelectrochemistry and Photovoltaics of Layered Semiconductors*, Aruchamy, A., Ed.; Kluwer: Dordrecht, 1992; pp. 83-116.
- U.S. Energy Information Administration. "Appendix C. Existing Hydrogen Production Capacity". *The Impact of Increased Use of Hydrogen on Petroleum Consumption and Carbon Dioxide Emissions*, August 2008.
- U.S. Energy Information Administration. *Annual Energy Outlook 2011*.
- U.S. Energy Information Administration. *International Energy Outlook 2011*.
- U.S. Geological Survey. Commodity Statistics and Information. <http://minerals.usgs.gov/minerals/pubs/commodity/> (accessed April, 2012)
- van de Krol, R.; Liang, Y.Q.; Schoonman, J. *J. Mater. Chem.* 2008, 18, 2311-2320.
- Varghese, C. K.; Paulose, M.; Shankar, K.; Mor, G. K.; Grimes, C. A. *J. Nanosci. Nanotechnol.* 2005, 5, 1158–1165.

- Velev, J.; Bandyopadhyay, A.; Butler, W. H.; Sarker, S. *Phys. Rev. B* 2005, *71*, 205208.
- Walter, M. G.; Warren, E. L.; McKone, J. R.; Boettcher, S. W.; Mi, Q.; Santori, E. A.; Lewis, N. S. *Chem. Rev.* 2010, *110*, 6446–6473.
- Wang, K.; Jia, F.; Zhi, Z.; Zhang, L. *Electrochem. Comm.* 2010, *12*, 1764-1767.
- Wang, W.; Huang, F.; Lin, X.; Yang, J. *Catal. Commun.* 2008, *9*, 8–12.
- Wang, W.; Wang, S.Y.; Liu, M. *Mater. Res. Bull.* 2005, *40*, 1781-1786.
- Wang, Y.; Deng, K.; Zhang, L. *J. Phys. Chem. C* 2011, *115*, 14300–14308.
- Wardman, P. *J. Phys. Chem. Ref. Data* 1989, *18*, 1637-1755.
- Weber, F. W.; Dignam, M. J. *J. Electrochem. Soc.* 1984, *131*, 1258-1265.
- White, H. S.; Abruna, H. D.; Bard, A. J. *J. Electrochem. Soc.* 1982, *129*, 265-271.
- Wolcott, A.; Smith, W. A.; Kuykendall, T. R.; Zhao, Y. P.; Zhang, J. Z. *Small* 2009, *5*, 104-111.
- Wolcott, A.; Smith, W. A.; Kuykendall, T. R.; Zhao, Y. P.; Zhang, J. Z. *Adv. Funct. Mater.* 2009, *19*, 1849-1856.
- Woodhouse, M.; Parkinson, B. A. *Chem. Mater.* 2008, *20*, 2495–2502.
- Worldwide Solar Insolation map, generated by meteonorm 6.0, <http://www.solarfeedintariff.net/worldmap.html>, last accessed 6/26/2012.
- Wu, Z.; Huang, F.; Shen, Y.; Xie, A.; Song, X. *J. Nanopar. Res.* 2011, DOI: 10.1007/s11051-011-0417-9
- Xi, J. Q.; Schubert, M. F.; Kim, J. K.; Schubert, E. F.; Chen, M. F.; Lin, S. Y.; Liu, W.; Smart, J. A. *Nat. Photonics* 2007, *1*, 176-179.
- Xia, J.; Yina, S.; Li, H.; Xu, H.; Xu, L.; Zhang, Q. *Colloid Surface A* 2011, *387*, 23–28.
- Ye, L.; Tian, L.; Peng, T.; Zan, L. *J. Mater. Chem.* 2011, *21*, 12479-12484.
- Yokoyama, D.; Minegishi, T.; Jimbo, K.; Hisatomi, T.; Ma, G.; Katayama, M.; Kubota, J.; Katagiri, H.; Domen, K. *Appl. Phys. Express* 2010, *3*, 101202.
- Yokoyama, D.; Minegishi, T.; Maeda, K.; Katayama, M.; Kubota, J.; Yamada, A.; Konagai, M.; Domen, K. *Electrochem. Comm.* 2010, *12*, 851-853.

Zhang, K. L.; Liu, C. M.; Huang, F. Q.; Zheng, C.; Wang, W. D. *Appl. Catal. B-Environ.* 2006, *68*, 125–129.

Zhang, X.; Ai, Z.; Jia, F.; Zhang, L. *J. Phys. Chem. C* 2008, *112*, 747-753.

Zhang, X.; Zhang, L. *J. Phys. Chem. C* 2010, *114*, 18198–18206.

Zhang, Y.C.; Tang, J.Y.; Wang, G.L.; Zhang, M.; Hu, X.Y. *J. Cryst. Growth* 2006, *294*, 278–282.

Zhao, Z.; Liu, F.; Zhao, L.; Yan, S. *Appl. Phys. A* 2011, *103*, 1059-1065.

Vita

Nathan Taylor Hahn was born in Newark, Ohio on October 10, 1984. In 2003 he graduated from Waxahachie High School in Waxahachie, Texas and enrolled in the University of Houston with a major in Chemical Engineering. While there, Nathan engaged in undergraduate research under the direction of Prof. Peter Strasser. After receiving his B.S. in 2007 he enrolled in the Chemical Engineering doctoral program at the University of Texas at Austin where he began his graduate research under the guidance of C. Buddie Mullins.

Email address: nthahn1@gmail.com

This dissertation was typed by the author.